Sharpening Our Observational Tools to Nail Down the Nature of Dark Energy

by

Daniel L. Shafer

A dissertation submitted in partial fulfillment
of the requirements for the degree of
Doctor of Philosophy
(Physics)
in the University of Michigan
2016

Doctoral Committee:

Professor Dragan Huterer, Chair
Professor Fred C. Adams
Professor August E. Evrard
Professor Jeffrey M. McMahon
Professor Christopher J. Miller

---

for Allison

A C K N O W L E D G M E N T S

First and foremost, I would like to thank my advisor, Dragan Huterer, for helpful advice, relentless encouragement, and abundant patience over the last several years. He is an awesome advisor, and I really enjoyed working with him, often feeling more like a colleague than a student. His expertise and experience were crucial to this work.

I would like to thank my parents for sacrificing their time and energy to raise me with every opportunity to be successful, for encouraging me to put my education first, and for constantly offering their help and support.

I would like to thank my wife, Allison, for being my best friend, supporting me throughout this journey, and reminding me that there are things in life other than astrophysics.

Finally, I would like to thank my committee and all of the faculty, staff, and my fellow graduate students in the Physics Department for creating such a supportive atmosphere for learning and research.

P R E F A C E

We live in an exciting time for physical cosmology. The ΛCDM model, one of several viable alternatives two decades ago, has now solidified as the standard cosmological model. It has been well-constrained and well-tested, passing a wide variety of new and more stringent cosmological tests. Even with all of this recent progress, ongoing surveys of unprecedented size, like DES and BOSS, along with future programs like DESI, LSST, JWST, *Euclid*, and WFIRST, will bring improvement by orders of magnitude still, allowing us to robustly test ΛCDM and its possible extensions. These observations, already planned well into the next decade, will bring new challenges in data management and analysis and require new theoretical insights and more powerful simulations. If we can rise to the challenge, we will have many new results, and probably some exciting surprises, to look forward to in the coming years.

This dissertation is based on work carried out at the University of Michigan from 2011–2016, all of which has been previously published in peer-reviewed journals. Chapter 2 is based on Ruiz et al. [1]. My overall contribution to that study was roughly 40% and included Figs. 2.1, 2.3, 2.4, 2.5, 2.6, and 2.11. Chapters 3–5 are based, respectively, on Shafer et al. [2], Shafer et al. [3], and Shafer [4]. Chapter 6 is based on Huterer et al. [5]. My contribution was roughly 30% and included Fig. 6.1.

TABLE OF CONTENTS

LIST OF FIGURES

Figure

LIST OF TABLES

Table

LIST OF APPENDICES

CHAPTER 1

Introduction

1.1 Modern Cosmology from the Cosmological Principle

Cosmology is the subfield of astrophysics concerned with the properties of the universe as a whole, and it has ancient roots. For thousands of years, cultures throughout the world have sought to understand and explain the universe in the context of their world view. Through a mixture of creation stories and other philosophies, often inspired by and tied to careful observations of the night sky, people have tried to answer the big questions: Where did we come from? What else is out there? How does it all work? Descriptions of the universe were as numerous and diverse as the cultures that created them.

On the other hand, only very recently has cosmology become an established science. The existence of distant galaxies was not accepted by the scientific community until the early-to-mid 20th century. Even after our basic cosmological picture was established, measurements were so uncertain that determinations of certain key parameters, such as the Hubble expansion constant and the age of the universe, varied by factors of two. Only in the last decade or two have we been able to turn cosmology into a precise science; however, the result is that we are now able to determine many of these important parameters with percent-level measurement uncertainties.

Cosmology can be modeled in a surprisingly simple framework. On small scales, the heterogeneity of the universe is apparent. In our Solar System, dense planets and asteroids move along stable orbits, leaving a near vacuum everywhere else. On galactic scales, we find dense galaxies and galaxy clusters in some regions and voids elsewhere. On even larger scales, however, we can map the enormous filaments of large-scale structure that carry us to the edge of the observable universe. On these scales ($\gtrsim$100 Mpc), we can often rely on the (testable) assumptions of homogeneity and isotropy. Homogeneity is the statement that the universe is the same everywhere, while isotropy is the statement that there is no preferred direction. They are consequences of the *cosmological principle*, which asserts that on the

largest scales, all properties of the universe are the same for all observers.

From these conditions, we can write down a compatible spacetime metric in the framework of general relativity (see e.g. [6]). We choose one which allows the spatial coordinates to scale (equally) with time and which allows for space to have uniform intrinsic curvature, which can be realized in one of three ways, as dictated by the value of the constant k. The possibilities for k are positive curvature (spherical geometry, closed universe), zero curvature (flat geometry, critical universe), or negative curvature (hyperbolic geometry, open universe). One can show that the appropriate metric is

$$ds^2 = -dt^2 + a(t)^2 \left[\frac{1}{1-kr^2}\, dr^2 + r^2 \left(d\theta^2 + \sin^2\theta\, d\phi^2 \right) \right], \tag{1.1}$$

where we have set the speed of light $c = 1$. This is the famous Friedmann-Lemaître–Robertson-Walker (FLRW) metric. From this interval, one can immediately deduce the corresponding metric tensor $g_{\mu\nu}$ and compute the Christoffel symbols, the Riemann tensor, the Ricci tensor $R_{\mu\nu}$, and the Ricci scalar R. The resulting Einstein tensor is given by

$$\begin{aligned} G_{\mu\nu} &= R_{\mu\nu} - \frac{1}{2} g_{\mu\nu} R \\ &= \text{diag}\left[\frac{3\,(k+\dot{a}^2)}{a^2}\,,\, -\frac{Z}{1-kr^2}\,,\, -r^2\, Z\,,\, -r^2 \sin^2\theta\, Z \right], \end{aligned} \tag{1.2}$$

where $Z \equiv 2a\ddot{a} + \dot{a}^2 + k$. For consistency, we should apply the assumptions of homogeneity and isotropy to the stress-energy tensor. With the assumption of a perfect fluid — one with no shear stresses, heat conduction, or viscosity, the stress-energy tensor is simply

$$T_{\mu\nu} = (\rho + p)\, U_\mu U_\nu + p\, g_{\mu\nu} = \text{diag}\left[\rho\,,\, \frac{p\, a^2}{1-kr^2}\,,\, p\, a^2 r^2\,,\, p\, a^2 r^2 \sin^2\theta \right], \tag{1.3}$$

where ρ is the fluid's energy density, p is its pressure, and $U_\mu = (1,0,0,0)$ is the four-velocity. We can now solve the Einstein field equations $G_{\mu\nu} = 8\pi G\, T_{\mu\nu}$ using the above. The equation for the 00 component immediately produces the following result:

$$\left(\frac{\dot{a}}{a} \right)^2 = \frac{8\pi G}{3} \rho - \frac{k}{a^2}\,. \tag{1.4}$$

The tensor trace gives a second independent result:

$$\begin{aligned} g^{\nu\mu}\, G_{\mu\nu} &= 8\pi G\, g^{\nu\mu}\, T_{\mu\nu} \\ -R &= 8\pi G\, T^{\nu}{}_{\nu} \\ -\frac{6}{a^2}\left(a\ddot{a} + \dot{a}^2 + k\right) &= 8\pi G\left(-\rho + 3p\right) \qquad (1.5) \\ \frac{\ddot{a}}{a} &= -\frac{4\pi G}{3}\left(\rho + 3p\right)\ . \qquad (1.6) \end{aligned}$$

Eq. (1.6) follows from using Eq. (1.4) to rewrite Eq. (1.5). There are, in general, 10 independent field equations to solve, but our assumptions (symmetries) leave only four nontrivial equations, two of which are redundant. Although there are no more independent results, it is possible and often useful to combine the above two equations and write down a third. If we multiply Eq. (1.4) by a^2, take its time derivative, and substitute for $\ddot{a}/a$ in Eq. (1.6), we obtain:

$$\dot{\rho} = -3\,\frac{\dot{a}}{a}\left(\rho + p\right)\ . \qquad (1.7)$$

Often these equations are collectively referred to as the Friedmann equations, but Eq. (1.4) is often called *the* Friedmann equation, with Eq. (1.6) called the acceleration equation and Eq. (1.7) called the fluid equation, an expression of conservation of energy. The quantity a is the scale factor, and it is the (time-dependent) factor that translates between comoving distance and physical distance, where comoving distance (also called coordinate distance) is unchanged by any expansion or contraction of the universe. Comoving distance coincides with physical distance at the value $a = 1$.

1.2 The Cosmological Constant and Simple Cosmologies

Einstein, motivated by his expectation of a steady-state universe, added a term $\Lambda\, g_{\mu\nu}$ to the Einstein tensor, where Λ is called the *cosmological constant*. Today, it is widely accepted that the universe is expanding and *not* in a steady state; however, the possibility of a cosmological constant is intriguing. In fact, if one simply writes the constant term on the other side of the equation, $G_{\mu\nu} = 8\pi G\, T_{\mu\nu} - \Lambda\, g_{\mu\nu}$, it has the appearance of a *vacuum energy density*, since it contributes to the stress-energy tensor $T_{\mu\nu}$. With the cosmological constant included, Eq. (1.4) becomes

$$\left(\frac{\dot{a}}{a}\right)^2 = \frac{8\pi G}{3}\rho - \frac{k}{a^2} + \frac{\Lambda}{3}\,, \qquad (1.8)$$

while Eq. (1.7) is unchanged.

To understand the effect of a so-called vacuum energy, we will first study the Friedmann equations in more detail. Let us rewrite Eq. (1.8) in a more useful form. The important thing to remember is that ρ represents the *total* energy density of the homogeneous universe. But the universe does not contain only one type of fluid. It contains both matter (ordinary baryonic matter and non-baryonic cold dark matter) and radiation (hot, relativistic matter particles like light neutrinos would also be included here). It is also convenient to describe both curvature and the cosmological constant in terms of an energy density, though it is important to emphasize that curvature does *not* actually contribute to a physical energy density, unlike Λ, which might. So let us define ρ_i to be the energy density of species i only, and then let us also define

$$\rho_k = \frac{3}{8\pi G}\frac{k}{a^2} \ , \quad \rho_\Lambda = \frac{\Lambda}{8\pi G} \ , \tag{1.9}$$

so that the Friedmann equation becomes

$$H^2 = \frac{8\pi G}{3}\left(\rho - \rho_k\right) \ , \quad \rho = \rho_m + \rho_r + \rho_\Lambda \ , \quad H \equiv \frac{\dot{a}}{a} \ . \tag{1.10}$$

Here, H is the Hubble parameter, which describes the rate of expansion of the universe; like a, it is a function of time.

One further simplification is helpful. Notice that if we set $\rho = 3H^2/(8\pi G)$ in Eq. (1.10), it would imply that $k = 0$ and the universe is flat. Since k is a constant, if this is the case at one time, then k is *always* zero and it is thus impossible for an expanding universe ($\dot{a} > 0$) to contract, though the rate of expansion will approach zero as $t \to \infty$. This motivates the definition of the critical density $\rho_{\text{crit}} = 3H^2/(8\pi G)$ and the fractional density $\Omega_i = \rho_i/\rho_{\text{crit}}$. The Friedmann equation simply becomes $\Omega - \Omega_k = 1$.

To proceed further, we observe that the two independent Friedmann equations involve three variables (a, ρ, and p). In order to get some real solutions, we must close the system by relating two of these quantities. The most obvious way to do that is by assuming an equation of state, which is a relationship between p and ρ. For the perfect fluids that we want to describe, the equation of state has the form $p_i = w_i\rho_i$, where w_i is a constant. For matter, which is assumed to be cold (non-relativistic), the pressure is negligible compared to the energy density, so we set $w_m = 0$ so that $p_m = 0$. For radiation, we know from statistical mechanics that $p_r = \rho_r/3$ so that $w_r = 1/3$. Although not the case for the other fluids, we expect the vacuum stress-energy tensor to be Lorentz invariant (all observers should see the same vacuum). Since $T_{\mu\nu} \propto g_{\mu\nu}$ when $p_\Lambda = -\rho_\Lambda$, we have $w_\Lambda = -1$. For curvature,

we can deduce the effective w_k from the fluid equation. Substituting the definition of ρ_k in Eq. (1.9) into Eq. (1.7) and specifying $p_k = w_k \rho_k$, we find that $w_k = -1/3$.

We expect the fluid equation to be valid for any species i. Since we now know the pressure as a function of energy density for each species, we can solve Eq. (1.7) to find the energy density ρ_i as a function of the scale factor a:

$$\rho_i = \rho_{i,0}\, a^{-3(1+w_i)}. \tag{1.11}$$

It is customary to denote present values with a subscript $_0$ and to fix $a_0 = 1$ (since a is just a scale factor, its overall normalization has no physical significance, and this is the most convenient choice).

This result is easy to understand. For matter, $w_m = 0$, so $\rho_m \propto a^{-3}$. This is what we expect: given some fixed amount of matter, its average mass density is inversely proportional to its volume. The mass of non-relativistic matter is proportional to its energy, and the actual volume of the universe is proportional to a^3, so this result is consistent with expectations. For radiation ($w_r = 1/3$), we find that $\rho_r \propto a^{-4}$. Here, we still expect the same dilution factor that applies to matter, but there is an extra factor of $1/a$. This is due to the fact that, as the universe expands, so do the wavelengths of photons, and the energy of a photon $E = hc/\lambda$ is inversely proportional to its wavelength. For the cosmological constant ($w_\Lambda = -1$), we find ρ_Λ to be constant. This may seem surprising, but if Λ is interpreted as vacuum energy, this makes sense: the volume of the universe may change, but the amount of vacuum energy is proportional to the volume of the vacuum, so the density is constant. The curvature result ($\rho_k \propto a^{-2}$) is less intuitive but is a consequence of the way we defined curvature density.

Finally, we can rewrite the Friedmann equation one more time by inserting the expressions for $\rho_i(a)$ and making use of the parameters Ω_i that we defined earlier:

$$H^2(a) = H_0^2 \left[\Omega_m a^{-3} + \Omega_r a^{-4} + \Omega_\Lambda - \Omega_k a^{-2}\right], \tag{1.12}$$

where these Ω_i refer to present values even though the subscript $_0$ is almost always omitted. Defining the cosmological redshift of photons as

$$1 + z \equiv \frac{\lambda_{\text{obs}}}{\lambda_{\text{emit}}} = \frac{1}{a}\,, \tag{1.13}$$

we can express Eq. (1.12) equivalently in terms of the redshift:

$$H^2(z) = H_0^2 \left[\Omega_m\,(1+z)^3 + \Omega_r\,(1+z)^4 + \Omega_\Lambda - \Omega_k\,(1+z)^2\right]. \tag{1.14}$$

Equations (1.12) and (1.14) are probably the most illuminating and most useful forms of the Friedmann equation.

Solving for $a(t)$, for instance, is now straightforward, though for a realistic universe the Friedmann equation must be integrated numerically for a given choice of the Ω_i and H_0 parameters. To gain insight, we can solve Eq. (1.12) assuming that the energy density of the universe is dominated by one of the fluids so that we can ignore the others. This may seem like a terrible oversimplification, since we know that the universe has multiple components and has had multiple components in the past; however, since each fluid tends to dominate during a different epoch, these simpler solutions could in principle be stitched together to obtain a more complete picture. So let us now find the solution for $a(t)$ when a fluid with equation of state parameter w is dominant. By integrating the simplified version of Eq. (1.12),

$$H^2 = H_0^2 \, a^{-3(1+w)}, \tag{1.15}$$

we find

$$a(t) = \left(\frac{t}{t_0}\right)^{\frac{2}{3(1+w)}}, \quad w \neq -1. \tag{1.16}$$

Here we have assumed that the universe had zero size ($a = 0$) at a time $t = 0$ (corresponding to the Big Bang) and used the present as a reference point ($a(t_0) = 1$). For the special case $w = -1$, one can go back to Eq. (1.15). The result is

$$a(t) = e^{H_0(t-t_0)} = e^{\sqrt{\Lambda/3}\,(t-t_0)}, \quad w = -1. \tag{1.17}$$

Thus we have exponential expansion as a function of time when the cosmological constant dominates. It is evident from Eq. (1.17) that one cannot have a nontrivial solution with $a = 0$ at $t = 0$, but we were able to set $a(t_0) = 1$ as in the other cases. A summary of the results for these simple one-fluid universes is given in Table 1.1.

component	**symbol (i)**	w_i	$\rho_i(a) \propto$	$a(t) \propto$
cold matter	m	0	$1/a^3$	$t^{2/3}$
radiation	r	$1/3$	$1/a^4$	$t^{1/2}$
curvature	k	$-1/3$	$1/a^2$	t
cosmological constant	Λ	-1	1	$e^{\sqrt{\Lambda/3}\,t}$

Table 1.1: Summary of results for simple one-component universes.

1.3 The Standard Cosmological Model

The currently favored cosmological model features a universe that consists mostly of cold dark matter and dark energy in the form of a cosmological constant. A Big Bang occurred 13.8 billion years ago, with space itself expanding from a very small, hot, and dense initial state. Roughly 10^{-36} seconds after the Big Bang, inflation — a period of very rapid expansion — occurred, driving any intrinsic curvature to very near zero and seeding the universe with small, Gaussian density perturbations. A few seconds later, protons and neutrons fused to form hydrogen and helium along with trace amounts of heavier elements in a process called Big Bang nucleosynthesis (BBN), which lasted several minutes. After about 380,000 years, at a redshift $z \simeq 1100$, the universe cooled enough for electrons and protons to combine and form neutral hydrogen, allowing photons to free stream. These photons are observed today at a temperature of 2.73 K as the cosmic microwave background (CMB). The universe then entered a period, the Dark Ages, which lasted until the epoch of reionization when the first stars formed and partially reionized the universe. The formation of galaxies and galaxy clusters followed, creating a large-scale structure imprinted with the primordial density perturbations and acoustic waves. At $z \sim 1$, roughly half the present age, the expansion of the universe began to accelerate due to the cosmological constant Λ, which now dominates the energy budget.

This model is called ΛCDM, since the primary ingredients are a cosmological constant and cold dark matter. With only six free parameters, ΛCDM accurately describes an enormous breadth of cosmological observations and has passed stringent tests in recent years. The six parameters are: the physical densities of cold dark matter and baryons $\Omega_c h^2$ and $\Omega_b h^2$, the Hubble constant $H_0 = 100\,h$ km/s/Mpc, the amplitude and index of a power law primordial power spectrum $P(k) = A_s\,(k/k_{\rm piv})^{n_s}$, and the optical depth at reionization τ. With the minor exception of τ, which is rather poorly constrained at present, *Planck* CMB observations [7] alone measure all of these parameters with roughly 1% precision.

Testing the ΛCDM model and characterizing the nature of dark energy are among the central challenges for modern cosmology. Given the robustness of ΛCDM, it is not surprising that most alternative models are extensions in the sense that ΛCDM is embedded as a special case. Such extensions include a non-minimal neutrino sector, where the neutrino mass sum or the effective number of species is allowed to vary; a non-minimal dark energy sector, where the equation of state is allowed to be different from -1 and vary with cosmic time; a nonzero value for intrinsic curvature; and a non-minimal inflationary epoch that manifests running of the spectral index or a nonzero tensor-to-scalar ratio. Many of these one- or two-parameter extensions are already well-constrained by combined data (e.g. [7]).

1.4 Distance Probes of Dark Energy

Here we give a brief overview of the three classic distance probes of dark energy and cosmic expansion: Type Ia supernovae (SNe Ia), CMB fluctuations, and baryon acoustic oscillations (BAO).

1.4.1 SNe Ia

SNe Ia alone were used to discover dark energy [8, 9]. They function as bright standard candles — objects with roughly constant or otherwise deterministic luminosity whose apparent brightnesses can be used to infer distance. SNe Ia are characterized spectroscopically by the lack of a hydrogen line, distinguishing them from Type II SNe, and the presence of a singly ionized silicon line, distinguishing them from Type Ib/c SNe. While the other types are associated with the core collapse of a dying massive star, it is thought that a SN Ia occurs when mass is accreted onto the surface of a white dwarf from a companion star. When the white dwarf accumulates enough mass to exceed the Chandrasekhar limit, the whole star detonates, releasing an enormous amount of energy in the process. Given this specific mass limit ($\sim 1.4\, M_\odot$) for white dwarves, it is not surprising that all SNe Ia release approximately the same amount of energy.

It is important to note that, whether or not our understanding of this mechanism is correct, it is an empirical fact that there exist stellar explosions, distinguishable from other stellar explosions, that tend to have similar peak luminosities. Since these explosions are very bright, they can be observed at high redshifts, making them useful for measuring cosmological distances.

The apparent magnitude of a SN Ia is given by

$$m(z) = 5\, \log_{10}\left[\frac{H_0}{c}\, d_L(z)\right] + \mathcal{M}\,, \tag{1.18}$$

where d_L is the luminosity distance and $\mathcal{M}$ is an offset that depends on the Hubble constant H_0 and the absolute magnitude of a SN Ia, which is *a priori* unknown. The luminosity

distance is given by $d_L(z) = (1+z)\, r(z)$, where

$$r(z) \equiv \begin{cases} R_0 \, \sin\left[\chi(z)/R_0\right] & \Omega_k > 0 \\ \chi(z) & \Omega_k = 0 \\ R_0 \, \sinh\left[\chi(z)/R_0\right] & \Omega_k < 0 \end{cases} \tag{1.19}$$

$$\chi(z) \equiv \int_0^z \frac{c}{H(z')}\, dz' \,, \quad R_0 \equiv \frac{c}{H_0} \frac{1}{\sqrt{|\Omega_k|}} \,. \tag{1.20}$$

For a flat universe, the Hubble parameter has the form

$$H(z) = H_0 \sqrt{\Omega_m \, (1+z)^3 + \Omega_X \, (1+z)^{3(1+w)}} \,, \tag{1.21}$$

where we have left out the radiation contribution, which is negligible for the relatively low redshifts ($z \lesssim 2$) where we find SNe. Also, we have replaced the Λ term with a more general dark energy term, assuming a constant equation of state that reduces to Λ if $w = -1$.

SNe are not perfect standard candles; their absolute magnitudes vary with a scatter of $\sim$0.3 mag, corresponding to a distance error of $\sim$14%. But useful empirical correlations exist between the peak apparent magnitude and other light-curve properties, notably the light curve's stretch (i.e. broadness, decline time) and color measure (e.g. magnitude difference between two bands). As a rule of thumb, broader is brighter, and bluer is brighter. These relations further standardize SNe Ia, reducing the intrinsic scatter to $\sim$0.15 mag or less for a distance error of less than 7%.

Since these standardization relations are empirical, substantial current work is focused on how best to model them, determining whether other useful correlations exist, and attempting to quantify any possible evolutionary effects.

1.4.2 CMB

The CMB contains a wealth of cosmological information; it can separately inform us about the densities of dark matter and baryons, the physics of inflation, and the geometry of the universe [7]. Until relatively recently, most of this information came from measurements of the power spectrum of temperature fluctuations, but today these are joined by measurements of the E-mode and B-mode polarization spectra as well as the CMB lensing potential.

On the other hand, CMB observations are very limited in their ability to constrain general models of the dark energy equation of state. Since dark energy was negligible at high redshifts, the CMB is only sensitive to dark energy in how it affects the CMB photons on

their way to us. While this includes some information from the effect of dark energy on growth of structure, via the integrated Sachs-Wolfe (ISW) effect and gravitational lensing, most of the information is encapsulated by a single measure of distance to the surface of recombination. Since the redshift z_* of recombination is not known *a priori*, it is most appropriate to summarize CMB distance information with a set of observables. A common choice is to measure z_* along with

$$l_a \equiv \pi \, (1 + z_*) \, \frac{d_A(z_*)}{r_s(z_*)} \, , \tag{1.22}$$

$$R \equiv \frac{\sqrt{\Omega_m H_0^2}}{c} \, (1 + z_*) \, d_A(z_*) \, , \tag{1.23}$$

where l_a is the acoustic angular scale, R is the so-called shift parameter, and r_s is the sound horizon — the distance that a sound wave travels in a time t since the Big Bang, given by

$$r_s(t) = \int_0^t \frac{c_s}{a} \, dt' \, , \quad c_s = \frac{c}{\sqrt{3 \, (1 + R)}} \, , \tag{1.24}$$

where the sound speed c_s depends on the ratio of baryon energy density to photon energy density, with $R \equiv 3\rho_b/(4\rho_\gamma)$.

Although these observables basically provide one distance measurement, it is a very precise distance to a very high redshift, so the approximate result is that it effectively fixes one parameter describing the geometry of the late universe, for instance, a constraint on Ω_m or a narrow constraint band in the Ω_m – w plane.

It is important to be aware of any possible model dependence of these observables. While they are typically independent of any dark energy model, they will be sensitive to the overall cosmological model. For instance, the measured value of z_* might shift if non-standard neutrino physics is assumed.

1.4.3 BAO

BAO are the regular, periodic fluctuations of visible matter density in large-scale structure (LSS) resulting from sound waves propagating in the early universe. The BAO signal corresponds to a peak in the correlation function at a comoving scale of $\sim$150 Mpc. This scale is an excellent standard ruler, and measuring the location of the peak at various redshifts will probe expansion and dark energy. The first detection of the feature in the SDSS LRG sample [10] has since been replaced by several more precise measurements, including one at $z = 0.106$ (6dF, [11]), $z = 0.32$ (BOSS LOWZ, [12]), and $z = 0.57$ (BOSS CMASS, [13]), with the latter achieving a $\sim$1% distance measurement. BAO can also be detected in

other LSS tracers, such as Lyman-α forests, where the feature has been detected at $z = 2.34$ using BOSS quasars (e.g. [14]).

The typical observable derived from the BAO measurement is $D_V(z_{\rm eff})/r_d$, where $z_{\rm eff}$ is the median redshift of the LSS survey, $r_d \equiv r_s(z_d)$ is the size of the sound horizon at the epoch of baryon drag, and D_V is a spherical-volume-averaged distance defined by

$$D_V(z) \equiv \left[(1+z)^2\, d_A^2(z) \frac{cz}{H(z)}\right]^{1/3}. \tag{1.25}$$

Recently, it has been possible to achieve high signal-to-noise detections using the transverse and radial correlation functions separately, resulting in separate measurements of $(1+z_{\rm eff})\, d_A(z_{\rm eff})/r_d$ and $cz_{\rm eff}/H(z_{\rm eff})/r_d$. In addition to providing more cosmological constraining power, these anisotropic measurements can be used to look for exotic departures from the standard model.

One important caveat when using the BAO observables is that the measurements are often correlated. This is the case for the anisotropic measurements as well as for measurements at different redshifts and/or from different surveys if there is overlap in survey volume. Neglecting any significant correlation will lead to incorrect constraints and underestimates of errors.

Also, note that comparing data to theory here requires a way to estimate the size of the sound horizon, which ultimately requires some information from the CMB, such as a prior on the sound horizon itself, priors on $\Omega_m h^2$ and $\Omega_b h^2$, or some combination thereof. One way around this is to use multiple BAO measurements as *relative* distance indicators, as one typically does with SNe Ia, and just marginalize over the sound horizon.

BAO measurements are generally thought to be robust and free of systematic effects at least down to the 1% level, making them effective probes of dark energy, especially at higher redshifts, where they will likely out-perform SN Ia distances.

Fig. 1.1 illustrates how the three probes (SN Ia, CMB, BAO) complement one another to constrain dark energy by breaking degeneracies in parameter space. Combining these and other probes not only allows us to more precisely determine cosmological parameters, it also provides a way to check for consistency and determine whether there are any unaccounted-for systematic effects.

1.5 Outline

This goal of this dissertation is to investigate systematic effects and perform new cosmological tests with observational probes of dark energy in anticipation of the precision dark

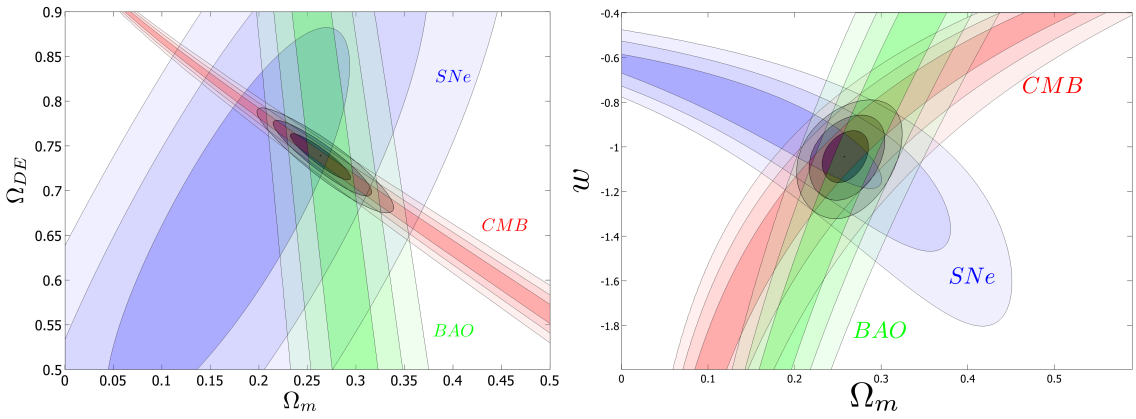

Figure 1.1: SN Ia, CMB, and BAO constraints on Ω_m and Ω_Λ in an open ΛCDM universe (left panel) and on Ω_m and w in a flat universe where the dark energy equation of state is allowed to vary (right panel).

energy constraints expected in the near future.

Chapters 2–4 study systematic effects in dark energy probes, focusing especially on constraints from distance probes like SNe Ia. In Chapter 2, we quantify the effect of current SN Ia systematic errors on dark energy constraints, both for simple parametrizations of the equation of state and for a general description with principal components. We consider both SN-only and combined constraints and find that the SN Ia systematics typically degrade figures of merit by roughly a factor of three, illustrating their importance even for current data. Separately, we consider the effect on constraints of the finite detection significance of the BAO feature.

Chapter 3 investigates recent evidence for a phantom dark energy equation of state using three separate SN Ia compilations (SNLS3, Union2.1, and PS1) in combination with CMB distance information from either WMAP9 or *Planck*. Using this distance information alone, we find nearly 2σ evidence for $w < -1$ when SNLS3 or PS1 is combined with *Planck*. In the process, we introduce new tests to investigate systematic effects. We study the dependence of the constraints on the redshift, stretch, color, and host galaxy stellar mass of SNe, but we find no unusual trends. In contrast, the constraints strongly depend on any external H_0 prior: a higher adopted value for the direct measurement of the Hubble constant ($H_0 \gtrsim 71$ km/s/Mpc) leads to $\gtrsim 2\sigma$ evidence for phantom dark energy. Given *Planck* data, and assuming that ΛCDM is correct, we conclude that either the SNLS3 and PS1 data have systematics that remain unaccounted for or that the Hubble constant is below about 71 km/s/Mpc.

Chapter 4 is concerned with photometric calibration errors in the galaxy power spectrum. We first point out the danger posed by the multiplicative effect of calibration errors,

where large-angle error propagates to small scales and may be significant even if the large-scale information is cleaned or not used in the cosmological analysis. We then propose a method to measure the arbitrary large-scale calibration errors and use these measurements to correct the small-scale (high-multipole) power which is most useful for constraining the majority of cosmological parameters. Using a Fisher matrix formalism, we demonstrate the effectiveness of our approach on synthetic examples and briefly discuss how it may be applied to real data.

Chapters 5–6 focus on tests of the standard ΛCDM model. In Chapter 5, we use goodness-of-fit and Bayesian model comparison techniques with model-independent SN Ia and BAO data to test power law expansion as an alternative cosmological model. We find that neither power law expansion nor ΛCDM is strongly preferred over the other when the SN Ia and BAO data are analyzed separately but that power law expansion is strongly disfavored by the combination. We treat the so-called $R_{\rm h} = ct$ cosmology (a constant rate of expansion) separately and find that it is conclusively disfavored by all combinations of data that include SN Ia observations and a poor overall fit when systematic errors in the SN Ia measurements are ignored, despite a recent claim to the contrary. We discuss this claim and some concerns regarding hidden model dependence in the SN Ia data.

In Chapter 6, we use low-redshift SN Ia data to test for the presence of the peculiar velocity correlations predicted for the standard ΛCDM model. We find no evidence for the presence of these correlations, although, given the significant noise, the data is also consistent with them. We then consider the dipolar component of the velocity correlations — the frequently studied "bulk velocity" — and explicitly demonstrate that including the velocity correlations in the data covariance matrix is crucial for drawing correct and unambiguous conclusions about the bulk flow. In particular, current SN data is consistent with no excess bulk flow on top of what is expected for ΛCDM and effectively captured by the covariance. We further clarify the nature of the apparent bulk flow that is inferred when the velocity covariance is ignored.

CHAPTER 2

Dark Energy with SN Ia Systematic Errors

2.1 Introduction

Since the discovery of the accelerating universe in the late 1990s [8, 9], a tremendous amount of effort has been devoted to improving measurements of dark energy (DE) parameters. As constraints on these parameters improved, controlling the systematic errors in measurements became critical for continued progress. The systematics come in many flavors, including a multitude of instrumental effects and astrophysical effects.

Type Ia supernovae (SNe Ia) were used to discover DE and still provide the best constraints on DE. The advantage of SNe Ia relative to other cosmological probes is that *every* SN provides a distance measurement and therefore some information about DE. More recently, SN Ia observations have been joined by measurements of baryon acoustic oscillations (BAO), which provide exceedingly accurate measurements of the angular diameter distance in redshift bins. Cosmic microwave background (CMB) anisotropies come mostly from high redshift and are thus not particularly effective in probing DE, but they do provide one measurement of the angular diameter distance to redshift $z \simeq 1100$ very accurately. Galaxy clusters also constrain DE usefully, while weak gravitational lensing is expected to become one of the most effective probes of DE in the near future. For recent comprehensive reviews of DE probes, see [15, 16].

In this work, we are interested in studying the effect of SN Ia systematics on DE constraints by including the *covariance* of measurements between different SNe. The covariance includes primarily systematic errors, and for the first time it has been quantified in depth by [17]. Including the effects of the systematic errors, represented by nonzero covariance, weakens the overall constraints on model parameters. Here we wish to explore the effect of systematic errors for general models of DE described by a number of principal components (PCs) of the equation of state, though we first consider these effects for simpler, more commonly used descriptions of the DE sector. We choose to combine the SN

Ia data with BAO and CMB measurements and estimate the effects of *current* systematic errors in SN Ia observations. We then proceed to study another systematic concern that is particularly relevant for BAO: whether the finite significance of the detection of the BAO feature in various surveys, when taken into account, weakens the constraints imposed on DE parameters.

While we closely follow the accounting for the SN Ia systematics from [17], we note that several other analyses have considered the effect of SN systematics. However, most of these analyses only studied the effects of the systematic errors on the constant equation of state (e.g. [17–20]) or included the additional parameter w_a to describe the variation of the equation of state with time (e.g. [21]). Notable exceptions are studies by [22] and [23], which considered a number of specific DE models with non-standard behavior, and [24] and [25], which parametrized the DE density in several redshift bins. Here our goal is to go beyond any specific models and study the effects of systematic errors in current data on DE constraints in the greatest generality possible. While a truly model-independent description of the DE sector is of course impossible, a description of the expansion history in terms of 10 or so parameters – which we adopt in this paper – comes close[1]. In this sense, our paper complements the recent investigations by [26, 27] (see also [28–36]), which studied constraints on very general descriptions of DE using (a slightly different set of) current data but without specific study of the effects of systematic errors.

The paper is organized as follows. In Sec. 2.2, we describe the SN Ia, BAO, and CMB data (and for BAO and CMB, the distilled observable quantities) that we use in our analysis. In Sec. 2.3, we discuss useful parametrizations of DE and compare constraints on the DE parameters with and without systematic errors included in the analysis. In Sec. 2.4, we investigate the effects of the finite detection significance of the BAO feature in galaxy surveys on the cosmological parameter constraints. In Sec. 2.5, we summarize our conclusions.

2.2 Data Sets Used

We begin by describing the data sets used in this analysis. We have used three probes of DE: SNe Ia, BAO and CMB anisotropies.

[1] We do not, however, consider allowing departures from general relativity; doing so would further generalize the treatment.

2.2.1 SN Ia Data and Covariance

Although SNe Ia are not, of course, perfect standard candles, it has long been known that there exist useful correlations between the peak apparent magnitude of a SN Ia and the *stretch*, or broadness, of its light curve (simply put, broader is brighter). The peak apparent magnitude is also correlated with the color of the light curve (bluer is brighter). We therefore model the apparent magnitude of a SN Ia with the equation [37]

$$m_{\rm mod} = 5\log_{10}\left(\frac{H_0}{c}\,d_L\right) - \alpha_s(s-1) + \beta_c\,\mathcal{C} + \mathcal{M}, \tag{2.1}$$

where d_L is the luminosity distance, α_s is a nuisance parameter associated with the measured stretch s of a SN Ia light curve, and β_c is a nuisance parameter associated with the measured color $\mathcal{C}$ of the light curve. The absolute magnitude of a SN Ia is contained within the constant magnitude offset $\mathcal{M}$, which is considered yet another nuisance parameter[2].

Recent work has concentrated on estimating correlations between measurements of individual SN Ia magnitudes. A complete covariance matrix for SNe Ia includes all identified sources of systematic error in addition to the intrinsic scatter and other sources of statistical error. The χ^2 statistic is then given by

$$\chi^2 = \Delta\mathbf{m}^T\mathbf{C}^{-1}\Delta\mathbf{m}, \tag{2.2}$$

where $\Delta\mathbf{m} = \mathbf{m}_{\rm obs} - \mathbf{m}_{\rm mod}(\mathbf{p})$ is the vector of magnitude differences between the observed magnitudes of N SNe Ia $\mathbf{m}_{\rm obs}$ and the theoretical prediction that depends on the set of cosmological parameters $\mathbf{p}$, $\mathbf{m}_{\rm mod}(\mathbf{p})$. Here $\mathbf{C}$ is the $N \times N$ covariance matrix between the SNe. Given a value for χ^2, we assume that the likelihood of a set of cosmological parameters is Gaussian, so that $\mathcal{L}(\mathbf{p}) \propto e^{-\chi^2/2}$. Since $\mathbf{C}$ is a function of parameters α_s and β_c (see below), we would naïvely expect that the inclusion of the Gaussian prefactor $1/\sqrt{\det\mathbf{C}}$ in the likelihood is necessary. However, using simple simulations of parameter extraction with synthetic data, we (and separately [17]) find that including the prefactor leads to significant *biases* in recovered α_s and β_c values. This result, discussed briefly in [17], is in hindsight not surprising given that both the independent variables (stretch and color) and dependent variable (magnitude) have errors; see e.g. [38] for a lengthy discussion. We therefore do not include the $1/\sqrt{\det\mathbf{C}}$ prefactor in our analysis.

Recently [17] determined covariances between SN Ia measurements from the Super-

[2]Throughout the analyses in this paper, we actually marginalize analytically over a model with *two* distinct $\mathcal{M}$ values, where a mass cut of the host galaxy dictates which $\mathcal{M}$ value applies (here we use a mass cut of $10^{10}M_\odot$). This is meant to correct for host galaxy properties and is empirical in nature (see text and Appendix C of [17]). For simplicity, we suppress mention of the second $\mathcal{M}$ parameter.

Source	$N_{\rm SN}$	Range in z
Low-z	123	0.01 - 0.1
SDSS	93	0.06 - 0.4
SNLS	242	0.08 - 1.05
HST	14	0.7 - 1.4

Table 2.1: Summary of SN Ia observations included in this analysis, showing the number of SNe included from each survey and the approximate redshift ranges.

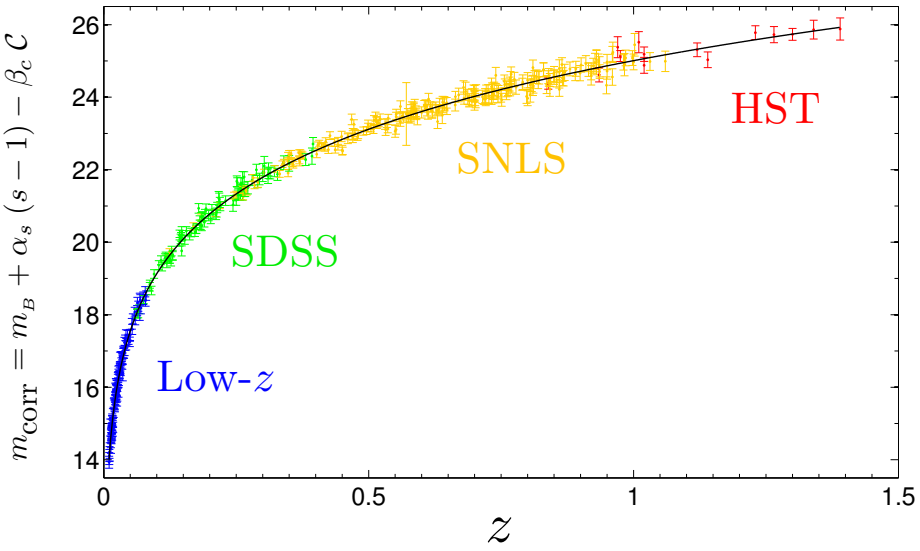

Figure 2.1: Hubble diagram for the compilation of all SN Ia data used in this paper, labeling SNe from each survey separately and showing the (diagonal-only) magnitude uncertainties. The solid black line represents the best fit to the data.

nova Legacy Survey (SNLS). The SN compilation and covariance matrix that resulted from this work will be used in this analysis. The SNLS compilation consists of 472 SNe Ia, approximately one half of which were detected in SNLS, while the rest originated from one of three other sources. These four main sources are summarized in Table 2.1 and illustrated in the Hubble diagram of Fig. 2.1. The low-redshift (Low-z) SNe actually come from a variety of samples as discussed in [17].

The complete covariance matrix from [17] can be written most usefully as the sum of two separate parts, a diagonal part consisting of typical statistical errors and a systematic part, which includes both diagonal and off-diagonal elements. This off-diagonal piece includes some correlated errors which are considered statistical in [17] (since they can be

reduced by including more observations), but here we disregard the distinction and group these errors with the actual systematic errors, which also lead to off-diagonal covariance elements. This simplification is reasonable because the correlated statistical errors are small compared to the (correlated) systematic errors. The diagonal, statistical-only part of the covariance matrix can be expressed as

$$\begin{aligned} D_{ii}^{\rm stat} &= \sigma_{m_B,i}^2 + \alpha_s^2\,\sigma_{s,i}^2 + \beta_c^2\,\sigma_{\mathcal{C},i}^2 + \sigma_{\rm int}^2 \\ &+ \left(\frac{5(1+z_i)}{z_i(1+z_i/2)\log 10}\right)^2 \sigma_{z,i}^2 + \sigma_{\rm lensing}^2 \\ &+ \sigma_{\rm host\ correction}^2 + D_{ii}^{m_B s\,\mathcal{C}}(\alpha_s,\beta_c) \end{aligned} \tag{2.3}$$

In the above, $\sigma_{m_B,i}$, $\sigma_{s,i}$, $\sigma_{\mathcal{C},i}$, and $\sigma_{z,i}$ are the statistical uncertainties of the measured magnitude, stretch, color, and redshift, respectively, of the $i^{\rm th}$ SN. The z term translates the error in redshift into error in magnitude. To include actual intrinsic scatter of SNe Ia and allow for any mis-estimates of photometric uncertainties, the quantity $\sigma_{\rm int}$ is included, with a different value allowed for each sample. The $\sigma_{\rm int}$ values were derived by requiring the χ^2 of the best-fitting (Ω_M,w) cosmological fit to a flat universe to be one per degree of freedom for each sample separately. Also included here are statistical uncertainties due to gravitational lensing and uncertainty in the host galaxy correction.

The contribution $D_{ii}^{m_B s\,\mathcal{C}}(\alpha_s,\beta_c)$ represents a combination of the covariance terms between magnitude, stretch, and color for the $i^{\rm th}$ SN. It is given by

$$D_{ii}^{m_B s\,\mathcal{C}}(\alpha_s,\beta_c) = 2\alpha_s D_{ii}^{m_B\,s} - 2\beta_c D_{ii}^{m_B\,\mathcal{C}} - 2\alpha_s\beta_c D_{ii}^{s\,\mathcal{C}}, \tag{2.4}$$

where $D_{ii}^{m_B\,s}$, $D_{ii}^{m_B\,\mathcal{C}}$ and $D_{ii}^{s\,\mathcal{C}}$ represent the computed magnitude-stretch, magnitude-color, and stretch-color covariances for the $i^{\rm th}$ SN. Note that even the statistical covariance matrix is a function of α_s and β_c, meaning that a proper analysis involves varying the errors (recomputing the covariance matrix) any time α_s and β_c are changed.

A similar equation can be used to construct the systematic covariance matrix, where different systematic terms are combined to produce submatrices which are then added together with specified values for α_s and β_c, as above. The systematic terms include calibration (which is the dominant contribution), Malmquist bias, peculiar velocities, Milky Way dust extinction, contamination of the sample with non-Ia SNe, uncertainties arising from differences in the light-curve fitters, uncertainty in the relationship between host galaxy properties and SN magnitude, evolution of α_s and β_c, and early light-curve photometric uncertainty. The systematic covariance matrix includes diagonal and off-diagonal elements,

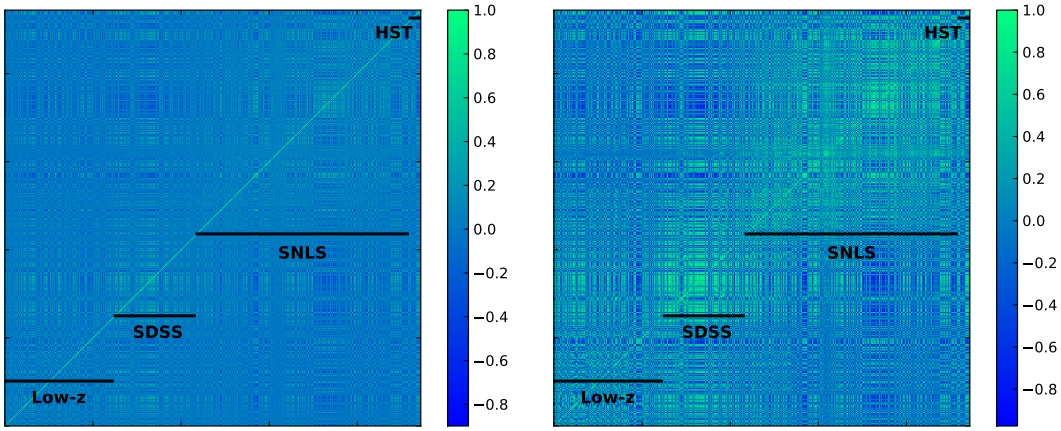

Figure 2.2: Left panel: correlation matrix obtained from the complete covariance matrix $\mathbf{C}^{\rm full}$, sorted first by survey and then by redshift within each survey. Right panel: same, but using only the systematic covariance matrix $\mathbf{C}^{\rm sys}$. In both cases we assume $\alpha_s = 1.43$ and $\beta_c = 3.26$, the best-fit values for the flat $w = \text{const}$ model. The right panel is similar to Fig. 12 from Conley et al. (2011a), but we repeat it here and show the full covariance (left panel) for completeness.

which are calculated (see [17] for more details) using the equation

$$C_{ij}^{\rm sys} = \sum_{k=1}^{K} \left(\frac{\partial m_{{\rm mod}\,i}}{\partial S_k} \right) \left(\frac{\partial m_{{\rm mod}\,j}}{\partial S_k} \right) (\Delta S_k)^2 \,, \tag{2.5}$$

where the sum is over the K systematics S_k, ΔS_k is the size of each term (for example, the uncertainty in the zero point), and $m_{\rm mod}$ is defined in Eq. (2.1). Then the full covariance matrix is simply given by

$$\mathbf{C}^{\rm full} = \mathbf{D}^{\rm stat} + \mathbf{C}^{\rm sys}. \tag{2.6}$$

A plot of the full covariance matrix (constructed using flat $w = \text{const}$ model best-fit values $\alpha_s = 1.43$ and $\beta_c = 3.26$) is shown in Fig. 2.2.

2.2.2 BAO and CMB data

To produce the combined constraints in this paper, we include information from both BAO and the CMB in addition to the SN data. In each case, we choose for simplicity distilled quantities which depend only on Ω_M, $\Omega_{\rm DE}$, Ω_K, and a parametrized $w(z)$.

For BAO, we compare the theoretical prediction for the acoustic parameter $A(z)$ with

Sample	$z_{\rm eff}$	$A_0(z_{\rm eff})$
6dFGS	0.106	0.526 ± 0.028
SDSS DR7	0.20	0.488 ± 0.016
SDSS DR7	0.35	0.484 ± 0.016
WiggleZ	0.44	0.474 ± 0.034
BOSS	0.57	0.444 ± 0.014
WiggleZ	0.60	0.442 ± 0.020
WiggleZ	0.73	0.424 ± 0.021

Table 2.2: Summary of measurements of distilled BAO parameter $A(z)$. We show the survey from which the measurement comes, the effective redshift of the survey (or its subsample), and the measured value A_0.

the measured value, where we define (see [10])

$$A(z) \equiv \left[r^2(z)\frac{cz}{H(z)}\right]^{1/3} \frac{\sqrt{\Omega_M H_0^2}}{cz}, \tag{2.7}$$

where $r(z)$ is the comoving distance to redshift z. We combine recent measurements of $A(z)$ at different effective redshifts, using data from the 6dF Galaxy Survey [11], the Sloan Digital Sky Survey (SDSS) Data Release 7 (DR7) [39], the WiggleZ survey [40, 41], and the SDSS Baryon Oscillation Spectroscopic Survey (BOSS) [42, 43]. The measured values are summarized in Table 2.2.

A plot of the measured values and their uncertainties superimposed on an $A(z)$ curve (Fig. 2.3) suggests that there is no significant tension between the measurements. Note that the SDSS DR7 measurements at $z = (0.2, 0.35)$ are correlated with correlation coefficient 0.337. The WiggleZ measurements are correlated with coefficient 0.369 for the pair $z = (0.44, 0.6)$ and coefficient 0.438 for $z = (0.6, 0.73)$. Ignoring the relatively small overlap in survey volume between SDSS DR7 and the BOSS sample, we expect all other pairwise correlations to be zero. We compute χ^2 in the usual way for correlated measurements, as in Eq. (2.2).

Nearly all of the sensitivity of the CMB to DE comes from the measurement of an angle at which the sound horizon at $z \approx 1100$ is observed (e.g. [44]). This measurement in turn determines the angular diameter distance to recombination with the physical matter quantity, $\Omega_M h^2$, essentially fixed. The latter quantity is popularly known as the CMB shift

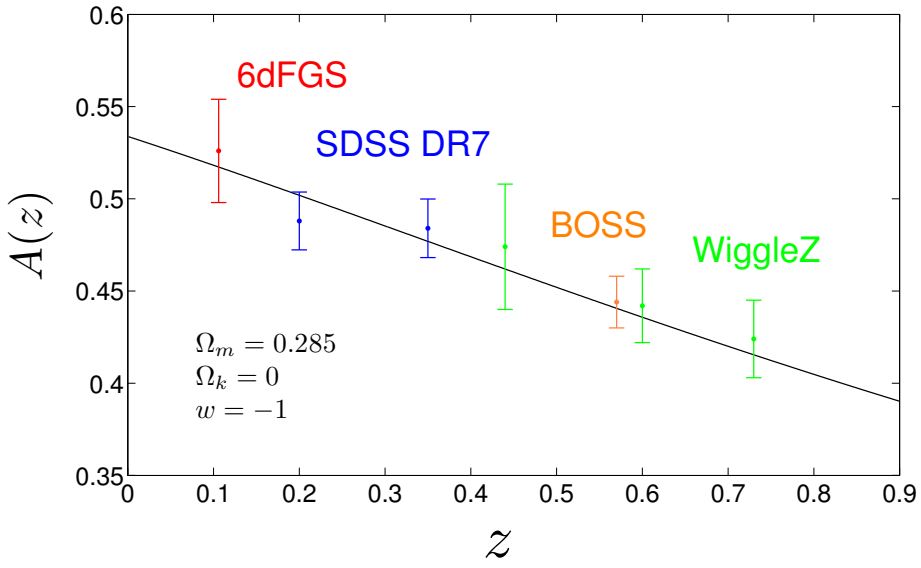

Figure 2.3: Measured values of $A(z)$ and their (diagonal-only) uncertainties for each effective redshift. The black curve shows $A(z)$ for a model that fits the data points well, and the parameters for this model are given in the legend.

parameter R and is defined as

$$R \equiv \frac{\sqrt{\Omega_M H_0^2}}{c}\, r(z_*), \tag{2.8}$$

where $z_* = 1091.3$ is the redshift of decoupling as measured by WMAP7 [45]. We take the measured value of R to be the value determined by WMAP7, $R_0 = 1.725 \pm 0.0184$ [45]. We compute χ^2 in the usual way, comparing this measured value of R with the theoretical prediction.

Calculating the combined SN, BAO, and CMB likelihood is now a simple task. We define $\mathcal{L}_{\rm comb} \propto e^{-\chi^2_{\rm tot}/2}$, where $\chi^2_{\rm tot} = \chi^2_{\rm SN} + \chi^2_{\rm BAO} + \chi^2_{\rm CMB}$.

2.2.3 Parameter constraint methodology

We use two alternate codes to produce our constraints. For the basic constraints, including the constant equation of state of DE or the (w_0, w_a) description, we use a brute-force search which computes likelihoods over a grid of values of ~ 5 parameters (listed below).

Alternatively, we developed a new Markov Chain Monte Carlo (MCMC; e.g. see [46, 47]) code to determine DE parameter constraints and figures of merit (FoMs) for the general (~ 13 parameters) PC description. The MCMC procedure is based on the Metropolis-Hastings algorithm [48, 49]. From the likelihood $\mathcal{L}(\mathbf{x}|\theta)$ of the data $\mathbf{x}$ given each proposed

parameter set θ, Bayes' Theorem tells us that the posterior probability distribution of the parameter set given the data is

$$\mathcal{P}(\theta|\mathbf{x}) = \frac{\mathcal{L}(\mathbf{x}|\theta)\mathcal{P}(\theta)}{\int \mathcal{L}(\mathbf{x}|\theta)\mathcal{P}(\theta)\, d\theta}, \tag{2.9}$$

where $\mathcal{P}(\theta)$ is the prior probability density. The MCMC algorithm generates random draws from the posterior distribution. We test convergence of the samples to a stationary distribution that approximates $\mathcal{P}(\theta|\mathbf{x})$ by applying a conservative Gelman-Rubin criterion [50] of $R - 1 \lesssim 0.03$ across a minimum of four chains for each model class. We use the `getdist` routine of the CosmoMC code [51] to process the resulting chains; `getdist` bins the chains and then smoothes the binned distribution of counts by convolution with a multidimensional Gaussian kernel.

We verified that the two codes give results that are in excellent agreement in several relevant cases, e.g. constraints in the Ω_M–w or w_0–w_a plane.

2.3 Results: Effects Of The Systematics

2.3.1 Preliminaries

Before beginning our discussion of systematics, we briefly consider the vanilla ΛCDM cosmology, where $w = -1$. The cosmological parameters describing the expansion rate are matter and cosmological constant densities relative to critical, Ω_M and Ω_Λ. Including the nuisance parameters, the total parameter set is

$$p_i \in \{\Omega_M, \Omega_\Lambda, \mathcal{M}, \alpha_s, \beta_c\}. \tag{2.10}$$

We combine SN constraints with BAO and CMB constraints and marginalize over the other parameters to map the likelihood of Ω_Λ. We find a mean value $\Omega_\Lambda = 0.724 \pm 0.0114$. This suggests that a universe with zero (or negative) cosmological constant is ruled out at approximately 64-σ! Amusingly, using the brute-force likelihood search that includes the positive and negative values of Ω_Λ, we find that the combined data give a remarkably low likelihood of zero or negative vacuum energy, even allowing for nonzero curvature: $P(\Omega_\Lambda \leq 0) \sim 10^{-267}$. Of course, in reality, the evidence for DE is not nearly this convincing, since the likelihood in the space of cosmological observables is certainly not expected to be Gaussian this far away from the peak and thus would *not* be described by $\mathcal{L}_{\rm comb} \propto e^{-\chi^2_{\rm tot}/2}$ (we discuss a related issue in Sec. 2.4). Nonetheless, it is impressive how

strong the evidence for DE is with current data.

We now discuss how one goes beyond ΛCDM cosmology by parametrizing the DE equation of state.

Previous work on the effect of systematics, such as [17], considered the DE sector parametrized by its energy density relative to critical, $\Omega_{\rm DE}$, and a constant equation of state w. Here, we are particularly interested in extending the DE sector to allow for a time-varying equation of state. We make two alternative choices in addition to the constant equation of state so that the three parametrizations we consider are:

1. Constant equation of state, $w = \text{constant}$;
2. Equation of state described with w_0 and w_a [52], so that $w(a) = w_0 + w_a(1-a)$;
3. Equation of state described by a finite number of principal components of $w(z)$ [53].

We now describe in more detail the different parametrizations of DE that we consider (constant w, w_0 and w_a, PCs) and then proceed to analyze the effects of SN systematics on parameter constraints.

2.3.2 Constant w

Assuming that DE can be described by an equation of state w that is constant in time, and assuming a flat universe, we calculate the SN-only likelihood in the Ω_M–w plane. We marginalize over the usual nuisance parameters $\mathcal{M}$, α_s, and β_c.

The results for SN-only constraints on Ω_M and w are shown in Fig. 2.4, where we illustrate the effect of the systematics by showing constraints from the full covariance matrix $\mathbf{C}^{\rm full}$ on top of those which assume only the diagonal statistical uncertainties $\mathbf{D}^{\rm stat}$. The systematic uncertainties broaden the well-determined direction in the Ω_M-w plane without elongating the poorly determined direction much. Constraints in either parameter are not appreciably shifted. The marginalized uncertainty for w is $\sigma_w = 0.17$ for statistical errors only and $\sigma_w = 0.20$ when systematic errors are included. Thus, even though systematic errors increase the area of the contours in the Ω_M–w plane by more than a factor of two, they only increase the uncertainty of w by about 20%.

We also seek to understand how SN systematics influence the stretch and color parameters α_s and β_c, not only because these correlations are what make SNe Ia useful standard candles, but also because it is expected that systematics could potentially affect these correlations. In Fig. 2.5, we marginalize over $\mathcal{M}$, Ω_M, and w to show constraints on the stretch and color coefficients α_s and β_c. Of particular interest is the color coefficient β_c, which

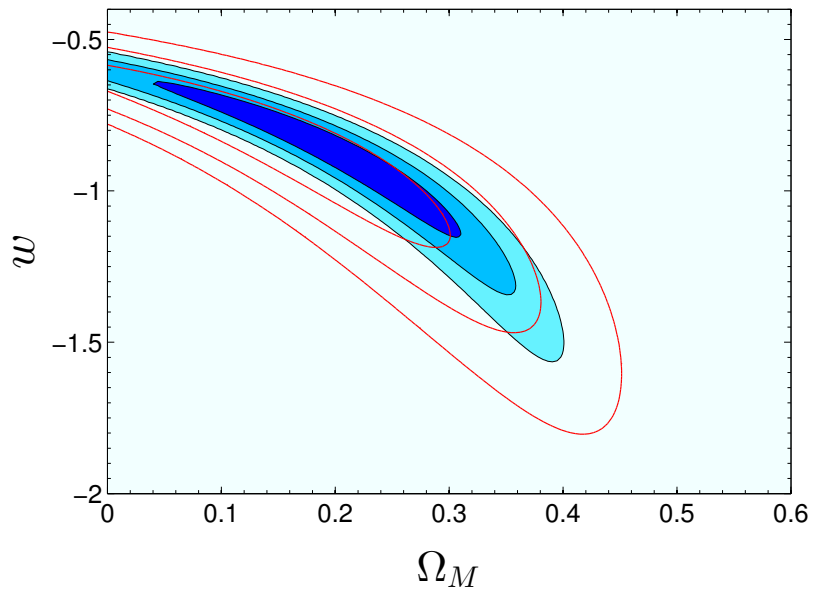

Figure 2.4: 68.3%, 95.4%, and 99.7% likelihood constraints on Ω_M and w, assuming a constant value for w and a flat universe. We use only SN data and marginalize over the nuisance parameters. We compare the case of diagonal statistical errors only (shaded blue) with the full covariance matrix (red).

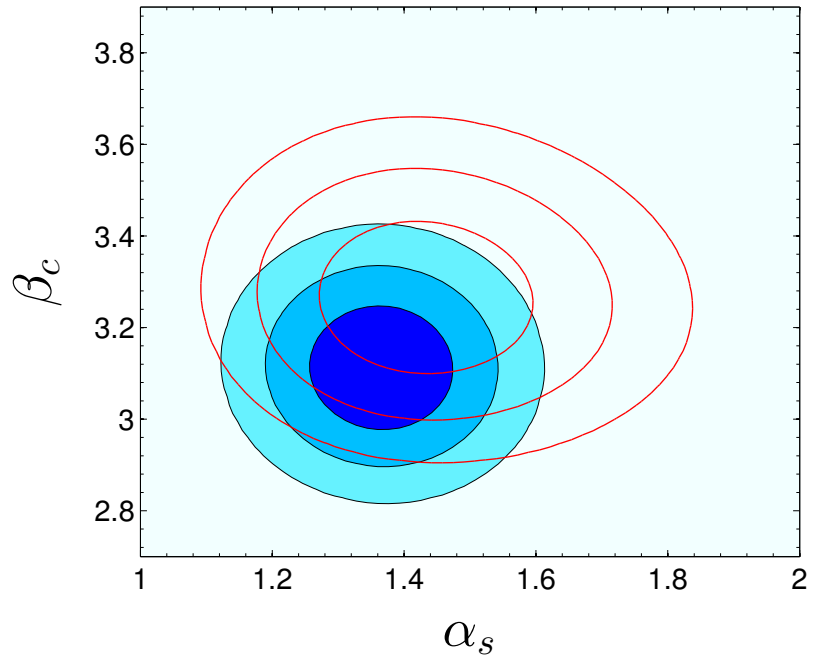

Figure 2.5: 68.3%, 95.4%, and 99.7% likelihood constraints on α_s and β_c, assuming a constant value for w and a flat universe. We use only SN data and marginalize over $\mathcal{M}$, Ω_M, and w. We compare the case of diagonal statistical errors only (shaded blue) with the full covariance matrix (red).

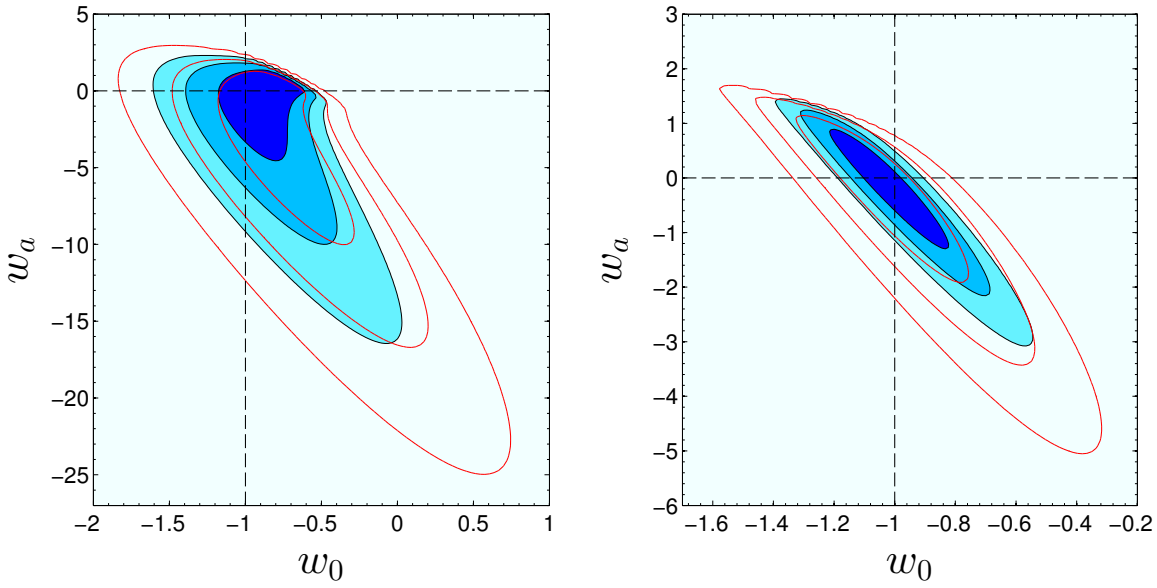

Figure 2.6: 68.3%, 95.4%, and 99.7% likelihood constraints on w_0 and w_a in a flat universe, marginalized over Ω_M and the nuisance parameters. The left panel shows SN-only constraints, while the right panel shows combined SN+BAO+CMB constraints. The shaded blue contours represent constraints with only statistical SN errors assumed ($\mathbf{D}^{\rm stat}$), while the red contours represent the full SN covariance matrix ($\mathbf{C}^{\rm full}$). Note that the ΛCDM model $(w_0, w_a) = (-1, 0)$, represented by the black dashed lines, is fully consistent with the data.

$\mathrm{FoM}^{(w_0\,w_a)}$	$\mathbf{D}^{\mathrm{stat}}$	$\mathbf{C}^{\mathrm{full}}$
SN	2.28	1.16
SN+BAO+CMB	32.9	11.8

Table 2.3: Values of the FoM (Eq. (2.12)) for SN alone (middle row) and SN+BAO+CMB (bottom row). The middle column shows the FoMs for the statistical covariance matrix $\mathbf{D}^{\mathrm{stat}}$ only, while the right column shows the FoMs for the full covariance matrix $\mathbf{C}^{\mathrm{full}}$. Note that including the systematics reduces the FoM by a factor of two to three.

is broadly consistent with values found previously; the systematic errors shift it slightly upwards and increase errors in both parameters by a modest amount.

2.3.3 w_0 and w_a

We wish to understand the constraints on the redshift dependence of $w(z)$, so we allow $w(z)$ to have the form [52, 54]

$$w(z) = w_0 + w_a\, z/(1+z). \tag{2.11}$$

Constraints on w_0 and w_a in a flat universe are shown in Fig. 2.6. The shaded blue contours represent constraints with only statistical SN errors assumed ($\mathbf{D}^{\mathrm{stat}}$), while the red contours ($\mathbf{C}^{\mathrm{full}}$) additionally include the systematic errors. The left panel shows SN-only constraints, while the right panel shows constraints when BAO and CMB information is also included.

The figure of merit (FoM) for this model defined by the Dark Energy Task Force (DETF) [55, 56] is the inverse of the area of the 95.4% confidence level region A_{95} in the w_0–w_a plane; to be slightly more specific, we instead define the FoM as in [27] as

$$\mathrm{FoM}^{(w_0\,w_a)} \equiv (\det \mathbf{C})^{-1/2} \approx \frac{6.17\pi}{A_{95}}. \tag{2.12}$$

The approximate equality in Eq. (2.12) becomes exact for a Gaussian posterior distribution, in which case our FoM is equivalent to the DETF FoM. The FoMs for various scenarios in the w_0–w_a plane are given in Table 2.3. We find that including the systematic errors reduces the FoM by about a factor of two to three.

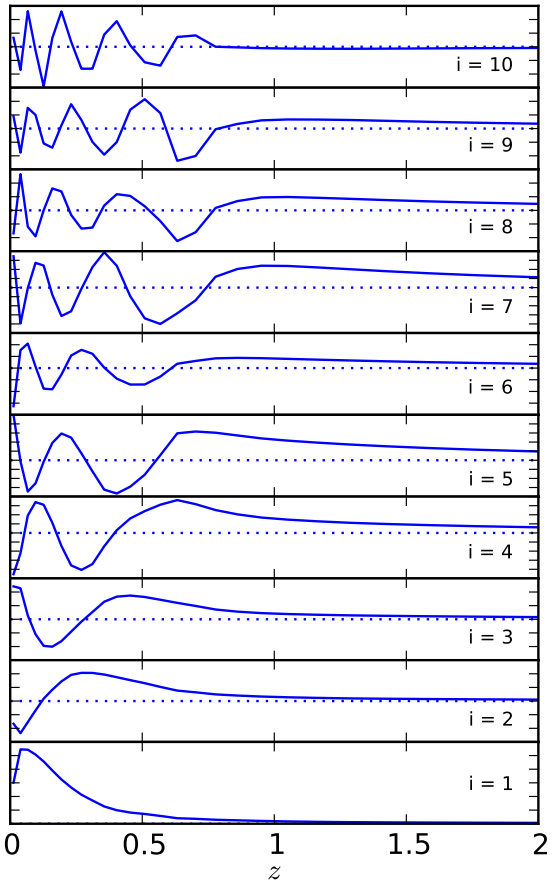

Figure 2.7: The first 10 PCs, $e_1(z)$–$e_{10}(z)$, used in our analysis, in order of increasing variance (bottom to top). The PCs were obtained assuming the observable quantities centered at the fiducial ΛCDM model, but with actual errors from the current data. See text for details.

2.3.4 Principal Components

We now describe the methodology of how to calculate and constrain the principal components of DE [53], which are weights in redshift ordered by how well they are measured by a given cosmological probe and with a given survey.

Following e.g. [26], we first precompute the PCs assuming the current data *centered at a fixed fiducial model* (we choose the standard flat ΛCDM model with $\Omega_M = 1-\Omega_\Lambda = 0.25$). For this precomputation, we include data from all probes (SN+BAO+CMB) and use all identified SN errors. We follow the procedure set forth by the Figure of Merit Science Working Group (FoMSWG) [57] and parametrize $w(z)$ by 36 piecewise constant values in bins uniformly spaced in scale factor a in the range $0.1 \leq a \leq 1.0$. We fix (i.e. ignore) all other parameters in the FoMSWG except for Ω_M and the SN Ia nuisance parameter[3] $\mathcal{M}$ because they are not probed by the SN Ia data, and at the same time they are effectively marginalized over in the BAO and CMB data in the distilled observable quantities, $A(z)$ and R respectively. We fix curvature to zero.

We therefore have a 38×38 Fisher matrix (or really a 45×45 Fisher matrix with seven parameters fixed), corresponding to parameters

$$p_i \in \{w_1, \ldots, w_{36}, \Omega_M, \mathcal{M}\}. \tag{2.13}$$

We marginalize over Ω_M and $\mathcal{M}$ and then diagonalize the remaining 36-dimensional Fisher matrix of the piecewise constant w parameters. The resulting eigenvectors – shapes that describe $w(z)$ – are the PCs $e_i(z)$, and we show the 10 best-determined of these PCs, $e_1(z)$–$e_{10}(z)$, in Fig. 2.7.

The equation of state can be described as [58]

$$1 + w(z) = \sum_{i=1}^{N} \alpha_i e_i(z), \tag{2.14}$$

where α_i are amplitudes for each PC $e_i(z)$. While the Fisher matrix tells us the best accuracy to which these PCs are measured using the assumed data set (these accuracies are related to the eigenvalues λ_i via $\sigma(\alpha_i) = \lambda_i^{-1/2}$), we are not interested in this; rather, we would like to constrain the PCs using actual current data.

We then feed the shapes in redshift of the first several PCs to the MCMC procedure to

[3] In the Fisher matrix precomputation of the PCs we assume a single $\mathcal{M}$ parameter as per usual practice (and following the FoMSWG parametrization), but in the actual constraints on the cosmological parameters we adopt *two* such parameters as described in Sec. 2.2.1. To the extent that the PCs will be correlated anyway due to the differences between real data and assumed "data" going into the Fisher matrix, this subtle difference will be unimportant.

constrain these (and a few other, non-$w(z)$) parameters.

Finally, in our parameter search we impose weak priors on the PCs. Following [58] we impose a hard-bound prior on each α_i, enforcing its contribution to excursions in the equation of state to the region $|1 + w(z)| \leq 1$. This approach yields top-hat priors of width [27]

$$\Delta\alpha_i = \frac{2}{N_{z,\mathrm{PC}}} \sum_{j=1}^{N_{z,\mathrm{PC}}} |e_i(z_j)| \tag{2.15}$$

centered at $w(z) = -1$ or $\alpha_i = 0$. As we will demonstrate, these priors are much wider than the allowed ranges for many of the individual PCs, meaning that our principal results are largely unaffected by the prior (Indeed, we verified this explicitly by constraining the PCs without the prior).

The pairwise constraints on all 13 parameters (Ω_M, the PC amplitudes $\alpha_1 - \alpha_{10}$, and the nuisance parameters α_s and β_c) are shown in Fig. 2.8. The black curves represent constraints from the diagonal statistical SN errors only, while the red curves correspond to the full SN covariance matrix. Overall, the systematic errors broaden and shift the contours slightly.

In Fig. 2.9, we show the individual marginalized constraints on the 10 PC amplitudes. When we assume only diagonal statistical errors, three PCs have a ratio of error to the rms value of the top-hat prior less than 1/3, and six PCs have a ratio less than 1/2. For the full covariance case, two and five PCs have error/prior ratios less than 1/3 and 1/2, respectively. From this, we are extremely encouraged by the fact that constraints on several PCs are very good even with current data, a result incidentally also found by [26] using a slightly different combined "current" data set that, most notably, did not include the BOSS and WiggleZ BAO measurements. Here we again see that the SN systematics broaden the constraints slightly; however, as we show just below, the cumulative effect of the systematics on the FoM is not negligible.

We finally calculate the generalization of the DETF FoM to PCs. As defined in [27],

$$\mathrm{FoM}_n^{(\mathrm{PC})} \equiv \left(\frac{\det \mathbf{C}_n}{\det \mathbf{C}_n^{(\mathrm{prior})}} \right)^{-1/2}, \tag{2.16}$$

where $\mathbf{C}_n$ is the $n \times n$ covariance submatrix of n PCs and

$$\det \mathbf{C}_n^{(\mathrm{prior})} = \prod_{i=1}^{n} \left(\frac{\Delta\alpha_i}{\sqrt{12}} \right)^2$$

is the determinant of the top-hat prior covariance for the n PC coefficients. Each

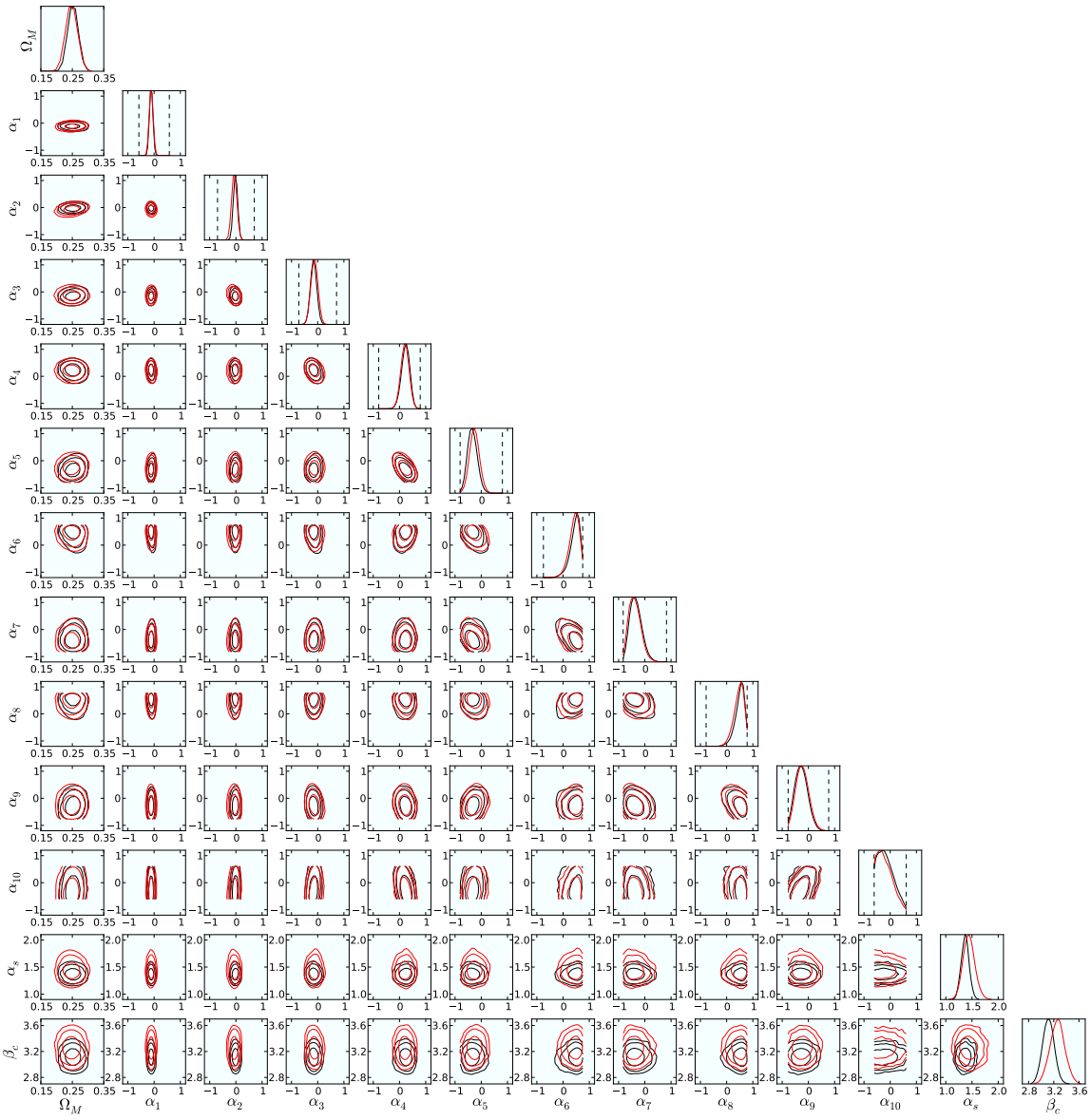

Figure 2.8: 68.3%, 95.4%, and 99.7% likelihood constraints for all pairwise combinations of the 13 cosmological parameters using the combined SN+BAO+CMB data. Diagonal boxes show the 1D marginalized likelihood for each parameter. The black contours illustrate the case of diagonal statistical SN errors only ($\mathbf{D}^{\rm stat}$), while the red contours ($\mathbf{C}^{\rm full}$) also include the systematic SN covariance matrix. The parameter ordering is (top to bottom, or left to right): matter density relative to critical Ω_M, the 10 PC amplitudes α_1–α_{10}, and the stretch and color nuisance parameters α_s and β_c. Note the good constraints on all parameters except for the last few PC amplitudes.

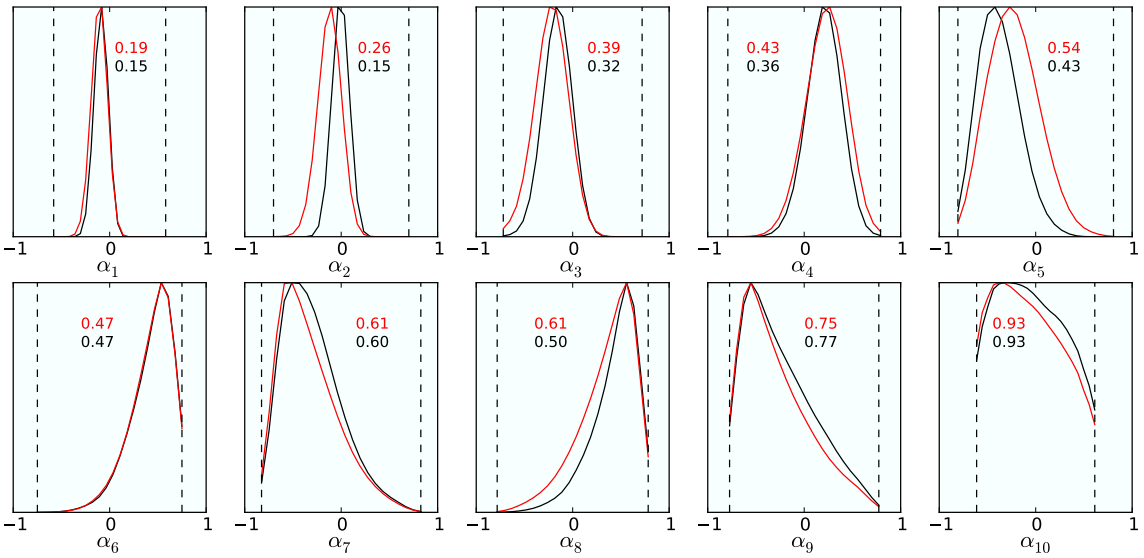

Figure 2.9: Marginalized SN+BAO+CMB constraints on the 10 PC amplitudes. The dashed vertical lines represent the prior limits. Black curves represent constraints from the diagonal statistical SN errors only, while the red curves correspond to the full SN covariance matrix. The black and red number in each panel shows the ratio of the PC error to the rms of the top-hat prior for the statistical-covariance and full-covariance case, respectively. Note the good constraints on all PC amplitudes except for the last few.

$(\Delta\alpha_i/\sqrt{12})^2$ term refers to the rms value of the top-hat prior, where $\Delta\alpha_i$ is the width of the top-hat prior as calculated in Eq. (2.15).

FoM results are shown in Fig. 2.10, where we show the FoM as a function of the number of PCs included. The top panel shows the FoMs with and without SN systematic errors, while the bottom panel shows the corresponding ratios of the two cases. We see that the FoM degradation with the addition of SN systematic errors asymptotes to about a factor of three to four when about five PCs are included and after that remains relatively constant. We therefore conclude that only the few lowest PCs are affected by current systematic errors. We suspect that this is due to the fact that the effect of the systematics is relatively smooth in redshift, and therefore systematics do not become degenerate with the higher PCs that wiggle in z (see the PC shapes in Fig. 2.7). It is somewhat fortuitous that higher ($n \gtrsim 5$) PCs seem to be unaffected by systematics, since it is precisely those higher PCs that are difficult to measure accurately; however, it may be the case that systematics in future data will behave differently and affect the higher components.

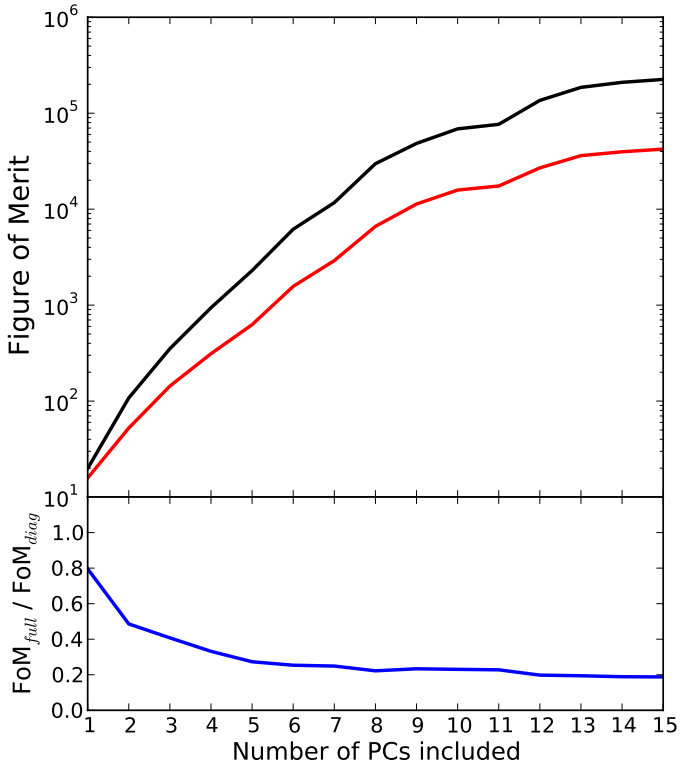

Figure 2.10: Top panel: FoM as a function of the number of PCs included, with the black line showing the statistical-only FoM and the red line showing the FoM with systematics included (See Eq. (2.16) for the definition of the FoM). Bottom panel: ratio of the FoM with systematic errors considered in the SN Ia data to that with only statistical errors considered. BAO and CMB constraints were included in both cases. Notice that the FoM ratio levels off after approximately five PCs have been included. Note that here we have considered the first 15 PCs (as opposed to 10 in Figs. 2.7-2.9) to show that the FoM indeed flattens off as the PCs become very poorly constrained.

2.4 Effect of Finite Detection Significance of BAO

In an interesting paper, [59] pointed out that for marginal detections of cosmological observable quantities, a Gaussian assumption for the likelihood may be a poor one, especially for models that are several-σ away from the central value of the observed quantity. This happens because the usual Gaussian likelihood implicitly ignores the possibility that the observed quantity has *not* actually been detected in the data at all. That possibility may have non-negligible probability, and in that case a flat likelihood in the observable may be more appropriate. In other words, writing a total likelihood of parameters $\mathbf{p}$ as a function of data vector $\mathbf{d}$, we have

$$P(\mathbf{p}|\mathbf{d}) = P_{\rm detect}\, P(\mathbf{p}|\mathbf{d}, {\rm detect}) + (1 - P_{\rm detect})\, P(\mathbf{p}|\mathbf{d}, {\rm noise}), \tag{2.17}$$

where $P_{\rm detect}$ is the probability that the observable quantity has actually been detected and $P(\mathbf{p}|\mathbf{d}, {\rm detect})$ is the likelihood of the cosmological parameters in that case. The cosmological parameter likelihood $P(\mathbf{p}|\mathbf{d}, {\rm noise})$ corresponds to the case that the observable feature was actually noise, and it can be represented by a flat distribution in the parameters $\mathbf{p}$. *Most BAO analyses effectively assume that* $P_{\rm detect} = 1$, thus ignoring the higher-than-expected tail in the overall likelihood coming from the nonzero second term on the right-hand side of Eq. (2.17). If the BAO feature has been detected at very high significance, then this is a good assumption, but it is not *a priori* clear that this is the case with all of the current BAO surveys which typically have several-σ detection significances.

To account for the diminished power of the observations to discriminate between cosmological models when detection significance is not high, [59] suggest a fitting function which replaces the usual Gaussian χ^2 expression $\Delta\chi^2_G$ with

$$\Delta\chi^2 = \frac{\Delta\chi^2_G}{\sqrt{1 + \left(\frac{\rm S}{\rm N}\right)^{-4} \Delta\chi^4_G}}, \tag{2.18}$$

where ${\rm S}/{\rm N}$ is the signal-to-noise ratio or detection significance of the observable feature or quantity. With this prescription, the quantity $\Delta\chi^2$ is equal to its Gaussian counterpart for departures from the best-fit model that are small compared to the signal-to-noise of the observed feature, but it asymptotes to a constant "tail" $({\rm S}/{\rm N})^2$ in the opposite limit, when $\Delta\chi^2_G \gg ({\rm S}/{\rm N})^2$.

Here we apply this reasoning to the measurement of the BAO feature. The significances of the detection of the BAO feature are $2.4\,\sigma$ (corresponding to ${\rm S}/{\rm N} = 2.4$) for 6dF [11],

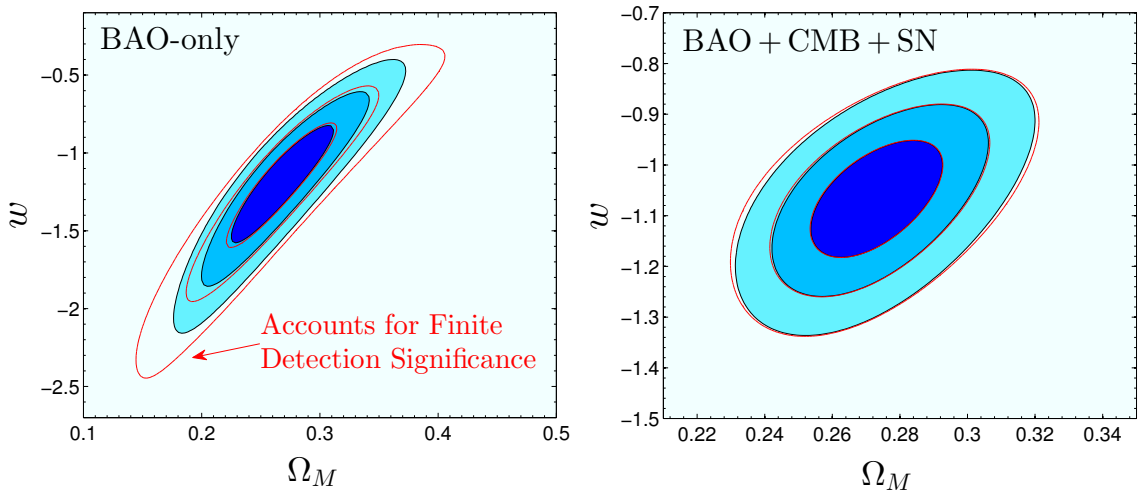

Figure 2.11: Effects on the BAO-only (left panel) and BAO+CMB+SN (right panel) constraints in the Ω_M–w plane with (red) and without (shaded blue) the finite detection significances of the BAO features taken into account. Note that the differences are modest in the BAO-only case and negligible in the combined case.

2.8 σ for WiggleZ [41] (combined for three redshift bins), 3.6 σ for SDSS [39] (combined for two redshift bins), and 5.0 σ for BOSS [43]. We expect that, once the probability of non-detection of the BAO feature has been included, the BAO constraints will change, especially for surveys with lower significance of detection and for 99.7% contour regions. This has in fact been confirmed by [59] for the case of the SDSS BAO data alone.

Fig. 2.11 shows the BAO-only (left panel) and BAO+CMB+SN (right panel) constraints in the Ω_M–w plane with and without the finite detection of the BAO features taken into account[4]. Note that the difference is modest in the BAO-only case and negligible in the combined case. This is as expected, especially given that some of the strongest BAO data sets (e.g. BOSS) also have the highest detection significances of the BAO feature.

Note also that there is nothing BAO-specific to the effects of the finite detection significance. While the CMB is detected with very high confidence and thus does not warrant a similar analysis, it could be applied to SNe Ia where, for example, a few percent of SNe may not be Type Ia[5]. Given the full probabilistic classification of each SN on whether or not it is Type Ia [60, 61], one could carry out a similar analysis, which in this context would be how imperfect purity of the SN Ia sample affects the constraints on cosmological parameters. We suspect the results would be even less discrepant relative to the usual

[4]The results in the w_0–w_a plane are qualitatively similar, and we do not show them here.

[5][17] find that the fraction of non-Ia SNe rises from zero at low redshift to $O(10\%)$ at $z \sim 1$; however, their modeling is very conservative, and the true fraction of non-Ia SNe is likely very small in the current data sets.

perfect-detection analysis than in the case of BAO, and we do not pursue such an analysis in this paper.

In conclusion, the finite detection significance of the BAO feature in large-scale structure surveys leads to a small but discernible weakening of the constraints on cosmological parameters.

2.5 Conclusions

In this paper, we have investigated the effects of systematic errors in current SN Ia observations on DE parameter constraints. We accounted for the systematic errors in SN Ia observations, including the effects of photometric calibration, dust, color, gravitational lensing, and other systematics by adopting a fully off-diagonal covariance matrix between ~ 500 SNe from the SNLS compilation (see Fig. 2.2). We extended the similar analysis from [17] by constraining the temporal evolution of the equation of state of DE described by the pair of parameters (w_0, w_a) as well as a much richer description in terms of 10 PCs of the equation of state (shown in Fig. 2.7). We combined the SN Ia constraints with data from BAO from four different surveys (see Fig. 2.3) as well as the principal information on DE given by the acoustic peak measurements of the CMB anisotropies measured by the WMAP experiment.

The constraints on the simple parametrizations of DE are affected by the systematics, but the overall constraints are still strong even after their inclusion (see Figs. 2.4 and 2.6). More importantly, we found that systematic errors affect the constraints somewhat, reducing the w_0–w_a FoM by a factor of about three (see Table 2.3), while the generalized PC-based FoM is degraded by a factor of three to four (see Fig. 2.10). However, as the PC analysis shows, this degradation is mainly restricted to the first few numbers (PC amplitudes) describing DE. In fact, what is particularly impressive about current data is that roughly five PCs are well-constrained even in the presence of systematic errors (see Figs. 2.8 and 2.9).

In the spirit of testing for systematic effects in current data constraining DE, we also wondered if the relatively low detection significances of BAO features, ranging from about $2.4\,\sigma$ to $5.0\,\sigma$ in various surveys, change the overall cosmological constraints. While not a systematic error *per se*, the small but non-negligible probability that the BAO feature has not been detected in some of these surveys implies that the posterior probability of cosmological parameter values asymptotes to a small but nonzero value far from the likelihood peak [59]. We find that, while the BAO-only constraints are somewhat affected, the combined constraints are not (see Fig. 2.11).

From all this, we conclude that current systematic errors do degrade DE constraints and FoMs, but not in a major way. Given that future constraints are forecasted to be much better, continued control of current systematic errors remains key for progress in characterizing DE.

CHAPTER 3

Distance Probes and Evidence for Phantom Dark Energy

3.1 Introduction

A key question in understanding the mechanism behind the acceleration of the Universe is the value of the dark energy equation of state, the ratio of pressure to energy density for dark energy: $w \equiv p_{\rm DE}/\rho_{\rm DE}$. Measurements so far [18–20, 22–25, 62–66] have generally been in good, even excellent, agreement with $w = -1$, the value corresponding to the vacuum energy density described by the famous cosmological-constant term in Einstein's equations of general relativity. Any measured departure from this value would not only profoundly shake up our understanding of the Universe, but also provide an important hint in our quest to understand cosmic acceleration.

It is therefore particularly important to measure the equation of state and search for any evidence of its variation in time. Over the past decade, there were several clear instances in which the measurements indicated that $w < -1$ at $\gtrsim 2\sigma$ evidence [28, 67–69], though eventually these departures either were explained by known systematics in the data or quietly went away as new and better data became available. More recently, with the release of the first results from Planck [7], other such claims have been presented, such as [70], which features high-quality data and a careful analysis including systematic errors [71] (see also [72, 73]). This motivates us to investigate the current data in some detail, concentrating especially on the value of w marginalized over other cosmological parameters.

The principal tool for studying the equation of state is the combination of three of the most mature probes of dark energy: Type Ia supernovae (SNe Ia), baryon acoustic oscillations (BAO), and cosmic microwave background (CMB) anisotropies. SNe Ia and BAO probe expansion at low and intermediate redshifts and are thus a crucial ingredient in studying dark energy. The CMB measurements effectively probe a single high-redshift distance (specifically, the distance to the surface of last scattering), which is crucial mainly

because it provides complementary information to break degeneracy in the Ω_m–w plane. For comprehensive reviews of dark energy probes, see [15, 16].

The rest of the paper is organized as follows. In Sec. 3.2, we describe the SN Ia, BAO, and CMB data that we use in our analysis. In Sec. 3.3, we present our results for the constraints on a constant dark energy equation of state along with several further analyses that were performed. In Sec. 3.4, we summarize and discuss our findings.

3.2 Data Sets

We begin by describing the data sets used in this analysis. We have used the three most mature probes of dark energy: SNe Ia, BAO, and CMB anisotropies. We focus on these three probes since they remain the most mature, well-studied, and robust dark energy probes at present. Furthermore, they are expected to be statistically independent for all practical purposes. Finally, being purely geometric in nature, they measure dark energy only through its effect on expansion history; therefore they are understood intuitively and may bypass certain systematic effects, such as those involved in growth of structure measurements, which are not very well understood.

3.2.1 SN Ia data

SNe Ia were used to discover dark energy [8, 9] and still provide the best constraints on dark energy. SNe Ia are very bright standard candles that are useful for measuring cosmic distances.

SNe Ia constrain cosmology by providing essentially one measurement each of the luminosity distance $D_L(z) = (1+z)\, r(z)$ to the redshift of the SN. The theoretical apparent magnitude is then given by

$$m_{\rm th}(z) = 5 \log_{10} \left(\frac{H_0}{c} D_L(z) \right) + \mathcal{M} \,, \tag{3.1}$$

where the constant magnitude offset $\mathcal{M}$ is a nuisance parameter that depends on both the absolute magnitude of a SN Ia and the Hubble constant H_0. It has long been known that there exist useful correlations between the peak absolute magnitude of a SN Ia and both the stretch (or broadness) and photometric color of its light curve. Simply put, a broader or bluer SN light curve corresponds to a brighter SN. Thus we compare the theoretical

apparent magnitude with the measured magnitude after light-curve correction:

$$m_{\text{corr}} = m_B + \alpha \times (\text{stretch}) - \beta \times (\text{color}) \,, \tag{3.2}$$

where the stretch and color measures are specific to the light-curve fitter employed (e.g. SALT2 [37] or SiFTO [74]) and where α and β are two additional nuisance parameters.

Recent work has concentrated on estimating correlations between measurements of individual SN Ia magnitudes as a way of accounting for the numerous systematic effects which must be controlled in order to improve SN Ia constraints significantly beyond their current level [1]. A complete covariance matrix for SNe Ia includes all identified sources of systematic error in addition to the intrinsic scatter and other sources of statistical error. The χ^2 statistic is then given by

$$\chi^2 = \Delta\mathbf{m}^{\intercal}\mathbf{C}^{-1}\Delta\mathbf{m} \,, \tag{3.3}$$

where $\Delta\mathbf{m} = \mathbf{m}_{\text{corr}} - \mathbf{m}_{\text{th}}(\mathbf{p})$ is the vector of differences between the observed, corrected magnitudes $\mathbf{m}_{\text{corr}}$ of N SNe Ia and the theoretical predictions $\mathbf{m}_{\text{th}}(\mathbf{p})$ that depend on the set of cosmological parameters $\mathbf{p}$. Here, $\mathbf{C}$ is the $N \times N$ covariance matrix between individual SNe.

In this analysis, we compare current SN Ia data from three separate compilations: the Union2.1 compilation from the Supernova Cosmology Project, the three-year compilation from the Supernova Legacy Survey (SNLS3), and the compilation of the first SN sample from the Pan-STARRS1 survey (PS1).

3.2.1.1 Union2.1

The Union2.1 compilation [25] from the Supernova Cosmology Project[1] improves on the previous Union2 compilation [24] by introducing 27 additional SNe at high redshift, making it both the largest compilation (580 SNe) and the one with the most high-redshift SNe ($\sim$30 at $z \gtrsim 1$). The compilation combines several different samples in each redshift region (low, intermediate, and high), making the redshift coverage very complete but also making the compilation very inhomogeneous.

For this analysis, we include all identified systematic errors via the covariance matrix provided. The SN magnitudes have been pre-corrected for stretch and color using best-fit values for α and β, and we have verified that our SN-only constraints match those presented in [25].

[1] http://supernova.lbl.gov/Union/

3.2.1.2 SNLS3

Results from the first three years of the Supernova Legacy Survey include measurements of $\sim$250 SNe at intermediate-to-high redshifts. When combined with $\sim$100 low-redshift SNe, $\sim$100 SNe from the Sloan Digital Sky Survey (SDSS), and $\sim$10 high-redshift SNe from the Hubble Space Telescope, they produce a compilation [17] of 472 SNe with good redshift coverage out to $z \sim 1$ and some SNe extending to $z \simeq 1.4$. The SNLS3 compilation contains the largest homogeneous sample and includes many of the best-measured SNe along with a detailed analysis of systematic errors [17]. Note that the SNLS3 and SDSS samples have been recalibrated [75] and that new cosmological results, including the full SDSS sample, are forthcoming.

We use the SN Ia data and covariance matrices provided[2] to compute the full covariance matrix, which includes all identified sources of statistical and systematic error. Like the corrected SN magnitudes, the covariance matrix is a function of the light-curve nuisance parameters α and β. For practical reasons, and for a fairer comparison with other SN Ia data sets, we fix these parameters at their best-fit values ($\alpha = 1.43$, $\beta = 3.26$) throughout the analysis. It is worth noting that completely marginalizing over these parameters (varying them both when computing the corrected magnitudes and when building the covariance matrix) has a negligible effect on constraints in our parameter space. We verify that our SN-only constraints match those in [1, 17], where α and β are varied.

It is important to note that, in constraints with SNLS3, we follow the prescription in [17] and marginalize over a model with two distinct $\mathcal{M}$ parameters, where a mass cut ($10^{10} M_{\odot}$) of the host galaxy dictates which $\mathcal{M}$ applies. This is meant to correct for environmental dependencies of SN Ia magnitudes on host galaxy properties and is empirical in nature. We discuss and investigate this issue further in Sec. 3.3.3.

3.2.1.3 PS1

The primary goal of the Panoramic Survey Telescope and Rapid Response System (Pan-STARRS) is to detect Solar System objects by making precise, repeated observations of a wide field of view. These observations also lead to the discovery of SNe Ia, which can be spectroscopically confirmed in follow-up observations. Recently-published SN results from the first 1.5 years of the Pan-STARRS1 Medium Deep Survey include a compilation [70] of 313 SNe, 112 of which were discovered via Pan-STARRS. The rest (201 SNe) come from a combination of low-redshift samples. Aside from the low-redshift anchor, all SNe come from the same instrument, making this compilation very homogeneous. A full

[2] https://tspace.library.utoronto.ca/snls

systematic analysis is described in [71]. Due to the smaller number of SNe and the lack of high-redshift SNe, the PS1 compilation is not competitive with current constraints from Union2.1 or SNLS3, but the survey is ongoing and this will eventually change. The current compilation nevertheless provides good constraints on a constant-w model of dark energy when combined with other probes, so we study it here.

We use the SN Ia data provided[3] and adopt the covariance matrix to account for all identified systematic errors. As with Union2.1, the SN magnitudes have been pre-corrected for stretch and color, and we have verified that our SN-only constraints agree with those in [70].

3.2.2 BAO data

Baryon acoustic oscillations (BAO) are the regular, periodic fluctuations of visible matter density in large-scale structure (LSS) resulting from sound waves propagating in the early Universe. In recent years, measurements of BAO have proven to be useful geometric probes of dark energy. A measurement of the position of the BAO feature in the LSS power spectrum or correlation function basically provides a precise measurement of a spherically-averaged comoving distance to the effective redshift of the survey. New measurements over a wide range of redshifts are making it possible to map expansion history with the BAO distance, analogous to the way SNe Ia map expansion with luminosity distance. For our BAO constraints, we combine recent measurements of the BAO feature from the Six-degree-Field Galaxy Survey (6dFGS) [11], the SDSS Luminous Red Galaxies (SDSS LRG) [76], and the SDSS-III DR9 Baryon Oscillation Spectroscopic Survey (BOSS) [43].

Different authors report their measurement of the BAO feature using different distilled observable quantities. The surveys included here report constraints on the quantity $r_s(z_d)/D_V(z)$ or its inverse, where $r_s(z_d)$ is the comoving sound horizon at the redshift of the baryon drag epoch and D_V is a spherically-averaged (two tangential and one radial) distance measure [10] given by

$$D_V(z) \equiv \left[(1+z)^2\, D_A^2(z) \frac{cz}{H(z)}\right]^{1/3}, \tag{3.4}$$

where $D_A(z) = r(z)/(1+z)$ is the angular diameter distance. We compute the sound

[3] http://wachowski.pha.jhu.edu/~dscolnic/PS1_public/

horizon via

$$r_s(z) = \int_0^t \frac{c_s}{a}\,\mathrm{d}t' = \int_0^a \frac{c_s}{a'^2 H(a')}\,\mathrm{d}a' \,, \tag{3.5}$$
$$c_s = \frac{c}{\sqrt{3\,(1+R)}} \,,$$

where the sound speed c_s depends on the ratio of baryon energy density to photon energy density, which is proportional to the scale factor:

$$R \equiv \frac{3\rho_b}{4\rho_\gamma} \approx 31500\,\Omega_b h^2 \left(\frac{T_{\rm CMB}}{2.7\ \mathrm{K}}\right)^{-4} a \,. \tag{3.6}$$

The redshift of the baryon drag epoch is given by the fitting formula [77]

$$z_d = \frac{1291\,(\Omega_m h^2)^{0.251}}{1 + 0.659\,(\Omega_m h^2)^{0.828}} \left[1 + b_1 (\Omega_b h^2)^{b_2}\right] \,, \tag{3.7}$$

where

$$b_1 = 0.313\,(\Omega_m h^2)^{-0.419} \left[1 + 0.607\,(\Omega_m h^2)^{0.674}\right] \,,$$
$$b_2 = 0.238\,(\Omega_m h^2)^{0.223} \,.$$

It is important to include a term for radiation in $H(a)$. One can write $\Omega_r = \Omega_m a_{\rm eq}$, where $a_{\rm eq} = 1/(1 + z_{\rm eq})$ is the scale factor at the epoch of matter-radiation equality and $z_{\rm eq}$ is approximated by

$$z_{\rm eq} \approx 25000\,\Omega_m h^2 \left(\frac{T_{\rm CMB}}{2.7\ \mathrm{K}}\right)^{-4} . \tag{3.8}$$

We assume the value $T_{\rm CMB} = 2.7255$ K in our analysis.

The measured values of the BAO parameters are summarized in Table 3.1. Covariance between different surveys should be negligible here, so we treat these as independent measurements.

Note that previous measurements of the BAO feature from SDSS LRG data (e.g. [10, 39]) cannot be used simultaneously with the measurement from [76] since roughly the same galaxy sample is analyzed. The measurement from [76] makes use of a reconstruction technique to enhance the BAO signal and increase the precision of the distance measurement. We use this measurement since it is the most precise and avoids the correlation between the pair of measurements from [39], where the SDSS LRG sample is combined with the SDSS main galaxy sample.

Also note that we choose to leave out the BAO measurements from the WiggleZ

Sample	z_{eff}	Parameter	Measurement
6dFGS	0.106	$r_s(z_d)/D_V(z_{\text{eff}})$	0.336 ± 0.015
SDSS LRG	0.35	$D_V(z_{\text{eff}})/r_s(z_d)$	8.88 ± 0.17
BOSS	0.57	$D_V(z_{\text{eff}})/r_s(z_d)$	13.67 ± 0.22

Table 3.1: Summary of BAO measurements combined in the analysis. We list the survey from which the measurement comes, the effective redshift of the survey, the observable parameter constrained, and its measured value.

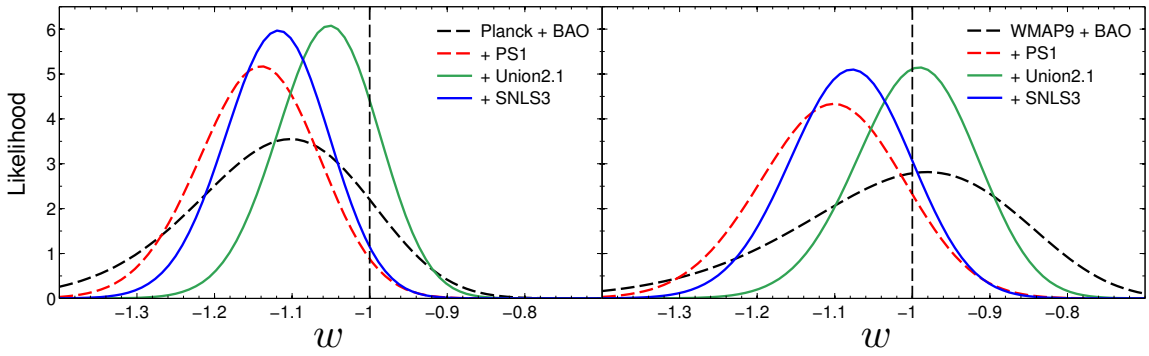

Figure 3.1: Likelihood curves for a constant equation of state w in a flat universe, using Planck CMB data (left panel) and WMAP9 CMB data (right panel). We compare constraints from CMB + BAO data alone (dashed black) to those which additionally include SN Ia data from SNLS3 (blue), Union2.1 (green), or PS1 (dashed red). All likelihoods are marginalized over other cosmological and nuisance parameters, as explained in the text.

Dark Energy Survey [41], which measures the BAO distance in three redshift slices ($z_{\text{eff}} = 0.44, 0.6, 0.73$). These measurements are somewhat correlated with the BOSS measurement due to overlap in sky area and redshift, and so far no correlation coefficients have been estimated. Although the correlation is probably negligible (in part due to shot noise), adding the WiggleZ measurements to the other BAO measurements improves our constraints only very slightly, so we leave them out.

3.2.3 CMB data

Although the CMB contains relatively little geometric information about dark energy, the position of the first peak in the power spectrum basically provides one very precise measurement of the angular diameter distance to recombination at $z \approx 1100$. This measurement helps break degeneracy between the dark energy equation of state and Ω_m [44]. In

our analysis, we include CMB constraints from Planck [7] and also from WMAP9 [78] for comparison.

We summarize CMB information using the following CMB observables:

$$l_a \equiv \pi \, (1 + z_*) \, \frac{D_A(z_*)}{r_s(z_*)} \, , \tag{3.9}$$

$$R \equiv \frac{\sqrt{\Omega_m H_0^2}}{c} \, (1 + z_*) \, D_A(z_*) \, . \tag{3.10}$$

The redshift z_* of decoupling is given by the fitting formula [79]

$$\begin{aligned} z_* = 1048 \, & \left[1 + 0.00124 \, (\Omega_b h^2)^{-0.738}\right] \\ & \times \left[1 + g_1 (\Omega_m h^2)^{g_2}\right] \, , \end{aligned} \tag{3.11}$$

where

$$g_1 = \frac{0.0783 \, (\Omega_b h^2)^{-0.238}}{1 + 39.5 \, (\Omega_b h^2)^{0.763}} \, ,$$

$$g_2 = \frac{0.560}{1 + 21.1 \, (\Omega_b h^2)^{1.81}} \, .$$

Following [80], we use the Markov chains from the Planck Legacy Archive (PLA) to derive constraints on the parameter combination $(l_a \, , R \, , z_*)$, which is known to efficiently summarize CMB information on dark energy, with the measurements themselves independent of the dark energy model to a good approximation. We assume the same model that we constrain in this analysis (flat universe, constant w) when deriving the CMB observables. For the Planck data, we use information from the temperature power spectrum combined with WMAP polarization at low multipoles (Planck + WP). We also use the PLA chains to derive the corresponding measurements for WMAP9 (temperature and polarization data) with the same model assumptions. The CMB measurements are summarized in Table 3.2.

We evaluate the correlation matrix for $(l_a \, , R \, , z_*)$ for Planck to be

$$\begin{pmatrix} 1.0000 & 0.5262 & 0.4708 \\ 0.5262 & 1.0000 & 0.8704 \\ 0.4708 & 0.8704 & 1.0000 \end{pmatrix} .$$

$\bar{x} \pm \sigma$	Planck	WMAP9
l_a	301.65 ± 0.18	301.98 ± 0.66
R	1.7499 ± 0.0088	1.7302 ± 0.0169
z_*	1090.41 ± 0.53	1089.09 ± 0.89

Table 3.2: Mean values and standard deviations of the CMB measurements used in our analysis. The measurements for both Planck and WMAP9 were obtained using the Markov chains provided by the Planck collaboration. We assumed the model with a flat universe and constant dark energy equation of state, the same model we constrain in this analysis.

The same correlation matrix for WMAP9 is

$$\begin{pmatrix} 1.0000 & 0.4077 & 0.5132 \\ 0.4077 & 1.0000 & 0.8580 \\ 0.5132 & 0.8580 & 1.0000 \end{pmatrix} .$$

We have explicitly verified that, when multiple probes are combined, the constraints on w obtained directly from the CMB chains are in good agreement with results obtained using the measurements in Table 3.2. For the base case of Planck combined with BAO and SNLS3 SNe, the best-fit values of w differ by less than 0.1σ. The discrepancy is greater when the complementary SN data are not included, but the difference is still less than 0.3σ for the data combinations we consider.

Note that our measurements cannot be directly compared to those presented in [80] because of different assumptions: we do not include Planck lensing information, we assume a flat model with w as a free parameter instead of a Λ model with curvature, and we treat z_* as an observable in place of $\Omega_b h^2$.

3.3 Results

3.3.1 Constraint methodology

The complete parameter set used in our analysis is

$$p_i \in \{\Omega_m\,, w\,, \Omega_m h^2\,, \Omega_b h^2\,, \{\mathcal{M}_i\}\}\ ,$$

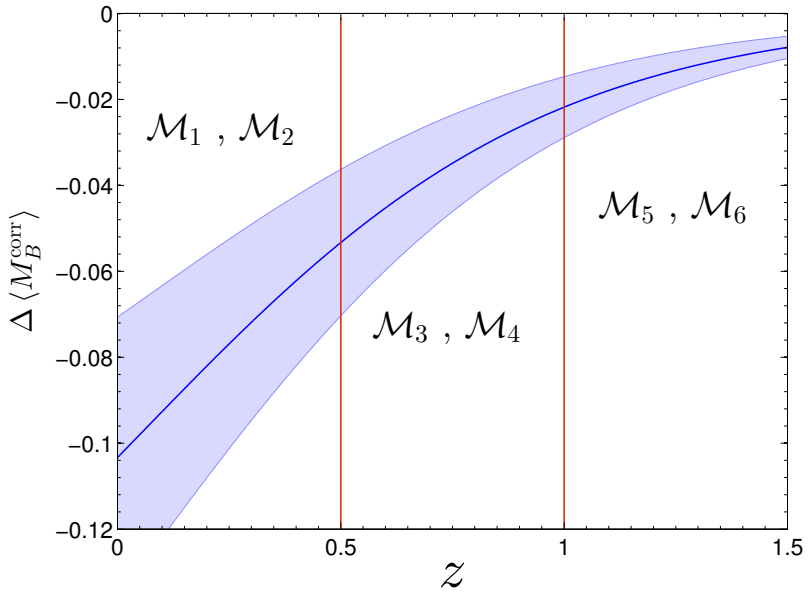

Figure 3.2: Evolution of the mass step predicted from a toy model calibrated using data from the Nearby Supernova Factory. This is similar to Fig. 11 of Rigault et al. (2013), though we include a region of uncertainty by propagating errors in the mass step and local star-forming fraction measured at $z = 0.05$ from the Nearby Supernova Factory data. Vertical lines separate the three redshift bins, each of which contains two $\mathcal{M}$ nuisance parameters, one for each host galaxy mass range.

where we marginalize over $\Omega_m h^2$ and $\Omega_b h^2$ for the CMB and BAO constraints and over one or more SN Ia nuisance parameters $\mathcal{M}_i$ (see Secs. 3.2.1.2 and 3.3.3). Given the small number of parameters, we calculate constraints using brute-force computation of likelihoods over a grid of parameter values. We assume a Gaussian likelihood $\mathcal{L} \propto \exp(-\chi^2/2)$, where we have ignored the $1/\sqrt{\det \mathbf{C}}$ prefactor, which is a constant and thus cancels out in likelihood ratios. Note that, in general, the SN covariance matrix is a function of the SN nuisance parameters. If we were to vary those parameters, we would need to recompute the SN covariance matrix at each step; however, one might still want to drop the Gaussian prefactor, as it can bias the values of recovered parameters if included (e.g. [38] and Appendix B of [17]). Finally, note that aside from the implicit prior that $\{\Omega_m\,, \Omega_m h^2\,, \Omega_b h^2\} \geq 0$, we assume flat priors on all of the parameters.

3.3.2 Basic constraints

Combined constraints on the equation of state, marginalized over the other parameters, are shown in Fig. 3.1, where the left panel shows the Planck data combined with the BAO and SN Ia data, while the right panel shows the same for WMAP9. CMB and BAO data

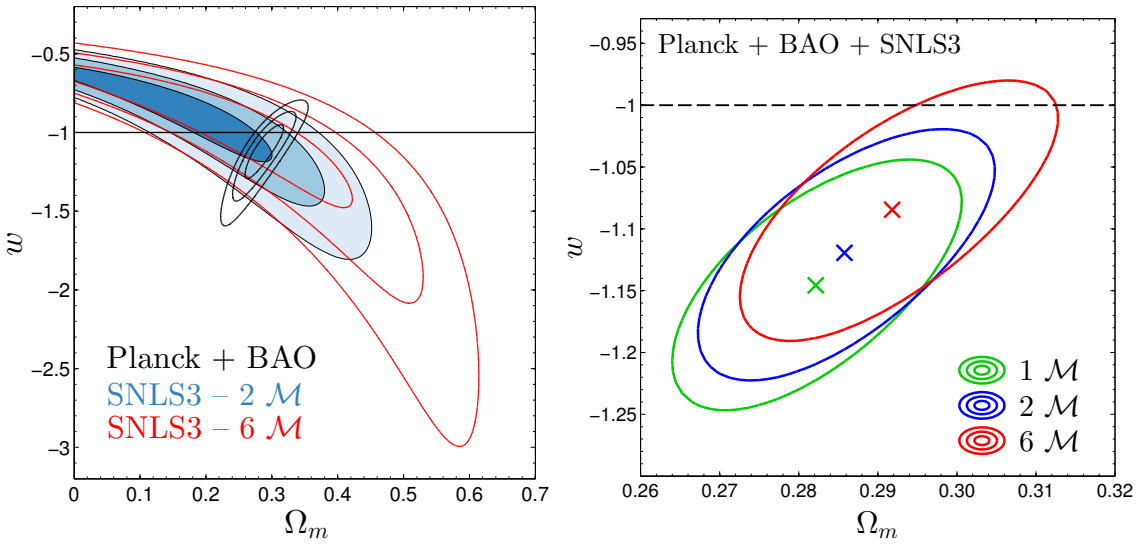

Figure 3.3: Effect of allowing for evolution of the mass step in redshift bins in the SN Ia analysis. *Left*: 68.3%, 95.4% and 99.7% likelihood contours in the Ω_m–w plane for SNLS3 data analyzed the standard way with two $\mathcal{M}$ nuisance parameters (filled blue) and a new way with six $\mathcal{M}$ parameters (open red), one for each of two mass bins and three redshift bins. Planck + BAO constraints (open black) are overlaid for comparison. *Right*: 68.3% contours in the same plane for combined Planck + BAO + SNLS3 data using one, two, or six $\mathcal{M}$ parameters.

alone constrain the equation of state rather weakly. With Planck, there is a preference for $w < -1$, but at $\simeq 1\sigma$ it is not significant. There is no preference at all with WMAP9. Note also that the constraints with Planck are visibly better than those with WMAP9, as Planck measures all of the CMB distance parameters $(l_a\,, R\,, z_*)$ more precisely, with errors that are 2–3 times smaller.

Things get more interesting when SN Ia data are added. The Union2.1 data set produces the best constraints when combined with CMB and BAO, marginally better than the constraints with SNLS3. Again, though, this leads to good agreement with a cosmological constant, with an insignificant preference for $w < -1$ driven by the Planck data. However, when SNLS3 or PS1 data are used, we find a preference for $w < -1$ at the 1.8σ (SNLS3) or 1.9σ (PS1) level with Planck and the 1σ (SNLS3) or 1.2σ (PS1) level with WMAP9.[4] Note that the PS1 data give slightly stronger evidence for $w < -1$, even though the overall constraints are weaker.

It is useful to study the SN Ia constraints in more detail, which we do in the following

[4]Since the posterior likelihoods are not perfectly Gaussian, we always determine σ values by computing the integral of the likelihood between the two values of w where the likelihood equals that at $w = -1$. The quoted multiple of σ is the number of standard deviations that enclose this probability in a *Gaussian* distribution.

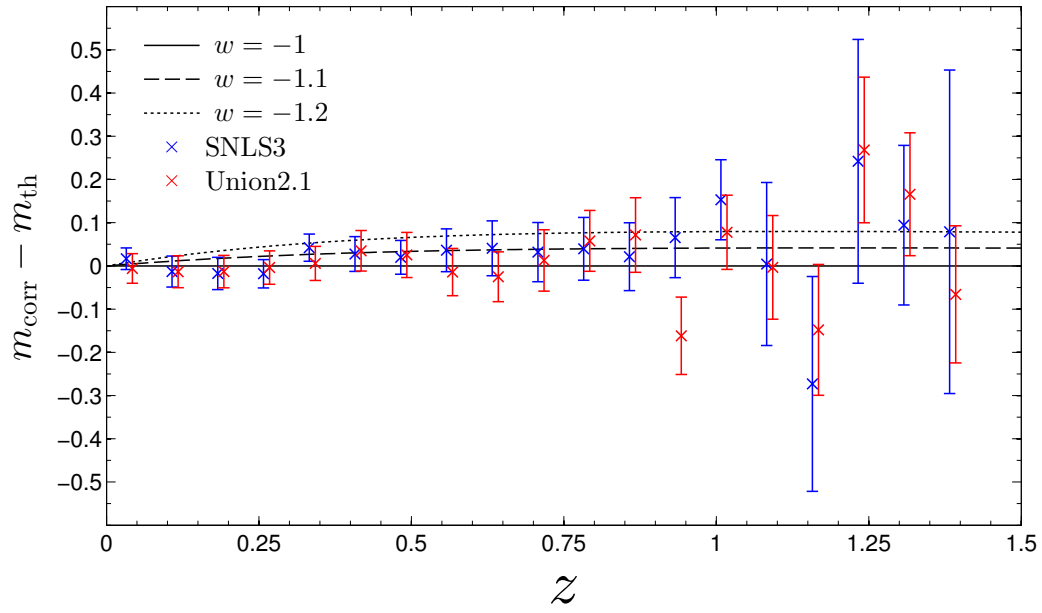

Figure 3.4: Residuals of SN Ia magnitudes, binned by redshift (inverse-covariance weights), for SNLS3 (blue) and Union2.1 (red). All curves and data points are relative to a flat ΛCDM cosmology with $\Omega_m = 0.3$, which is roughly the best-fit value from CMB and BAO data. The plot shows the degree to which SNe in each redshift range pull toward $w < -1$, and we show several theory curves with constant w for comparison.

two subsections. Our work here complements the detailed systematic analyses in [1, 17, 71, 81–87]. The particular focus of this paper is the effect of potential SN Ia systematics and external priors on evidence for "phantom" behavior of dark energy where $w < -1$.

3.3.3 SN Ia host mass correction

Recently, much work has been focused on understanding the environmental dependence of SNe Ia, which presumably is not only one of the important factors contributing to intrinsic scatter of SN magnitudes but also an important systematic effect. In particular, there is evidence that the absolute magnitude of SNe Ia is correlated with host galaxy properties such as specific star formation rate, metallicity, and stellar mass *after* the usual light-curve stretch and color correction [71, 81, 82, 84, 85, 87]. Most striking is the evidence for a "mass step" where SNe in more massive hosts ($\gtrsim 10^{10} M_\odot$) are brighter, on average, after light-curve correction. This is consistent with a step function, suggesting that one could fit for two separate magnitude offsets (i.e. $\mathcal{M}$), one for SNe in low-mass hosts and one for SNe in high-mass hosts. Indeed this was prescribed for SNLS3 in [17].

Of course, the mass of the host galaxy itself should have no direct physical influence on SN luminosity, so something else must be at work. Recent measurements from Nearby

Supernova Factory data [87] have indicated strong ($\sim 3.1\sigma$) evidence that SNe Ia in *locally* passive environments are brighter on average than those in active star-forming environments. The authors further show that this can explain the observed mass step, as passive environments are more common in high-mass galaxies. This is especially important because the fraction of SNe Ia in locally star-forming environments surely evolves with redshift, and therefore the amplitude of the mass step should also evolve. This is a systematic effect not corrected for by the introduction of two $\mathcal{M}$ parameters, and the authors estimate a bias on the equation of state of $\Delta w \simeq 0.06$.

Fig. 3.2 shows a toy model for the redshift evolution of the mass step from the analysis of [87], with errors that we have estimated by propagating errors in the mass step and local star-forming fraction measured at $z = 0.05$ from the Nearby Supernova Factory data. Given the astrophysical uncertainties in linking the star formation rate to host stellar mass and the latter to absolute magnitude of SNe Ia, we do not try to use any fixed model to correct for this. Instead, we use a less model-dependent parametrization of the relation between the observed host galaxy mass and absolute magnitude by allowing for two independent values of $\mathcal{M}$ in each of three redshift bins: $z \leq 0.5$, $0.5 < z \leq 1.0$, and $z > 1.0$. Therefore, instead of two offset parameters in the Hubble diagram as in [17], we now have a total of six $\mathcal{M}$ parameters. The redshift extent that pairs of these parameters cover is illustrated in Fig. 3.2, with the divisions centered on the fiducial model presented in [87]. Clearly, once their amplitudes are allowed to float, these nuisance parameters will do a much better job recovering the redshift dependence of the mass step than a single pair of $\mathcal{M}$ parameters for the whole redshift range. We succeeded in marginalizing analytically over these six parameters with flat priors and including covariance between SNe with different $\mathcal{M}$ (see Sec. A).

The result is shown in Fig. 3.3. In the left panel, the filled blue contours show the 68.3%, 95.4% and 99.7% constraints for the usual case with two $\mathcal{M}$ parameters, while the open red contours show the result for the six $\mathcal{M}$ parameters. The constraints clearly weaken, although not as much as one might expect with four extra parameters introduced at the level of the Hubble diagram. This "self-calibration" serves to effectively protect against departures from the standard-candle assumption. Remarkably, when SN Ia data is combined with CMB and BAO data, the resulting constraints are barely weakened because the lengthening of the contours occurs mainly in the direction that is very well constrained by the complementary data sets. On the other hand, the right panel of Fig. 3.3 shows that the best-fit value of w is shifted appreciably, illustrating the sensitivity of dark energy constraints to systematic effects in SN Ia measurements.

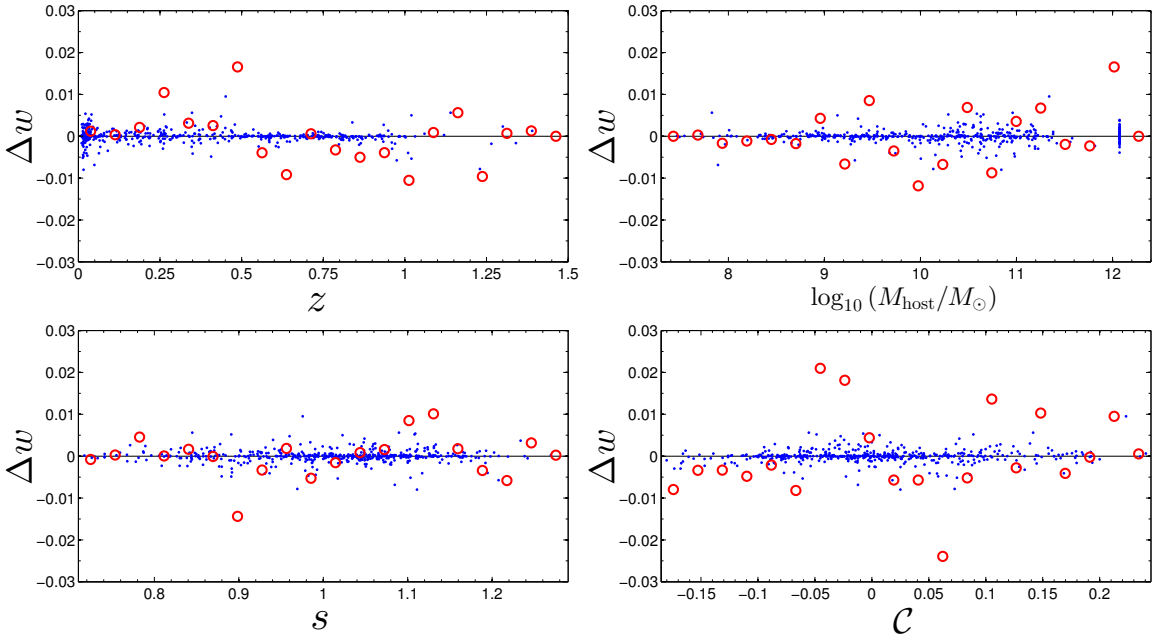

Figure 3.5: Effect of each individual SNLS3 SN on the combined constraint on the equation of state, as a function of redshift (top left), host galaxy stellar mass (top right), stretch (bottom left), and color (bottom right). The blue points show the shift Δw in the final constraint on w due to each individual SN. The red circles show the combined (summed) pull from each bin in the particular quantity.

3.3.4 Scanning through SN observables

Are SNe in any given redshift range of the SNLS3 compilation responsible for shifting the equation of state to phantom values? We examine this issue in Fig. 3.4, where we show the residuals in the Hubble diagram relative to $w = -1$ for SNe binned in $\Delta z = 0.075$ bins. In this analysis, we have assumed the same cosmology for both SNLS3 and Union2.1 ($\Omega_m = 0.3$, $w = -1$), where Ω_m is roughly the best-fit value from CMB + BAO. We fix the stretch, color, and $\mathcal{M}$ parameters at their best-fit values separately for each SN Ia data set. We see that the two data sets are consistent at the 1σ level in all bins except at $z \simeq 0.95$, where they are consistent at 2σ. Therefore, the agreement between the two Hubble diagrams seems excellent.

We can get an even more accurate picture of the redshift dependence of SN constraints on the equation of state. The individual points in Fig. 3.5 show the effect of adding a single SN to the combination of Planck + BAO + SNLS3. For practical purposes,[5] we compare the mean equation of state rather than the maximum of the likelihood. The red circles denote

[5]The computed mean value depends on the precise likelihood ratios between different points in a grid of parameter values, but a simple numerical estimate of the maximum-likelihood value will only reflect changes that are of order the grid spacing or larger.

the total (summed) contribution of SNe per $\Delta z = 0.075$ bin. We see that no redshift bin contributes to a negative shift in the mean equation of state more than about 0.01.

The other three panels in Fig. 3.5 show the individual SNLS3 SN contributions to w as a function of stretch, color, and host galaxy stellar mass. As before, the red circles denote the summed contribution of all SNe in a given bin in the quantity shown. As in the redshift scan, we do not observe any correlation or particular region in the stretch, color, or host-mass spaces that is chiefly responsible for shifting the equation of state.

3.3.5 External H_0 Prior

Adding a prior corresponding to an external measurement of the Hubble constant with a small error bar has an important effect on our results. This is easy to understand: Given that the CMB essentially pins down the physical matter density $\Omega_m h^2$ (for example, to better than 2% with Planck), $\delta \ln \Omega_m \simeq -2\delta \ln h$ and therefore a higher value of H_0 corresponds to a lower value of Ω_m. For a lower Ω_m, the degenerate direction of CMB + BAO constraints leads to a more negative w. Therefore, we would expect that higher values of H_0 lead to more negative w, and vice versa.

This expectation is confirmed by our explicit tests with the current data, shown in Fig. 3.6. Here we use the same Hubble constant measurement error of ± 2.4 km/s/Mpc as reported by [88], but instead of adopting the central value of 73.8 km/s/Mpc, we vary the central value as an integer in the range $H_0 \in [65, 75]$ km/s/Mpc, one value at a time. We show the final constraint on the dark energy equation of state using the CMB + BAO + H_0 data, with or without the addition of the PS1 or SNLS3 SN data, as a function of the H_0 central value. For the external prior $H_0 = 74 \pm 2.4$ km/s/Mpc, we recover results similar to [70] that favor $w < -1$ at $\sim 2.5\sigma$. However, for a smaller central value of H_0 (≤ 70 km/s/Mpc), the results are consistent with $w = -1$ at the 2σ level or less, and for an even smaller central value ($\simeq 66$ km/s/Mpc), we find the results consistent with $w = -1$ at 1σ.

3.4 Conclusions

We studied geometric constraints on the dark energy equation of state from recent SN Ia data complemented with distance measurements from the CMB and a compilation of BAO results. For the SNLS3 and PS1 SN data sets, the combined SN Ia + BAO + Planck data favor a phantom equation of state where $w < -1$ at $\sim 1.9\sigma$ confidence (see Fig. 3.1), in good agreement with the corresponding results reported in the original SN Ia and Planck

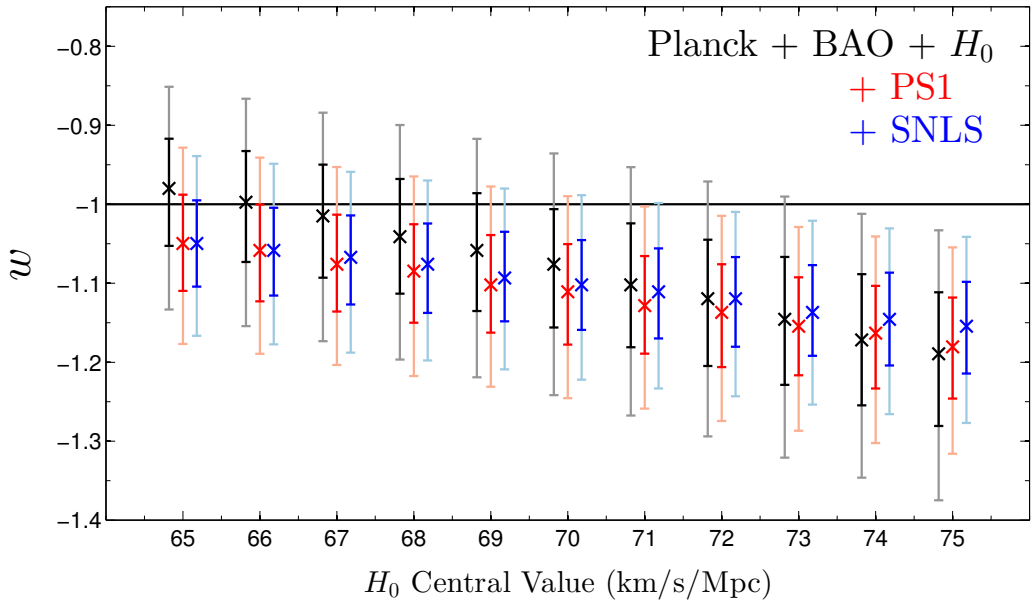

Figure 3.6: Effect of an external H_0 prior on the constant equation of state. We show the effect on Planck + BAO constraints (black) and on combined Planck + BAO + SN constraints separately for PS1 (red) and SNLS3 (blue), where the error bars bound 68.3% and 95.4% of the likelihood for w. The external prior has an uncertainty of 2.4 km/s/Mpc in each case, mimicking the uncertainty in the Riess et al. (2011) measurement.

papers. Evidence for a phantom equation of state is weaker if WMAP9 is used instead of Planck, while the Union2.1 data set is consistent with the cosmological-constant value $w = -1$ when combined with either CMB data set.

We have tested for a possible presence of systematics correlated with SN properties – their redshifts, stretch factors, colors, and host galaxy masses. We find no evidence of a trend or that a particular range of any of these properties contributes to pushing $w < -1$; rather, the hints of a phantom equation of state appear to be uncorrelated with these basic SN observables. We have also investigated the effect of modeling the redshift dependence of the host galaxy mass step of SN luminosities, assigning up to six separate $\mathcal{M}$ parameters for different mass and redshift bins. The additional nuisance parameters shift the SN Ia constraints sufficiently that, when combined with BAO and CMB data, they allow agreement with $w = -1$ at $\sim 1\sigma$. Therefore, a more generous allowance for the temporal evolution of the dependence of SN luminosity on host galaxy mass removes the evidence for $w < -1$. The hope for the future is that independent observations can pin down the environmental dependence of SN luminosities and make it possible to account for such subtle but important systematic effects in a consistent way and without the damaging effect of extra nuisance parameters at the level of the Hubble diagram.

External measurements of the Hubble constant play a particularly important role in the final constraints on w. This is shown in Fig. 3.6, where we illustrate the effect of adding a measurement of H_0 with an error of 2.4 km/s/Mpc as in [88], but with the central value varied from 65-75 km/s/Mpc. Clearly, interesting $> 2\sigma$ evidence for the phantom equation of state is present only when the central value is somewhat large: $H_0 \gtrsim 71$ km/s/Mpc. Therefore, as first clearly argued by [89], with excellent CMB constraints the Hubble constant measurements and their interpretation (e.g. [90, 91]) are among the most important inputs in determining the dark energy equation of state.

Although we have taken Planck + BAO data at face value throughout most of our analysis, it is worth mentioning that systematics may be present in these data as well. This is particularly true for the Planck data, given that its analysis is still in the early stages and given the moderate tension between Planck results and both WMAP and growth measurements (e.g. [92]). Indeed, a recent re-analysis of Planck data [93] resulted in parameter shifts that somewhat reduce the tension with WMAP, and substantial ongoing work is focused on understanding systematics in growth measurements.

With current data we therefore find ourselves in an interesting situation in which we can make the following statement at 2σ confidence: Given Planck data, either the SNLS3 and PS1 data have systematics that remain unaccounted for or the Hubble constant is below 71 km/s/Mpc; else the dark energy equation of state is indeed phantom.

CHAPTER 4

Multiplicative Errors in the Power Spectrum

4.1 Introduction

Observations of large-scale structure (LSS) have proven to be a powerful probe of cosmology in recent years. Earlier large galaxy surveys, such as CfA [94], APM [95], and 2dF [96, 97], have paved the way for modern surveys like WiggleZ [98], SDSS [99–101], and the Baryon Oscillation Spectroscopic Survey (BOSS), the current incarnation of SDSS [102, 103]. These surveys have identified millions of galaxies and obtained spectra (and therefore redshifts) of over one million, allowing us to map the three-dimensional distribution of matter in the Universe. The enormous data sets resulting from these surveys are often distilled into measurements of the location of the peak in the correlation function corresponding to the scale of baryon acoustic oscillations (BAO), the imprint on structure resulting from sound waves propagating in the early Universe [10, 39, 43, 76, 104]. These BAO measurements, some of which are now at the percent level [13], have been crucial in that they complement other probes of cosmic expansion to help break degeneracies between key cosmological parameters.

But there is much more information in the power spectrum than just the primary BAO peak, and with ongoing surveys like the Dark Energy Survey (DES; Abbott *et al.* 105), which is on track to identify $\sim$300 million galaxies, the galaxy power spectrum as a whole will complement other probes of cosmology (CMB power spectra, Type Ia supernovae, weak lensing, etc.) to place tight constraints on dark energy and other cosmological parameters. Planning is already underway for future wide-field LSS surveys, such as LSST [106] and *Euclid* [107].

Making these observations suitable for cosmology is not trivial. With the enormous statistical power of surveys like DES, control of systematics becomes crucial, especially at small scales where cosmic variance is small. A major class of systematic errors is *photometric calibration* errors, by which we mean any systematic that effectively causes the

magnitude limit of the sample to vary across the sky, thus biasing the true galaxy power spectrum. A number of recent observations [108–114] show a significant excess of power at large scales that likely results from such calibration errors that have not been accounted for. Recent work [109, 110, 114–117] has focused on mitigating these systematics in order to probe the underlying cosmology.

[118], which we will refer to as H13, introduced a formalism for quantifying the effect of an arbitrary photometric calibration error. They found that in order to use information from large scales to constrain cosmological parameters, the root-mean-square variation due to the calibration field must be $\sim$0.001–0.01 mag or less in order to avoid significantly biasing cosmological parameters. This is a very stringent requirement.

A potentially more dangerous effect is the *multiplicative* leakage of these large-angle errors to small angular scales, where most cosmological information resides. As discussed in H13, the observed number density of galaxies is given by $N_{\rm obs}(\hat{\boldsymbol{n}}) = [1 + c(\hat{\boldsymbol{n}})]\, N(\hat{\boldsymbol{n}})$, where the true number density $N(\hat{\boldsymbol{n}})$ is modulated by a calibration-error field $c(\hat{\boldsymbol{n}})$, which is directly related to a host of interrelated photometric effects (survey depth, completeness, atmospheric conditions, galactic dust, etc.). Even though the calibration error is significant only at large angular scales, it multiplies the true galaxy field, so the observed field is affected on *all* angular scales. This multiplicative effect, to our knowledge first pointed out in H13 in the context of LSS systematics, is further studied in this work.

Current methods to clean the power spectra have been impressively efficient, but they typically rely on systematics templates – prior knowledge of the relative spatial variation of the contamination across the sky due to a known systematic. The methods rely on the assumption that these templates are correct and that the set of templates is complete; any *unknown* large-scale systematic that is not covered by one of the templates (or some combination thereof) will not be accounted for.

Mode projection (or extended mode projection, see Leistedt and Peiris 117) is a particularly effective method. Essentially, it is a way of marginalizing over spatially varying patterns on the sky that are expected to be caused by various systematics. While mode projection has been shown to be effective at mitigating the added power from known systematics, this method cannot remove multiplicative errors. To understand why, suppose for simplicity that a single systematic effect modulates the observed galaxy densities and that the shape of the template is that of a pure spherical harmonic (so that $c(\hat{\boldsymbol{n}}) \propto Y_{\ell m}(\hat{\boldsymbol{n}})$ for some ℓ, m). This modulation will then not only add power at the angular scale ℓ, but it will also affect the power at *all* other multipoles. The obvious way to "project out" this mode, at least in principle, is to simply ignore that one contaminated m mode when estimating the variance C_ℓ. The additive error is removed entirely with little loss of cosmological informa-

tion, but other multipoles have still been affected by the multiplicative effect in accordance with our Eq. (4.13) below.

In this paper, we study a new approach that is both alternative and complementary to previously employed techniques: using some of the power spectrum observations themselves to directly measure the systematic contamination and correct the rest of the measurements for a cosmological analysis. Since the calibration errors are expected to enter at large scales and then fall off quickly at higher multipoles (smaller scales), one may interpret the low-multipole power spectrum as measurements of the systematics and use these to correct the power spectrum at high multipoles, sacrificing some cosmological information from large scales to remove the multiplicative error and obtain unbiased estimates of cosmological parameters from small scales. The benefit of this approach is that no templates or otherwise detailed modelling of the systematics is required at this level.

The rest of the paper is organized as follows. In Sec. 4.2, we review and extend the calibration formalism introduced in H13, discuss our Fisher matrix formalism, and describe a fiducial model and DES-like survey. In Sec. 4.3, we quantify the effect of multiplicative calibration error for our fiducial survey and demonstrate the self-calibration method. In Sec. 4.4, we summarize our conclusions and discuss how one might apply the self-calibration method to real data.

4.2 Methodology

In this section, we outline our formalism to describe the calibration errors, review and extend the Fisher matrix for the galaxy power spectrum, and detail our fiducial model and survey.

4.2.1 Calibration Error Formalism

In the absence of all systematics, we would observe the true number density of galaxies on the sky, which we expand in spherical harmonics:

$$\delta(\hat{\boldsymbol{n}}) \equiv \frac{N(\hat{\boldsymbol{n}}) - \bar{N}}{\bar{N}} = \sum_{\ell=0}^{\infty} \sum_{m=-\ell}^{\ell} a_{\ell m} Y_{\ell m}(\hat{\boldsymbol{n}}) \,, \tag{4.1}$$

where a bar denotes a sky average and where the monopole vanishes ($a_{00} = 0$) since it is proportional to the average overdensity on the sky, which is zero by construction. The coefficients $a_{\ell m}$ are expected to be Gaussian random variables with a mean of zero and a variance that depends on the cosmological model. The various m modes are statistically

independent under the assumption of isotropy, so we have the familiar relations

$$\langle a_{\ell m} a^*_{\ell' m'} \rangle = \delta_{\ell\ell'}\, \delta_{mm'}\, C_\ell \ , \tag{4.2}$$

$$\langle a_{\ell m} \rangle = 0 \ . \tag{4.3}$$

Following H13, we now consider the effect of an arbitrary variation in the limiting magnitude $\delta m_{\rm max}(\hat{\boldsymbol{n}})$ of the photometric survey due to calibration variation across the sky. This magnitude variation implies a *relative* variation in galaxy counts $[\delta N/N](\hat{\boldsymbol{n}}) \propto \delta m_{\rm max}(\hat{\boldsymbol{n}})$, where the constant of proportionality depends on the faint-end slope of the luminosity function $s(z) \equiv d\log_{10} N(z,m)/dm|_{m_{\rm max}}$ that may depend on redshift but does not depend on direction. More generally, one can write $[\delta N/N](\hat{\boldsymbol{n}}) \equiv c(\hat{\boldsymbol{n}})$ so that the observed galaxy number density $N_{\rm obs}(\hat{\boldsymbol{n}})$ is equal to the true number density $N(\hat{\boldsymbol{n}})$ modulated by the field $c(\hat{\boldsymbol{n}})$, which we can also expand in spherical harmonics:

$$N_{\rm obs}(\hat{\boldsymbol{n}}) = [1 + c(\hat{\boldsymbol{n}})]\, N(\hat{\boldsymbol{n}}) \ , \tag{4.4}$$

$$c(\hat{\boldsymbol{n}}) = \sum_{\ell m} c_{\ell m} Y_{\ell m}(\hat{\boldsymbol{n}}) \ . \tag{4.5}$$

The calibration coefficients $c_{\ell m}$ are deterministic (not inherently stochastic) and thus have the trivial statistical properties

$$\langle c_{\ell m} c^*_{\ell' m'} \rangle = c_{\ell m} c^*_{\ell' m'} \ , \tag{4.6}$$

$$\langle c_{\ell m} \rangle = c_{\ell m} \ . \tag{4.7}$$

In other words, the calibration-error field is a fixed pattern on the sky, and there is no loss of generality in making this assumption to simplify the analysis. The observed overdensity is given by

$$\begin{aligned} \delta_{\rm obs}(\hat{\boldsymbol{n}}) &\equiv \frac{N_{\rm obs}(\hat{\boldsymbol{n}}) - \bar{N}_{\rm obs}}{\bar{N}_{\rm obs}} = \frac{[1 + c(\hat{\boldsymbol{n}})]\, N(\hat{\boldsymbol{n}})}{\bar{N}(1+\epsilon)} - 1 \\ &= \frac{1}{1+\epsilon} \left[\delta(\hat{\boldsymbol{n}}) + c(\hat{\boldsymbol{n}}) + c(\hat{\boldsymbol{n}})\delta(\hat{\boldsymbol{n}}) - \epsilon\right] \ , \end{aligned} \tag{4.8}$$

where $\bar{N}_{\rm obs} = \bar{N}(1+\epsilon)$ is the observed mean number of galaxies per pixel on the sky. Then ϵ is defined by

$$\epsilon \equiv \frac{1}{\bar{N}}\, \overline{c(\hat{\boldsymbol{n}}) N(\hat{\boldsymbol{n}})} = \overline{c(\hat{\boldsymbol{n}})\, [1 + \delta(\hat{\boldsymbol{n}})]} = \frac{c_{00}}{\sqrt{4\pi}} + \frac{1}{4\pi} \sum_{\ell m} c_{\ell m} a^*_{\ell m} \ , \tag{4.9}$$

where the overbar again denotes a sky average.

Expanding the observed overdensity in spherical harmonics,

$$\delta_{\rm obs}(\hat{\boldsymbol{n}}) = \sum_{\ell m} t_{\ell m} Y_{\ell m}(\hat{\boldsymbol{n}}) \,, \tag{4.10}$$

we calculate the expansion coefficients of $\delta_{\rm obs}$ to be

$$t_{\ell m} = \frac{1}{1+\epsilon}\left[a_{\ell m} + c_{\ell m} - \sqrt{4\pi}\,\epsilon\,\delta_{\ell 0} + \sum_{\substack{\ell_1 m_1 \\ \ell_2 m_2}} R^{\ell_1\,\ell_2\,\ell}_{m_1 m_2 m}\, c_{\ell_1 m_1} a_{\ell_2 m_2}\right] \,, \tag{4.11}$$

where the coupling coefficient $R^{\ell_1\,\ell_2\,\ell}_{m_1 m_2 m}$ is a variant of the Gaunt coefficient, the result of integrating a product of three spherical harmonics. It can be written in terms of Wigner 3-j symbols:

$$\begin{aligned} R^{\ell_1\,\ell_2\,\ell}_{m_1 m_2 m} \equiv (-1)^m \sqrt{\frac{(2\ell_1+1)(2\ell_2+1)(2\ell+1)}{4\pi}} \\ \times \begin{pmatrix} \ell_1 & \ell_2 & \ell \\ 0 & 0 & 0 \end{pmatrix} \begin{pmatrix} \ell_1 & \ell_2 & \ell \\ m_1 & m_2 & -m \end{pmatrix} \,. \end{aligned} \tag{4.12}$$

In this formalism, how will the observed power be related to the true power C_ℓ? If the observed coefficients are $t_{\ell m}$, then the observed (potentially biased) power is given by (Appendix B)

$$\begin{aligned} T_\ell &= \frac{\sum_m \langle |t_{\ell m}|^2 \rangle}{2\ell+1} \\ &= C_\ell + C_\ell^{\rm cal} - \frac{1}{2\pi} C_\ell^{\rm cal} C_\ell \\ &\quad + \frac{1}{4\pi} \sum_{\ell_1 \ell_2} (2\ell_1+1)\, C_{\ell_1}^{\rm cal} \begin{pmatrix} \ell_1 & \ell_2 & \ell \\ 0 & 0 & 0 \end{pmatrix}^2 (2\ell_2+1)\, C_{\ell_2} \,, \end{aligned} \tag{4.13}$$

where we have defined the calibration-error contribution to the observed power as

$$C_\ell^{\rm cal} \equiv \sum_m |c_{\ell m}|^2/(2\ell+1) \,. \tag{4.14}$$

It is worth making several comments about Eq. (4.13), where the observed angular power spectrum T_ℓ is given as a function of the true power C_ℓ, the calibration-error power $C_\ell^{\rm cal}$, and various geometric coupling factors. The second term on the right-hand side, $C_\ell^{\rm cal}$, represents the *additive* effect of calibration error, which is typically important at large angular scales

(such as $\ell \lesssim 20$). The other terms are products of the true and calibration-error power; they represent the *multiplicative* effect of calibration errors that affects the observed power T_ℓ at all angular scales. Note that Eq. (4.13) is equivalent to the formula for T_ℓ from H13, though here we have substantially simplified it by defining away the $1/(1+\epsilon)$ factor and using Wigner 3-j relations (see Appendix B for more details).

Finally, we can gain some insight into the multiplicative contribution to T_ℓ by simplifying Eq. (4.13) under the assumption that $C_\ell^{\rm cal}$ vanishes for multipoles greater than some cutoff multipole $\ell = \ell_{\rm max,\,cal}$ and with the approximation that the true power C_ℓ is constant in the multipole range $\ell \pm \ell_{\rm max,\,cal}$ that contributes to the sum over ℓ_2. This allows us to factor C_{ℓ_2} out of the sum and apply the Wigner 3-j relation Eq. (B.8). Then Eq. (4.13) simply becomes

$$T_\ell \simeq C_\ell + C_\ell^{\rm cal} - \frac{1}{2\pi} C_\ell^{\rm cal} C_\ell + \sigma_c^2\, C_\ell \,, \tag{4.15}$$

where $\sigma_c^2 \equiv {\rm Var}[c(\hat{\boldsymbol{n}})] = \sum_{\ell=1}^{\infty}(2\ell+1)C_\ell^{\rm cal}/(4\pi)$ is the variance of the calibration field across the sky. This is generally an excellent approximation, and it shows that the multiplicative effect (the last term) is roughly independent of the shape of the calibration power spectrum. Also, all C_ℓ at $\ell > \ell_{\rm max,\,cal}$ are multiplied by roughly the same factor, an effect mimicking that of an incorrect galaxy bias.

4.2.2 Fisher matrix and bias

We now review and extend the standard LSS Fisher matrix formalism in order to forecast both the extent to which multiplicative calibration errors bias cosmological parameters and the uncertainty that results from trying to measure the contamination itself.

In the absence of systematics, and when cross-power spectra are assumed to vanish ($C_\ell^{\rm ij} \equiv 0$ for $i \neq j$), the observables C_ℓ^{ii} are uncorrelated with a variance due to cosmic sampling variance and shot noise:

$${\rm Var}[C_\ell^{ii}] = \frac{2}{(2\ell+1) f_{\rm sky}} \left(C_\ell^{ii} + \frac{1}{N^i} \right)^2 , \tag{4.16}$$

where N^i is the number of galaxies per steradian for redshift bin i. Then the well-known Fisher matrix for measurements of the power spectrum is given by

$$F_{\alpha\beta} = \sum_i \sum_\ell \frac{\partial C_\ell^{ii}}{\partial p_\alpha} \frac{1}{{\rm Var}[C_\ell^{ii}]} \frac{\partial C_\ell^{ii}}{\partial p_\beta} \,, \tag{4.17}$$

where the p_i are cosmological parameters.

We will be particularly interested in the effect of the presence of uncorrected-for calibration errors on cosmological parameters. A useful Fisher-matrix-based formalism is available to evaluate these effects [119, 120]. Given a bias $\delta\mathbf{m}$ in a vector of observables $\mathbf{m}$ with covariance matrix $\mathbf{C}$, the linear estimate for the bias in cosmological parameters is

$$\delta\mathbf{p} = \mathbf{F}^{-1}\mathbf{D}\,\mathbf{C}^{-1}\delta\mathbf{m}\,, \tag{4.18}$$

where the matrix $\mathbf{D}$ contains the derivatives of the observables with respect to the parameters evaluated at their fiducial values: $D_{ij} = \partial m_j/\partial p_i$.

We can extend the Fisher matrix to measure both cosmological parameters and calibration-error parameters $C_\ell^{\rm cal}$ from the observed (biased) angular power spectrum. Our observables are now the set of T_ℓ^{ii}, and we calculate their covariance from Eq. (4.15). To a good approximation, they are uncorrelated with a variance

$$\mathrm{Var}[T_\ell] \simeq \mathrm{Var}[C_\ell]\left(1+\sigma_c^2-\frac{1}{2\pi}C_\ell^{\rm cal}\right)^2, \tag{4.19}$$

where $\mathrm{Var}[C_\ell]$ is the usual error from cosmic variance plus shot noise, as in Eq. (4.16), and the redshift bin indices have been suppressed. The derivatives with respect to the parameters are

$$\frac{\partial T_\ell}{\partial p_i} \simeq \frac{\partial C_\ell}{\partial p_i}\left(1+\sigma_c^2-\frac{1}{2\pi}C_\ell^{\rm cal}\right)\,, \tag{4.20}$$

$$\frac{\partial T_\ell}{\partial C_{\ell'}^{\rm cal}} \simeq \delta_{\ell\ell'}\left(1-\frac{1}{2\pi}C_\ell\right)+\frac{2\ell'+1}{4\pi}\,C_\ell\,. \tag{4.21}$$

Note that when none of the $C_\ell^{\rm cal}$ are added as parameters, the Fisher matrix for cosmological parameters reduces to the usual Fisher matrix Eq. (4.17), independent of the fiducial size of the calibration errors.

4.2.3 Fiducial model and survey

At small scales, we use the Limber approximation, which ignores the contribution of radial modes, and model the angular power spectra of galaxy density fluctuations as

$$C_\ell^{ij} = b^i b^j \int_0^\infty \frac{H(z)}{r^2(z)}\,P\left(\frac{\ell+\frac{1}{2}}{r(z)},z\right)\,W^i(z)\,W^j(z)\,dz\,, \tag{4.22}$$

where b^i is the galaxy bias for the $i^{\rm th}$ redshift bin (which we assume to be a constant), $H(z)$ is the Hubble parameter, $r(z)$ is the comoving distance, $P(k,z)$ is the power spectrum, and

the weights are given by

$$W^i(z) = \frac{n(z)}{N^i}\left[\theta\left(z - z^i_{\rm min}\right) - \theta\left(z - z^i_{\rm max}\right)\right], \tag{4.23}$$

where $\theta(x)$ is the Heaviside step function, $z^i_{\rm min}$ and $z^i_{\rm max}$ are the lower and upper bound of the $i^{\rm th}$ redshift bin, and $n(z)$ is the radial distribution of galaxies per steradian. We use the transfer functions and nonlinear modelling of CAMB [121] to compute and evolve the power spectrum.

The Limber approximation is not valid at the largest scales, so for $\ell \leq 30$, we use the full expression for the power spectrum:

$$C^{ij}_\ell = \frac{2}{\pi}\int_0^\infty P(k,0)\, I^i_\ell(k)\, I^j_\ell(k)\, k^2 dk\,, \tag{4.24}$$

$$I^i_\ell(k) \equiv b^i \int_0^\infty W^i(z)\, D(z)\, j_\ell(k\, r(z))\, dz\,, \tag{4.25}$$

where $D(z)$ is the linear growth factor relative to $z = 0$ (since we are safely in the linear regime) and $j_\ell(x)$ is the spherical Bessel function of order ℓ. Note that in the above we are assuming a flat universe.

Our fiducial DES-like survey covers 5,000 deg^2 (corresponding to $f_{\rm sky} \simeq 0.12$) and identifies a total of 300 million galaxies ($\simeq$17 galaxies per arcmin^2). We split the sample into five tomographic redshift bins of width $\Delta z = 0.2$, centred at $z = 0.1,\ 0.3,\ 0.5,\ 0.7,$ and 0.9. We take the radial distribution of galaxies to be $n(z) \propto z^2 \exp(-z/z_0)$, with $z_0 = 0.3$, and divide the total number of galaxies among the redshift bins accordingly. As shown in Fig. 4.1, the distribution peaks at $z = 2z_0 = 0.6$. We assume that the photometric redshifts can be determined well enough that the cross-power spectra between these bins are small enough to be ignored, making the power spectra for different z slices statistically independent.

We choose for our fiducial cosmology a flat ΛCDM model with $\Omega_m = 0.3$, $\Omega_m h^2 = 0.143$, $\Omega_b h^2 = 0.0222$, $n_s = 0.96$, and $10^9 A_s = 2.2$ for $k_0 = 0.05$ Mpc^{-1}, values which agree well with data from *Planck* [7] and other probes.

In our analysis, we allow the dark energy equation of state to vary along with the parameters above, though we keep $\Omega_m h^2$ and $\Omega_b h^2$ fixed at their fiducial values. In practice, Planck CMB measurements constrain these parameters very well (to $\sim$1%), so we are effectively adding Planck priors to all of our constraints and assuming the remaining uncertainty to be negligible, which should be a reasonable approximation. We assume a (constant) galaxy bias $b^i = 2.2$ (same for all redshift bins), which we hold fixed for simplic-

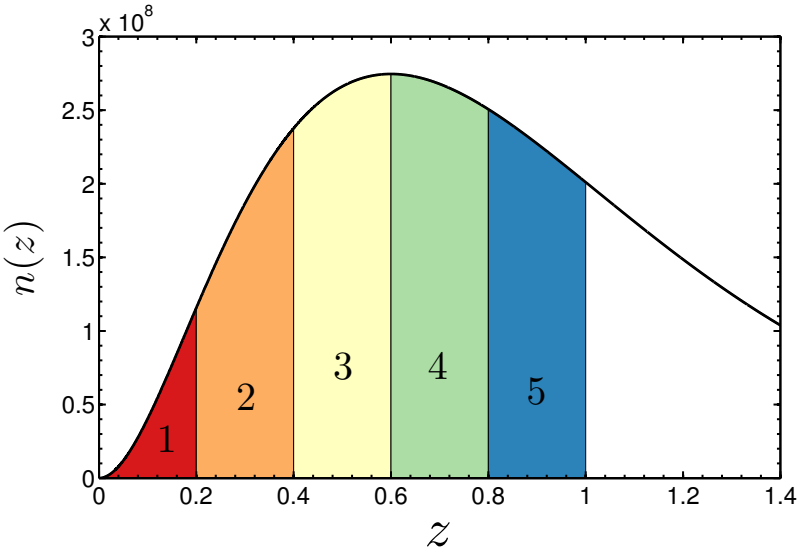

Figure 4.1: Number density of galaxies per steradian for our fiducial survey. Galaxies are assigned to the five redshift bins in proportion to the areas of the coloured regions, each spanning $\Delta z = 0.2$.

ity. In a full analysis, one should parametrize the bias appropriately and marginalize, since the bias parameters may have significant uncertainties and be somewhat degenerate with cosmological parameters. Allowing the dark energy equation of state to vary with time as $w(a) = w_0 + w_a(1-a)$ [52], our fiducial parameter space is therefore five-dimensional (Ω_m, w_0, w_a, n_s, A_s), though we briefly consider a constant equation of state (with fixed $w_a = 0$) as well.

4.3 Results

4.3.1 Biases from multiplicative errors

H13 used a similar formalism to study the effect of arbitrary photometric calibration errors on cosmological parameters. The large biases that resulted were primarily due to additive errors (the $C_\ell^{\rm cal}$ term in Eq. (4.13)), which strongly biased the power spectrum at low multipoles and which were assumed negligible at smaller scales ($C_\ell^{\rm cal} = 0$ for $\ell > \ell_{\rm max,\,cal}$). With the exception of some parameters (e.g. $f_{\rm NL}$), most of the constraining power on cosmological parameters, including dark energy parameters, comes from high ℓ, where there are many more modes to minimize cosmic variance. The simplest way to avoid biases due to these large additive errors at low ℓ is to just remove those multipoles from the analysis, sacrificing the modest amount of information they contain. For our fiducial survey, we find

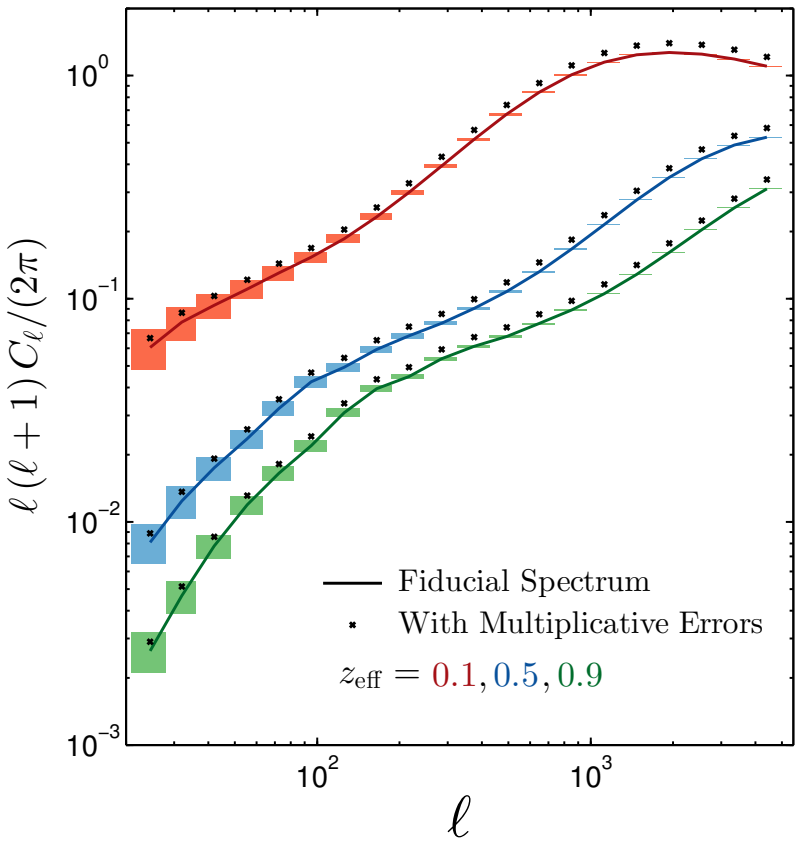

Figure 4.2: Multiplicative effect due to our fiducial calibration errors with $\sigma_c^2 = 0.1$ distributed on large scales $\ell \leq 20$. The biased power spectrum T_ℓ (black points) is compared to the true power spectrum C_ℓ (solid lines) for three of the five redshift bins of our fiducial survey. The spectra are binned in ℓ with inverse-variance weights, and the error boxes include cosmic variance and shot noise.

that this increases the errors on parameters by $\sim$1%, though this number is sensitive to the model and which parameters are varied. Alternatively, with detailed modelling of the systematic effects, one can attempt to remove the contaminated modes and obtain useful cosmological information from the low multipoles.

The problem is not so simple when there are significant *multiplicative* errors, corresponding to the other terms in Eq. (4.13), where a given multipole is not only affected by calibration errors at that scale, but also calibration errors from every other multipole. Ignoring or cleaning the low-ℓ information is not helpful here, since the biases have already "leaked" into the high-ℓ power. The multiplicative errors are much smaller (by a factor of order C_ℓ) than the additive errors, but for a large total amount of contamination, the effects can be important.

In Fig. 4.2, we show our fiducial power spectra along with the same power spectra when biased due to multiplicative errors, for three of the five redshift bins. The spectra are

binned with inverse-variance weights, and the error boxes represent the combined cosmic variance and shot noise error for each bin. For definitiveness, we assume a spectrum for the calibration systematics of $C_\ell^{\rm cal} \propto \ell^{-2}$ (separately for each redshift bin) and impose a cutoff such that $C_\ell^{\rm cal} = 0$ for $\ell > \ell_{\rm max,\,cal} = 20$. A variance of the calibration-error field across the sky of $\sigma_c^2 = 0.1$ is assumed. Recall that this quantity is related to the power spectrum of calibration errors by $\sigma_c^2 \equiv {\rm Var}[c(\hat{\boldsymbol{n}})] = \sum_{\ell=1}^{\infty}(2\ell+1)C_\ell^{\rm cal}/(4\pi)$. While this is a large contamination, it may not be unrealistic for a survey like DES, since the relevant error is the raw variation in the effective magnitude limit before any attempts to clean or remove it. While the cleaning or marginalization methods effectively remove the additive contribution, the $C_\ell^{\rm cal}$ term in Eq. (4.13), the original multiplicative effects remain.

Note that the *factor* by which the power is increased by the multiplicative errors is relatively constant, but since cosmic variance decreases at higher ℓ, the biases eventually become larger than the errors. From the approximate expression Eq. (4.15), we can easily estimate this relative bias in the space of observables. The multiplicative bias is $\sigma_c^2\, C_\ell$, while the variance is given by Eq. (4.16). Ignoring the shot noise contribution, the bias relative to the error is therefore

$$\frac{T_\ell - C_\ell}{\sigma_{C_\ell}} \simeq \sqrt{\frac{(2\ell+1)\,f_{\rm sky}}{2}}\,\sigma_c^2\,. \tag{4.26}$$

For $\sigma_c^2 = 0.1$, the bias is as large as the error for $\ell \simeq 800$ and twice as large for $\ell \simeq$ 3,000. The biases on bandpowers, such as those shown in Fig. 4.2, are more severe still, as cosmic variance is further reduced by measuring the power spectrum in bins spanning several independent ℓ modes.

Fig. 4.3 shows the effect of the bias from Fig. 4.2 in the space of dark energy parameters w_0 and w_a using information from $\ell = 21$ through $\ell_{\rm max} =$ 2,000. In this case, both w_0 and w_a are shifted from their fiducial values by more than 3σ.

Fig. 4.4 shows the effect of these same biases in the full space of our cosmological parameters. We plot $\Delta\chi^2$ as a function of the maximum multipole $\ell_{\rm max}$ used in the analysis, where $\Delta\chi^2 = \delta\mathbf{p}^\top\mathbf{F}\,\delta\mathbf{p}$. For the five-dimensional space of all parameters, this is equivalent to the observable-space $\Delta\chi^2$ in the Fisher matrix formalism. In this case, χ^2 is shifted by 3σ for $\ell_{\rm max} \simeq 100$. We also show $\Delta\chi^2$ for the two-parameter spaces of Ω_m and w (marginalizing over A_s and n_s but fixing $w_a = 0$) and for w_0 and w_a (marginalizing over the other three parameters). In these cases, χ^2 is shifted by more than 3σ for $\ell_{\rm max} \simeq$ 2,500. Notice that the sizes of the biases oscillate somewhat; since the Fisher derivatives sometimes flip sign, the biases will cancel for some $\ell_{\rm max}$. This subtlety depends strongly on which parameters are of interest, apparent here from the "out-of-phase" cancelling between

the constant-w and w_0–w_a dark energy parametrizations. It is therefore the envelope of the bias curves in the Ω_m–w and w_0–w_a spaces that indicates the bias one can realistically expect.

Although we fix the galaxy bias in this illustration, it is worth mentioning that the effect at high ℓ of a constant (scale-independent) galaxy bias is almost completely degenerate with the multiplicative effect from low ℓ (see Eq. (4.15) with $C_\ell^{\rm cal} = 0$). In other words, if the contaminated low multipoles are removed from the analysis and the galaxy bias is constrained along with other cosmological parameters, the inferred value of the galaxy bias will shift due to the multiplicative effect, but the marginalized constraints on the other cosmological parameters will not be significantly biased. Of course, if the galaxy bias exhibits scale dependence or can be known independently to a good precision (which we effectively assumed here), this will not be the case.

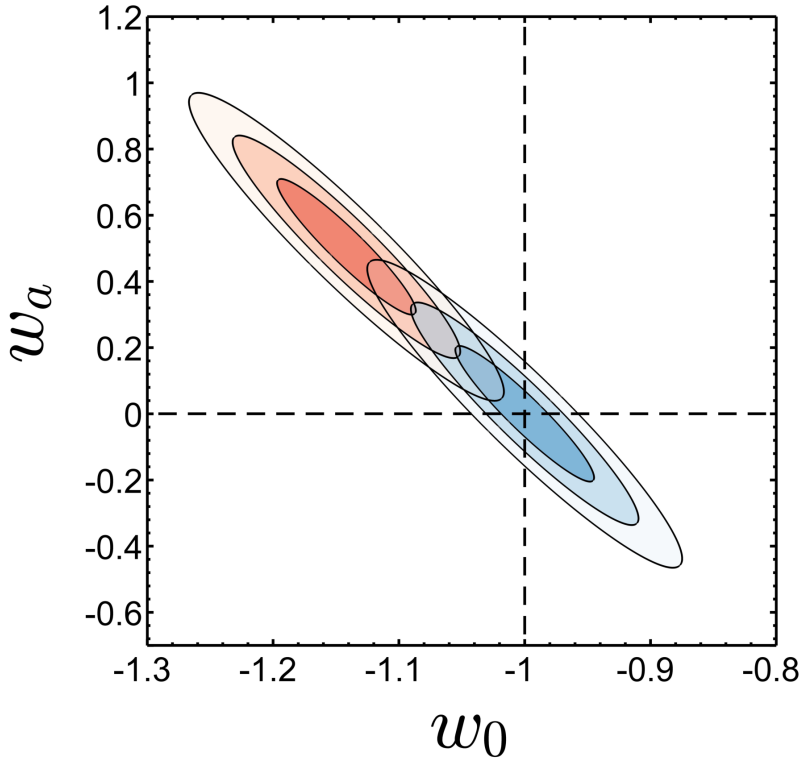

Figure 4.3: Forecasted 68.3, 95.4, and 99.7 per cent joint constraints on the w_0–w_a dark energy parametrization for our fiducial survey, using information from $\ell = 21$ through $\ell_{\rm max} = 2{,}000$ without calibration errors (blue) and with multiplicative calibration errors from $\ell \leq 20$ with $\sigma_c^2 = 0.1$ (red).

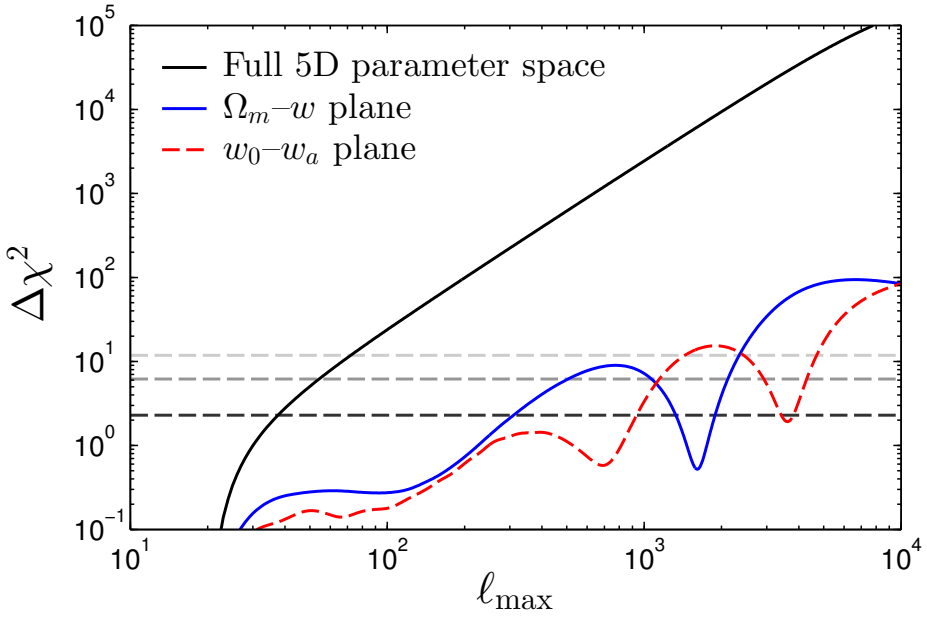

Figure 4.4: Shift in parameter-space χ^2 due to multiplicative calibration errors as a function of the maximum multipole used in the analysis. We show the effect on the full five-dimensional space of parameters (black) along with the two-dimensional spaces of Ω_m and w with fixed $w_a = 0$ (blue) and w_0 and w_a (red). The overlaid dashed grey lines mark the 68.3, 95.4, and 99.7 per cent bounds for a *two-dimensional* Gaussian distribution (for comparison with the red or blue lines).

4.3.2 Self-calibration to remove multiplicative errors

We now study the possibility of measuring the contamination directly at low multipoles to correct the power at high multipoles. Due to large cosmic variance, the low-ℓ $C_\ell^{\rm cal}$ are not known precisely, and for a cut sky, there will be very few modes to inform us about the lowest-ℓ $C_\ell^{\rm cal}$. In practice, the T_ℓ would be measured in bandpowers, so one could then measure the calibration error in bandpowers, but for our purposes here, we assume that each $C_\ell^{\rm cal}$ can be measured with an associated error due to cosmic variance of the true power (and shot noise, though it is negligible at the relevant low multipoles). Note that in our Fisher formalism we are ignoring any additional errors that may result from imperfectly extracting T_ℓ from the cut sky, though these could be estimated in principle [116, 122, 123].

To study the effect of a self-calibration procedure, we consider the example in Sec. 4.3.1, where a calibration power spectrum $C_\ell^{\rm cal} \propto \ell^{-2}$ with $\sigma_c^2 = 0.1$ and $\ell_{\rm max,\,cal} = 20$ has been added to each of the fiducial power spectra. We introduce the $C_\ell^{\rm cal}$ as nuisance parameters to be constrained along with the cosmological parameters. Since $\ell_{\rm max,\,cal} = 20$, there are 20 calibration-error parameters for each of five redshift bins, for a total of 100 nuisance parameters. Using the Fisher matrix formalism discussed in Sec. 4.2.2, we can

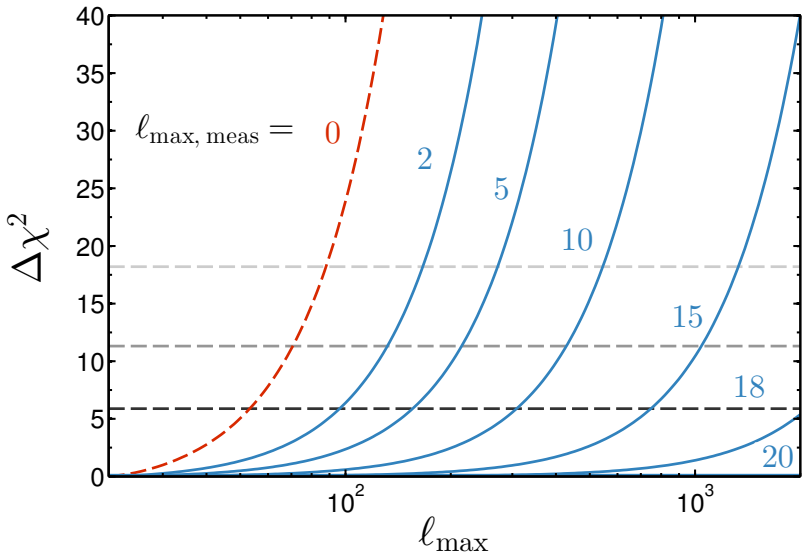

Figure 4.5: Shift in the full five-dimensional parameter-space χ^2 due to multiplicative calibration errors as a function of the maximum multipole used in the analysis, for calibration-error parameters measured up to various $\ell_{\rm max,\ meas}$. The overlaid dashed grey lines mark the 68.3, 95.4, and 99.7 per cent bounds for a five-dimensional Gaussian distribution.

estimate the additional statistical error on cosmological parameters that results from imperfectly measuring the $C_\ell^{\rm cal}$.

In Fig. 4.5, we show the effect of measuring $C_\ell^{\rm cal}$ up to a variety of $\ell_{\rm max,\ meas}$ by plotting $\Delta\chi^2$ (in the five-dimensional parameter space of Ω_m, w_0, w_a, n_s, and A_s) due to the remaining bias, as a function of the maximum multipole $\ell_{\rm max}$ used in the analysis. In other words, for $\ell_{\rm max,\ meas} = x$, we constrain $5x$ total nuisance parameters. For $\ell_{\rm max,\ meas} = 20$, $\Delta\chi^2 = 0$ for all $\ell_{\rm max}$, since the assumption is that all of the calibration terms have been measured without significant bias. Note the very large biases in the cosmological parameters when $\ell_{\rm max,\ meas}$ is low; that is, when we have not used measurements of additive error at sufficiently many low multipoles to effectively "clean" the high-multipole LSS information.

In Fig. 4.6, we show the statistical error and remaining bias in the w_0 and w_a dark energy parameters as a function of the maximum multipole $\ell_{\rm max,\ meas}$ at which calibration errors are measured. For both parameters, the statistical errors increase modestly (by $\sim$50%), while the biases approach zero at $\ell_{\rm max,\ meas} = \ell_{\rm max,\ cal}$. In this specific case, it is apparent that one would need to measure systematics to $\ell \simeq 10$ in order to reduce the biases to a comfortable level (such as $\sim 1/4$ of the statistical error).

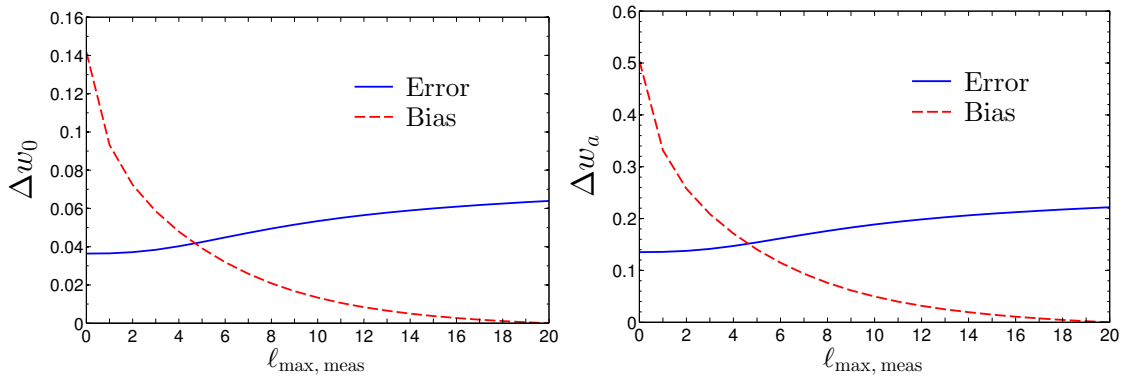

Figure 4.6: Statistical error (blue) and bias (dashed red) on w_0 (left) and w_a (right) as a function of the maximum multipole $\ell_{\rm max,\ meas}$ at which calibration errors are measured.

4.4 Discussion

In this paper, we have considered a general class of systematic errors – photometric calibration errors – that contaminate measurements of the galaxy angular power spectrum. These errors arise from any effect which causes a spatial variation in the effective magnitude limit of the photometric survey, modulating the true galaxy number densities and biasing the angular power spectrum (see Eq. (4.13)). More specifically, we studied the effect of *multiplicative* errors, where calibration error at any scale biases inferences of the power spectrum at all other scales. In this case, cleaning the power spectra of excess additive power, or excluding contaminated multipoles from the analysis, does not remove the multiplicative effect. For a large total amount of contamination, the multiplicative effect can significantly bias cosmological parameters (Figs. 4.3–4.4).

Given the fact that these calibration errors tend to affect primarily large angular scales (for instance $\ell \lesssim 20$), we proposed a possible method of "self-calibrating" the survey by using the largest angular scales to measure the contamination itself, which can then be removed from small scales where most of the information on cosmological parameters resides. We studied a fiducial DES-like survey, using Fisher matrix formalism to forecast errors and biases in cosmological parameters given the survey parameters and our assumed photometric calibration error. We then extended the Fisher matrix to include the low-multipole calibration powers as nuisance parameters. For a modest increase in statistical uncertainty, one can remove the biases in cosmological parameters, including those describing dark energy (Fig. 4.6).

We now briefly discuss how this method could be applied to real data. One clear problem with the procedure is the near-perfect degeneracy at large scales between the additive calibration-error power and cosmological parameters. This means that nearly all of the

information on cosmological parameters must come from small scales. While little information on most cosmological parameters comes from the largest scales, a major exception is the non-Gaussianity parameter $f_{\rm NL}$, on which *most* information comes from these scales (see fig. A1 of H13), making its measurement difficult with this procedure. On the other hand, it may be possible to incorporate cross-power spectra from overlapping redshift bins and cross-correlations with other probes into this formalism. The extra information, which may not be subject to the same systematics, could be used to constrain parameters like $f_{\rm NL}$ along with the general calibration-error parameters.

The other important assumption is that one can safely ignore all additive error above some multipole $\ell_{\rm max,\,cal}$. For our illustration here, we assumed $\ell_{\rm max,\,cal} = 20$, though this is optimistic, and one could easily make the cutoff somewhere else. While photometric calibration error from known systematics tends to decrease sharply at smaller scales, some contamination may still be present at higher multipoles. Although one can probably assume that the extra multiplicative effect from any of these (smaller) additive errors is negligible, the additive errors themselves would need to be removed via other means.

One could thus imagine using this procedure in conjunction with mode projection and other cleaning techniques, using the cleanest possible small-scale spectrum but still retaining the fully contaminated spectrum at large scales to constrain the calibration-error parameters. This procedure would be particularly useful if one is worried about unknown sources of calibration error but willing to assume that these add significant power to multipoles below some cutoff only.

Finally, if one is doubtful about removing all of the smaller-scale additive contamination using standard cleaning techniques, the only way forward would be to choose a more conservative $\ell_{\rm max,\,cal}$ that is high enough for one to comfortably assume that the bias in the remaining small-scale spectrum is due only to the multiplicative effect from the larger scales.

CHAPTER 5

Testing Power Law Cosmology with Model Comparison Statistics

5.1 Introduction

Despite the general observational success of ΛCDM in describing the detailed properties of the Universe and its expansion, some alternative models for expansion have been proposed. A notable alternative is power law cosmology, where the scale factor evolves purely as a function of the proper time (age) to some constant power. While constraints from Big Bang nucleosynthesis suggest that a power law model cannot describe the complete expansion history of the Universe [124, 125], it may be more plausible as a description of a low-redshift modified-gravity alternative to the cosmological constant. For instance, power law expansion could result from a coupling of classical fields to spacetime curvature, regardless of matter content (e.g. [126]). Theoretical motivation aside, it is instructive to compare alternative models with ΛCDM to test the robustness of the data and their ability to discriminate between competing models.

Power law expansion has been shown (e.g. [127–129]) to be consistent with a variety of cosmological probes for a power law exponent in the range $1 \lesssim n \lesssim 1.5$. More recently, [130] studied power law cosmology using current data from observations of Type Ia supernovae (SNe Ia) and baryon acoustic oscillations (BAO). They found that low-redshift power law cosmology is a good fit to the SN Ia data if the power law exponent has a value $n \simeq 1.5$. Here we will study similar data, but rather than simply constrain the model parameters and confirm that one can find a good fit, we would like to explicitly compare power law cosmology with ΛCDM. We will use several alternative model comparison statistics to determine if (and if so, how strongly) various data combinations prefer power law expansion over ΛCDM.

A similar alternative to ΛCDM is the so-called $R_\mathrm{h} = ct$ universe proposed by [131], where $R_\mathrm{h} = c/H(t)$ is the Hubble radius. Though presented as a distinct model, the

expansion history of $R_\mathrm{h} = ct$ matches that of a power law with exponent $n = 1$ (a constant rate of expansion). Note that a constant rate of expansion has been studied earlier [132, 133] under the name "linear coasting cosmology."

Whether or not the $R_\mathrm{h} = ct$ model is unphysical has been debated in the literature. Aside from the nucleosynthesis arguments [124, 125] that apply to power law expansion in general, [134] points out that the $R_\mathrm{h} = ct$ universe, which is constrained to have an effective equation of state $\bar{w} = -1/3$, requires either that $\Omega_m = 0$ or that the dark energy equation of state evolves in an unphysical way at early times. In a response, [135] argues that the assumption of a conserved matter field is not justified even at late times, though one might view this as rather contrived. The idea of R_h as a meaningful cosmic horizon has also been challenged [136]. Setting these important concerns aside, we may still ask whether the observations favor $R_\mathrm{h} = ct$ expansion as a phenomenological description of the late Universe.

An analysis by [137] determined that the $R_\mathrm{h} = ct$ universe is ruled out by both SN Ia data and $H(z)$ data (from BAO and cosmic chronometers) separately, though, as pointed out in [138], the conclusions are based heavily on visual inspection of plots of reconstructed dynamical quantities. While there is nothing wrong with this dynamical approach, and while the inconsistency with $R_\mathrm{h} = ct$ indeed appears quite significant, direct model comparison can quantify the preference of the data and appropriately account for differences in model complexity. That analysis also ignores systematic errors in the SN Ia measurements, and these are significant for current data. In addition, proponents of $R_\mathrm{h} = ct$ cosmology have argued [139, 140] that using SN Ia data may be unfair anyway because of hidden model dependence.

In this paper, we test both power law cosmology and, separately, the $R_\mathrm{h} = ct$ cosmology against ΛCDM using current data and robust model comparison statistics. The outline of the rest of the paper is as follows. In Sec. 5.2, we briefly review these three models for cosmic expansion. In Sec. 5.3, we describe the datasets we will use, and in Sec. 5.4, we review the goodness-of-fit and model comparison statistics. Our results are presented in Sec. 5.5. Finally, in Sec. 5.6, we discuss the issue of hidden model dependence in the SN Ia data, explaining why there is no real problem, before summarizing our conclusions.

5.2 Models

In this section, we briefly describe the three models we wish to compare: ΛCDM, power law cosmology, and the $R_\mathrm{h} = ct$ cosmology.

5.2.1 ΛCDM

The flat ΛCDM model is considered the standard model of modern cosmology, and it is motivated by a combination of physics and empirical observations. In the ΛCDM framework, the present-day Universe consists mostly of cold dark matter and the simplest form of dark energy, the cosmological constant Λ. The ΛCDM model is usually described as having six free parameters (e.g. Ω_m, $\Omega_c h^2$, $\Omega_b h^2$, n_s, A_s, τ), remarkably simple for a model that describes the Universe as a whole (for comparison, the Standard Model of particle physics has 19 free parameters). Moreover, if the focus is only on late-time relative expansion, there is really only one free parameter, which we take to be Ω_m. For a flat universe, the present cosmological-constant density is fixed to the value $\Omega_\Lambda = 1-\Omega_m$, and the comoving angular diameter distance $r(z)$ coincides with the line-of-sight comoving distance:

$$r(z) = \frac{c}{H_0}\int_0^z \frac{dz'}{E(z')}\,, \tag{5.1}$$

$$E(z) \equiv \frac{H(z)}{H_0} = \sqrt{\Omega_m(1+z)^3 + (1-\Omega_m)}\,. \tag{5.2}$$

Note that, since we are focusing on low-redshift expansion only, we can ignore contributions to $H(z)$ from radiation or relativistic neutrinos, which have a negligible impact on expansion to the precision we are concerned with here.

5.2.2 Power law and $R_\mathbf{h} = ct$ cosmology

In power law cosmology, the scale factor evolves with proper time (age) as

$$a(t) = \left(\frac{t}{t_0}\right)^n, \tag{5.3}$$

where $a_0 = a(t_0) = 1$ is the present value. In this case, we have

$$E(z) = (1+z)^{1/n}, \tag{5.4}$$

so that

$$r(z) = \frac{c}{H_0} \times \begin{cases} \dfrac{(1+z)^{1-1/n}-1}{1-1/n}, & n \neq 1\,, \\ \\ \ln(1+z), & n = 1\,. \end{cases} \tag{5.5}$$

Here there is one free parameter, the power law exponent n, which can be restricted to be in the range $0 < n < \infty$ if we agree we live in an expanding universe. Since the data

combinations we will analyze here all exclude $n \leq 0$ anyway, this restriction does not affect our analysis.

The $R_\mathrm{h} = ct$ universe [131], though proposed as a distinct model, has an expansion history that matches that of a power law with $n = 1$. In the definition, R_h is the gravitational radius, which is equivalent to the Hubble radius $R_\mathrm{h} = c/H(t)$ for a flat universe, so one can also write $Ht = 1$ to describe this model. The comoving angular diameter distance is then given by the second case in Eq. (5.5). There are no free parameters in this model, so only nuisance parameters associated with the data can be varied.

Note that we are assuming a flat universe for these models as well, an assumption which can be relaxed (e.g. [130]). Flatness is empirically motivated (e.g. [7]) for ΛCDM-like models, where Ω_k is constrained to be small, but the tightest constraints are somewhat model-dependent since they rely on CMB observations (see Sec. 5.3.2). On the other hand, if the inflationary picture is correct, we still have strong theoretical motivation to assume a flat universe, and we proceed with this assumption.

5.3 Data Sets

We now describe in some detail the data used in the analysis. It is crucial that we only choose data whose interpretation is independent of the cosmological model. To this end, we consider SN Ia observations as well as measurements of the BAO feature in large-scale structure. These are among the most mature, well-studied, and robust probes of dark energy and cosmic expansion at present. In this section and also in Sec. 5.6, we discuss some important issues related to the model-independence of these data.

We intentionally do not use some other measurements of distance and expansion rate, such as cosmic chronometers (e.g. [141, 142]), which measure $H(z)$ directly by estimating the ages of passively evolving galaxies. While very promising, this method is newer and less well-studied, and the systematic errors on individual measurements are often as large as the statistical errors. In addition, we leave out measurements of the CMB distance because the measurement is at least somewhat model-dependent (see Sec. 5.3.2).

5.3.1 SN Ia data

Type Ia supernovae (SNe Ia) are very bright standard candles (or *standardizable* candles) that are useful for measuring cosmological distances. SNe Ia alone provided the first convincing evidence for accelerated cosmic expansion [8, 9]. Today, not only have we observed many more SNe, but we have also improved our understanding of their light curves

and performed rigorous analyses of systematic errors (e.g. [17, 71, 83, 143]). Although measurements of CMB anisotropies and large-scale structure can constrain the matter content of the Universe and even the dark energy equation of state, SNe Ia have an important role in breaking degeneracies to achieve precision constraints on dark energy.

The distance modulus of a SN at redshift z is given by

$$\mu(z) = 5 \log_{10} \left[\frac{H_0}{c} D_L(z) \right], \tag{5.6}$$

where $D_L(z) = (1+z)\, r(z)$ is the luminosity distance. Here we have defined the distance modulus without the H_0 term, which is degenerate with the SN Ia absolute magnitude (see below).

Useful correlations between the peak luminosity of SNe Ia and both the stretch (or broadness) and photometric color of their light curves improve the standardization of SNe Ia by reducing the intrinsic scatter in their luminosities (and simultaneously mitigating potential systematic effects). Simply put, a broader or bluer SN light curve corresponds to a brighter SN. More recently, it has become apparent that properties of the host galaxy correlate with the intrinsic luminosity as well, and understanding these effects is the focus of much current work (e.g. [81, 87, 144]). It is now common practice to fit for two absolute magnitudes, splitting the sample using a stellar mass cut of the host galaxy. We therefore compare the predicted distance modulus with its measured value after light-curve correction:

$$\mu_{\rm obs} = m - (\mathcal{M} - \alpha\, s + \beta\, C + P\, \Delta M), \tag{5.7}$$

where m is the apparent magnitude in some photometric band, s and C are the stretch and color measures, which are specific to the light-curve fitter (e.g. SALT2 [37]) employed, and $P \equiv P(M_* > 10^{10} M_\odot)$ is the probability that the SN occurred in a high-stellar-mass host galaxy. The stretch, color, and host-mass coefficients (α, β, and ΔM, respectively) are nuisance parameters that should ideally be constrained along with any cosmological parameters. The constant $\mathcal{M} = M - 5 \log_{10}[H_0/c \times 10\ \text{pc}]$ absorbs the H_0 term from Eq. (5.6) and is yet another nuisance parameter.

Recent analyses (see below) have concentrated on estimating correlations between measurements of individual SNe in order to appropriately account for the numerous systematic effects which must be controlled in order to improve constraints significantly beyond their current level. A complete covariance matrix for SNe Ia includes estimates of all identified systematic errors in addition to the intrinsic scatter and other statistical errors. The χ^2

statistic is then calculated in the usual way for correlated measurements:

$$\chi^2 = \Delta\boldsymbol{\mu}^{\intercal}\mathbf{C}^{-1}\Delta\boldsymbol{\mu}\ , \tag{5.8}$$

where $\Delta\boldsymbol{\mu} = \boldsymbol{\mu}_{\rm obs} - \boldsymbol{\mu}(\boldsymbol{\theta})$ is the vector of residuals between the observed, corrected distance moduli and the theoretical predictions that depend on the set of cosmological model parameters $\boldsymbol{\theta}$ and $\mathbf{C}$ is the $N_{\rm SN} \times N_{\rm SN}$ covariance matrix for the observed distance moduli.

In this work, we use current SN Ia datasets from two alternative analyses: the joint light-curve analysis (JLA) of SNe from the Supernova Legacy Survey (SNLS) and the Sloan Digital Sky Survey (SDSS) and the Supernova Cosmology Project's Union2.1 compilation.

5.3.1.1 JLA

The joint light-curve analysis (JLA) [145] includes recalibrated SNe from the first three years of SNLS [17, 75] as well as the complete SN sample from SDSS [146], and it is the largest combined SN analysis to date. The final compilation includes 740 SNe, ∼100 low-redshift SNe from various subsamples, ∼350 from SDSS at low to intermediate redshifts, ∼250 from SNLS at intermediate to high redshifts, and ∼10 high-redshift SNe from the Hubble Space Telescope.

We use the SN Ia data and individual covariance matrix terms provided[1] to compute the full covariance matrix, which includes statistical errors and all identified systematic errors. The covariance matrix, like the corrected distance moduli themselves, is a function of the light-curve nuisance parameters α and β. In the analysis, we vary all of the SN Ia nuisance parameters (α, β, $\mathcal{M}$, ΔM), recomputing the covariance matrix whenever α or β is changed.

5.3.1.2 Union2.1

The Union2.1 analysis [25] from the Supernova Cosmology Project[2] adds ∼15 high-redshift SNe to the Union2 compilation [24], making Union2.1 the compilation with the most high-redshift SNe (∼30 at $z > 1$) to date.

The SN distance moduli provided have been pre-corrected for stretch, color, and host-mass correlations using best-fit values for α, β, and ΔM. While we do include all identified systematic errors via the covariance matrix provided, we keep α and β fixed at their best-fit values in the analysis because the covariance matrix is a function of these parameters and individual covariance matrix terms are not provided. While fixing α and β is unlikely

[1] http://supernovae.in2p3.fr/sdss_snls_jla/
[2] http://supernova.lbl.gov/Union/

to affect the results of our model comparison (see Sec. 5.5), it is important to allow the effective value of the SN Ia absolute magnitude to change, so we let both $\mathcal{M}$ and ΔM vary in the analysis.

5.3.2 BAO data

Baryon acoustic oscillations (BAO) are the regular, periodic fluctuations of visible matter density in large-scale structure resulting from sound waves propagating in the early Universe. In recent years, precise measurements of the BAO scale at a variety of redshifts have proven to be effective probes of cosmic expansion and dark energy [16, 147]. The principal observable is the *ratio* of the BAO distance scale at low redshift to the comoving sound horizon $r_d = r_s(z_d)$ at the redshift of baryon drag ($z_d \simeq 1060$, shortly after recombination at $z_* \simeq 1090$).

Typically the BAO feature is assumed to be isotropic and is identified from a spherically-averaged power spectrum. In this case, the observable is $D_V(z_{\rm eff})/r_d$, where D_V is a spherically-averaged (two transverse and one radial) distance measure [10] given by

$$D_V(z) \equiv \left[r^2(z) \, \frac{cz}{H(z)} \right]^{1/3} , \tag{5.9}$$

where $r(z) = (1+z)\, D_A(z)$ is the comoving angular diameter distance and $H(z)$ is the Hubble parameter. More recently, it has become possible to robustly measure radial and transverse clustering separately, allowing for anisotropic BAO. In that case, the observables $r(z_{\rm eff})/r_d$ and $c/(H(z_{\rm eff})\, r_d)$ are measured separately (but with some statistical correlation).

We follow [147] and combine recent measurements of the BAO feature from the Six-degree-Field Galaxy Survey (6dFGS) [11], the SDSS-II DR7 main galaxy sample (MGS) [104], and the SDSS-III Baryon Oscillation Spectroscopic Survey (BOSS) DR11 LOWZ [12] and CMASS [13] samples. We also include a combined measurement from BOSS Lyman-α forest (LyαF) auto-correlation [14] and cross-correlation [148]. We use pairs of anisotropic measurements for the CMASS and LyαF samples and isotropic measurements for the others.

The BAO measurements used in this analysis are summarized in Table 5.1. As discussed in [147], statistical correlations (covariance) between these different samples should be negligible, so we treat them as independent in the analysis. Note that the CMASS anisotropic measurements are correlated with coefficient -0.52, while the LyαF measurements are correlated with coefficient -0.48.

The likelihood for the BAO observables is not Gaussian far from the peak. For a finite

Sample	$z_{\rm eff}$	Observable	Measurement
6dFGS	0.106	$D_V(z_{\rm eff})/r_d$	3.047 ± 0.137
SDSS MGS	0.15	$D_V(z_{\rm eff})/r_d$	4.480 ± 0.168
BOSS LOWZ	0.32	$D_V(z_{\rm eff})/r_d$	8.467 ± 0.167
BOSS CMASS	0.57	$r(z_{\rm eff})/r_d$	14.945 ± 0.210
BOSS CMASS	0.57	$c/(H(z_{\rm eff})\, r_d)$	20.75 ± 0.730
BOSS LyαF	2.34	$r(z_{\rm eff})/r_d$	36.489 ± 1.152
BOSS LyαF	2.34	$c/(H(z_{\rm eff})\, r_d)$	9.145 ± 0.204

Table 5.1: Summary of BAO measurements combined in this analysis. We list the sample from which the measurement comes, the effective redshift of the sample, the observable quantity constrained, and its measured value. The anisotropic measurements from BOSS CMASS are correlated with coefficient -0.52, while those from BOSS LyαF are correlated with coefficient -0.48. Otherwise, we assume the measurements to be statistically independent.

detection significance of the BAO feature, the actual likelihood will eventually asymptote to a flat tail, since any value for the observable is equally probable in the event of a non-detection [59]. This is particularly important to consider when constraining parameters to a high confidence level or claiming that a model is a very poor fit to the data.

We account for this effect by applying the fitting function proposed in [59] to approximate the correct likelihood. For a given signal-to-noise ratio (S/N), the usual $\Delta\chi^2_{\rm G} = -2\ln\mathcal{L}_{\rm G}$ for an observable with a Gaussian likelihood is replaced by

$$\Delta\chi^2 = \frac{\Delta\chi^2_{\rm G}}{\sqrt{1 + \Delta\chi^4_{\rm G}\left(\frac{S}{N}\right)^{-4}}}\,. \tag{5.10}$$

Here, the S/N corresponds to the reported detection significance, in units of σ, of the BAO feature. For further explanation of this effect and how it relates to BAO measurements, see [1, 59]. Note that if $\Delta\chi^2_{\rm G}$ is a combined value for multiple measurements, such as a pair of anisotropic BAO measurements, the relevant $(S/N)^2$ is the Gaussian $\Delta\chi^2$ value that corresponds to the detection *probability*. For instance, $(S/N)^2 = 6.18$ rather than 4.00 for a 2σ (95.4%) detection and a $\Delta\chi^2_{\rm G}$ with two degrees of freedom (see e.g. [149]).

The detection significance quoted for 6dFGS is 2.4σ. For SDSS MGS, the detection significance is roughly 2σ, but since the likelihood is non-Gaussian anyway, we apply Eq. (5.10) to the publically-available χ^2 look-up table. We also truncate its $\Delta\chi^2$ contribution at $\Delta\chi^2 = 3.43$ to avoid extrapolating beyond the edge of the table. No detection significance was explicitly quoted for BOSS LOWZ, so we assume a 4σ detection as a conservative guess. The quoted detection significance is more than 7σ for BOSS CMASS,

but we use a value of 6σ in the analysis, in case the likelihood becomes non-Gaussian for other reasons at such a high confidence level. Finally, for BOSS LyαF, the detection significance is 5σ for the auto-correlation measurement and roughly 4σ for the cross-correlation measurement. Since these measurements are almost completely independent (see [14]), we simply add their publically-available χ^2 tables. Although the combined detection significance is presumably higher, we apply Eq. (5.10) to the combined χ^2 table assuming a significance of only 4σ. We then truncate the $\Delta\chi^2$ contribution at $\Delta\chi^2 = 15.93$ (less than 4σ for two degrees of freedom) to avoid any extrapolation beyond the table. We have verified that the final results are qualitatively insensitive to the exact choices here and quantitatively sensitive to only the LyαF BAO significance, which we discuss in Sec. 5.5.

Measurements of the BAO scale are typically calibrated by the CMB, which effectively fixes the sound horizon r_d by precisely constraining $\Omega_m h^2$ and $\Omega_b h^2$. Here we avoid using the CMB to measure the sound horizon, as this measurement is model-dependent. To this end, we simply allow r_d to be a free parameter, effectively using only *relative* distance information from BAO. This is analogous to SN Ia analysis, where one usually marginalizes over the SN Ia absolute magnitude, using only relative distance information to constrain dark energy. The CMB also provides its own precise measurement of the angular diameter distance to recombination at $z_* \simeq 1090$ that breaks degeneracies among the parameters describing expansion. Here we will also leave out this high-redshift distance measurement; while it can be thought of as just another BAO measurement (i.e. $r(z_*)/r_d$), the interpretation is not completely model-independent because the redshift z_* of the CMB cannot be determined without a model. See [147] for further discussion of these different options for calibrating BAO measurements.

5.4 Methodology

In this section, we review the statistics we use to determine goodness-of-fit and perform the model comparison.

5.4.1 Goodness of fit

To determine if a model is a good fit to the data, we minimize χ^2 over the free model parameters and calculate the probability $P(\chi^2_{\rm min}, \nu)$ that a greater $\chi^2_{\rm min}$ could occur due to chance alone for a fit with $\nu = N - k$ degrees of freedom, where N is the total number of

measurements and k is the number of free model parameters. This probability is given by

$$P(\chi^2, \nu) = \frac{\Gamma\left(\frac{\nu}{2}, \frac{\chi^2}{2}\right)}{\Gamma\left(\frac{\nu}{2}\right)}, \tag{5.11}$$

where $\Gamma(s, x)$ is the upper incomplete gamma function,

$$\Gamma(s, x) = \int_x^\infty t^{s-1} e^{-t} dt \, , \tag{5.12}$$

and $\Gamma(s) = \Gamma(s, 0)$ is the (complete) gamma function.

5.4.2 Model comparison

We will use three alternative methods for model comparison. Formally, the different statistics have different meanings and are valid under different assumptions, so obtaining consistent results using different criteria mitigates the possibility that invalid assumptions about the nature of the data will favor one model over another and lead to invalid conclusions. Each of these statistics accounts for the fact that a simpler model (one with fewer free parameters) is preferable to a more complex model if both fit the data similarly well. Note that they do not require the different models to be nested; while $R_\mathrm{h} = ct$ is nested within power law cosmology, neither is nested with ΛCDM. For more information about these statistics, and for other interesting uses of model comparison in cosmology, see [150–156].

The Akaike information criterion (AIC) [157], which is grounded in information theory, estimates how much more information is lost when describing data with one model over another. For a best-fit χ^2_min and a model with k free parameters, AIC is given by

$$\mathrm{AIC} = \chi^2_\mathrm{min} + 2k \, . \tag{5.13}$$

This is an asymptotic expression, and a second-order correction term can be added to make the criterion more accurate for a finite number of observations:

$$\mathrm{AICc} = \mathrm{AIC} + \frac{2k\,(k+1)}{N-k-1} \, . \tag{5.14}$$

This makes a small difference when the number of data points N is large (e.g. for the SN data) but a significant difference if N is small (e.g. for the BAO data). Since AICc reduces to AIC in the limit of large N, we use AICc instead of AIC throughout the analysis.

The Bayesian information criterion (BIC) [158] is also an asymptotic expression, and

it follows from a Bayesian argument that considers likelihoods in the exponential family of probability distributions, which includes the Gaussian distribution and many other common distributions. BIC selects the model that is a posteriori most probable. It is given by

$$\text{BIC} = \chi^2_{\text{min}} + k \ln(N) \ . \tag{5.15}$$

BIC typically (though not always) penalizes extra parameters more severely than AIC.

The Bayes factor B_{10} indicates the likelihood of one model relative to another by integrating both likelihoods over all values of the model parameters, weighting them by the priors. This statistic is presumably the most robust, as it considers all values, not just the best-fit values, of the parameters. It naturally penalizes a model with more free parameters, especially if those parameters do not lead to a better fit. In fact, BIC can be considered an approximation to the logarithm of the Bayes factor. For a set of data D and two different models M_0 and M_1 that are described, respectively, by sets of parameters $\boldsymbol{\theta}_0$ and $\boldsymbol{\theta}_1$, the Bayes factor indicates the likelihood of M_1 relative to M_0 and is given by

$$B_{10} = \frac{\int \Pr(D|\boldsymbol{\theta}_1, M_1) \Pr(\boldsymbol{\theta}_1|M_1) \, d\boldsymbol{\theta}_1}{\int \Pr(D|\boldsymbol{\theta}_0, M_0) \Pr(\boldsymbol{\theta}_0|M_0) \, d\boldsymbol{\theta}_0} \ . \tag{5.16}$$

For this analysis, we take the prior distributions $\Pr(\boldsymbol{\theta}|M)$ to be flat, and we assume that the likelihoods $\Pr(D|\boldsymbol{\theta}, M)$ are Gaussian (this assumption is implicit in our definitions of AIC and BIC, where we write χ^2_{min} in place of the more general $-2\ln(\mathcal{L}_{\text{max}})$). We compute the likelihoods numerically over grids of parameter values. Analytic marginalization over $\mathcal{M}$ and ΔM (e.g. Appendix of [2]) leaves at most four parameters over which to grid, making this brute-force approach feasible.

5.5 Results

Table 5.2 lists the best-fit values for the model parameters, including the nuisance parameters for the SN and BAO data, for each model discussed in Sec. 5.2 and data combination discussed in Sec. 5.3. Table 5.3 shows the results of the model comparison. For each model and data combination, we list the number of parameters k that were varied, the total number of data points N, the best-fit χ^2_{min}, the probability $P(\chi^2_{\text{min}}, \nu)$ that a greater χ^2_{min} could occur due to chance alone for degrees of freedom $\nu = N - k$, and the likelihood of the model relative to ΛCDM for the AICc, BIC, and Bayes factor model comparison statistics. We note that, while statisticians have proposed various scales that give a qualitative interpretation

Model	Data	Ω_m	n	$r_d \times H_0/c$	α	β	$\mathcal{M}$	ΔM
ΛCDM	JLA (Stat)	0.287	-	-	0.140	3.14	24.11	-0.060
ΛCDM	JLA (Sys)	0.294	-	-	0.141	3.10	24.11	-0.070
ΛCDM	Union2.1 (Stat)	0.278	-	-	-	-	43.16	0.000
ΛCDM	Union2.1 (Sys)	0.295	-	-	-	-	43.17	0.000
ΛCDM	BAO	0.285	-	0.0338	-	-	-	-
ΛCDM	BAO + JLA (Stat)	0.286	-	0.0338	0.140	3.14	24.11	-0.059
ΛCDM	BAO + JLA (Sys)	0.288	-	0.0338	0.141	3.10	24.11	-0.070
ΛCDM	BAO + Union2.1 (Stat)	0.282	-	0.0339	-	-	43.16	-0.002
ΛCDM	BAO + Union2.1 (Sys)	0.288	-	0.0338	-	-	43.16	0.001
Power Law	JLA (Stat)	-	1.56	-	0.139	3.14	24.14	-0.061
Power Law	JLA (Sys)	-	1.55	-	0.141	3.10	24.13	-0.071
Power Law	Union2.1 (Stat)	-	1.54	-	-	-	43.20	-0.022
Power Law	Union2.1 (Sys)	-	1.44	-	-	-	43.20	-0.003
Power Law	BAO	-	0.93	0.0301	-	-	-	-
Power Law	BAO + JLA (Stat)	-	1.52	0.0333	0.139	3.13	24.14	-0.062
Power Law	BAO + JLA (Sys)	-	1.45	0.0331	0.140	3.09	24.14	-0.072
Power Law	BAO + Union2.1 (Stat)	-	1.49	0.0332	-	-	43.20	-0.027
Power Law	BAO + Union2.1 (Sys)	-	1.35	0.0326	-	-	43.21	-0.007
$R_\mathrm{h} = ct$	JLA (Stat)	-	-	-	0.131	3.13	24.24	-0.083
$R_\mathrm{h} = ct$	JLA (Sys)	-	-	-	0.138	3.07	24.23	-0.077
$R_\mathrm{h} = ct$	Union2.1 (Stat)	-	-	-	-	-	43.33	-0.115
$R_\mathrm{h} = ct$	Union2.1 (Sys)	-	-	-	-	-	43.29	-0.026
$R_\mathrm{h} = ct$	BAO	-	-	0.0308	-	-	-	-
$R_\mathrm{h} = ct$	BAO + JLA (Stat)	-	-	0.0308	0.131	3.13	24.24	-0.083
$R_\mathrm{h} = ct$	BAO + JLA (Sys)	-	-	0.0308	0.138	3.07	24.23	-0.077
$R_\mathrm{h} = ct$	BAO + Union2.1 (Stat)	-	-	0.0308	-	-	43.33	-0.115
$R_\mathrm{h} = ct$	BAO + Union2.1 (Sys)	-	-	0.0308	-	-	43.29	-0.026

Table 5.2: Best-fit values of each parameter varied for each model and data combination.

of the numerical results of model comparison statistics (e.g. Jeffreys' scale for the Bayes factor), these are obviously rather subjective, so here we simply discuss the results in terms of relative probabilities (e.g. $\exp(-\Delta\mathrm{BIC}/2)$) and let the reader judge their significance.

From Table 5.3, it is clear that ΛCDM is a good fit to all of the SN Ia data. When systematic errors are included, the fit may even be slightly *too* good, indicating that the errors may be overestimated. This would not be surprising, as the SN analyses generally aim to be conservative when estimating the magnitude of systematic errors. A more surprising result is that ΛCDM is actually not a very good fit to the BAO data. The fit, with a probability of 0.052, corresponds to a nearly 2σ discrepancy. This tension has already been noted (e.g. [147]) and is due to the anisotropic LyαF BAO measurements, with the radial measurement $c/(H(2.34)\, r_d)$ too high and the transverse measurement $r(2.34)/r_d$ too low for ΛCDM. This is the case regardless of whether Ω_m and r_d are constrained by CMB observations (e.g. *Planck*) or by the combined set of BAO measurements, as in this analysis. The similar value of Ω_m preferred by both SN Ia and BAO data means extra tension will not arise when combining the data, and so the combined SN + BAO fits are still very good.

Model	Data	k	N	$\chi^2_{\rm min}$	$P(\chi^2_{\rm min}, \nu)$	$\exp(-\Delta\text{AICc}/2)$	$\exp(-\Delta\text{BIC}/2)$	B_{10}
ΛCDM	JLA (Stat)	5	740	722.6	0.62	1	1	1
ΛCDM	JLA (Sys)	5	740	682.7	0.92	1	1	1
ΛCDM	Union2.1 (Stat)	3	580	562.2	0.66	1	1	1
ΛCDM	Union2.1 (Sys)	3	580	545.1	0.83	1	1	1
ΛCDM	BAO	2	7	11.0	0.052	1	1	1
ΛCDM	BAO + JLA (Stat)	6	747	733.6	0.57	1	1	1
ΛCDM	BAO + JLA (Sys)	6	747	693.8	0.89	1	1	1
ΛCDM	BAO + Union2.1 (Stat)	4	587	573.3	0.61	1	1	1
ΛCDM	BAO + Union2.1 (Sys)	4	587	556.1	0.78	1	1	1
Power Law	JLA (Stat)	5	740	725.8	0.59	0.20	0.20	0.17
Power Law	JLA (Sys)	5	740	682.7	0.92	1.0	1.0	0.84
Power Law	Union2.1 (Stat)	3	580	567.6	0.60	0.069	0.069	0.057
Power Law	Union2.1 (Sys)	3	580	547.0	0.81	0.39	0.39	0.28
Power Law	BAO	2	7	8.8	0.12	3.0	3.0	1.3
Power Law	BAO + JLA (Stat)	6	747	748.7	0.41	0.00053	0.00053	0.00065
Power Law	BAO + JLA (Sys)	6	747	705.0	0.82	0.0037	0.0037	0.0052
Power Law	BAO + Union2.1 (Stat)	4	587	590.1	0.41	0.00022	0.00022	0.00021
Power Law	BAO + Union2.1 (Sys)	4	587	567.9	0.67	0.0028	0.0028	0.0026
$R_{\rm h} = ct$	JLA (Stat)	4	740	855.8	0.0014	3.2×10^{-29}	3.2×10^{-28}	1.0×10^{-28}
$R_{\rm h} = ct$	JLA (Sys)	4	740	721.3	0.64	1.2×10^{-8}	1.1×10^{-7}	2.0×10^{-8}
$R_{\rm h} = ct$	Union2.1 (Stat)	2	580	656.7	0.013	8.3×10^{-21}	7.2×10^{-20}	2.3×10^{-20}
$R_{\rm h} = ct$	Union2.1 (Sys)	2	580	565.7	0.63	9.2×10^{-5}	0.00081	0.00013
$R_{\rm h} = ct$	BAO	1	7	18.3	0.0056	0.21	0.069	0.42
$R_{\rm h} = ct$	BAO + JLA (Stat)	5	747	874.1	0.00055	8.3×10^{-31}	8.3×10^{-30}	1.9×10^{-30}
$R_{\rm h} = ct$	BAO + JLA (Sys)	5	747	739.6	0.52	3.1×10^{-10}	3.0×10^{-9}	5.1×10^{-10}
$R_{\rm h} = ct$	BAO + Union2.1 (Stat)	3	587	675.0	0.0053	2.2×10^{-22}	2.0×10^{-21}	4.9×10^{-22}
$R_{\rm h} = ct$	BAO + Union2.1 (Sys)	3	587	584.0	0.49	2.5×10^{-6}	2.2×10^{-5}	4.1×10^{-6}

Table 5.3: Results of the model comparison. For each of the models and data combinations, we list the number of parameters k that were varied, the total number of data points N, the best-fit $\chi^2_{\rm min}$, the probability $P(\chi^2_{\rm min}, \nu)$ that a greater $\chi^2_{\rm min}$ could occur due to chance alone for degrees of freedom $\nu = N - k$, and the likelihood of the model relative to ΛCDM for the AICc, BIC, and Bayes factor model comparison statistics.

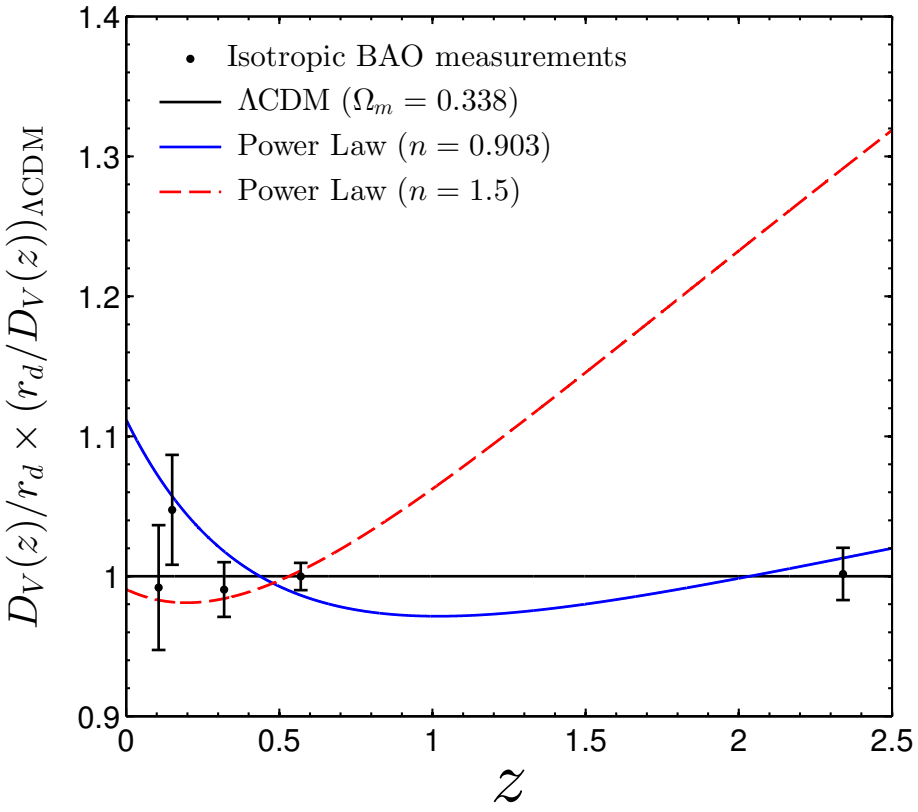

Figure 5.1: Fits to an isotropic-only version of the BAO data (black points), where we use the direct isotropic measurement from BOSS CMASS ($z = 0.57$) and an isotropic measurement derived from the LyαF anisotropic measurements ($z = 2.34$). We show the best fit to this modified BAO set for ΛCDM with Ω_m and r_d varied (solid black), power law cosmology with n and r_d varied (solid blue), and power law cosmology with $n = 1.5$ and only r_d varied (dashed red), where the value $n = 1.5$ is roughly the value required to fit the SN Ia data.

As we will see below, the uncalibrated galaxy BAO distances (our set without the LyαF BAO) are not effective in distinguishing between the expansion models we consider here. Although the galaxy BAO measurements are more mature and their systematics have been more thoroughly studied, there is no obvious reason why we should ignore the LyαF measurements. The original analyses [14, 148] investigate some important systematic effects, and they find no substantial evidence that contamination from these systematics is large. They also show that the measurements are generally robust to variations in the fiducial analysis pipeline. We therefore use the full set of BAO measurements, including the high-redshift LyαF BAO, leaving open the possibility that power law or $R_\mathrm{h} = ct$ cosmology improves the fit to the anisotropic data.

Interestingly, power law cosmology is about as good a fit to the SN and BAO data separately as ΛCDM. If systematic errors in the SN data are ignored, ΛCDM is preferred,

but when the systematics are included, the preference for ΛCDM nearly disappears. Here the AICc and BIC statistics give identical results simply because ΛCDM and power law cosmology both have one free model parameter. Power law expansion is actually a better fit to the BAO data, though the model comparison statistics indicate only a mild preference for power law expansion. The Bayes factor, which considers the likelihood averaged over the respective parameter spaces, is particularly indifferent.

The story changes when SN and BAO data are combined, however, and here ΛCDM is strongly favored by the data. As Table 5.2 suggests, the power law exponent preferred by SN data ($n \simeq 1.5$) is much higher than that preferred by BAO data ($n = 0.93$), and this tension means that the combination strongly disfavors power law cosmology relative to ΛCDM, even though power law expansion is still a good fit overall. The relative probability that power law cosmology is the "correct" model is at most $0.0052 \simeq 1/200$, which occurs for the Bayes factor when the JLA SN compilation is used with systematic errors included in the analysis.

One might wonder whether the low power law exponent ($n = 0.93$) preferred by the BAO data is due to some effect specific to the anisotropic measurements and the extra degree of freedom they probe. To investigate this, and to visualize the fit to the BAO data, we plot an isotropic-only version of the BAO data in Fig. 5.1. Here we have used the direct isotropic measurement from BOSS DR11 CMASS [13], $D_V(0.57)/r_d = 13.773 \pm 0.134$, and an isotropic measurement we derived from the LyαF anisotropic measurements, $D_V(2.34)/r_d = 30.543 \pm 0.570$, where we have propagated the errors and accounted for their correlation. Note that, while the direct isotropic measurement from CMASS is in excellent agreement with a measurement inferred in this way, the result is approximately valid only if systematic errors in the anisotropic measurements are negligible compared to the statistical errors. Obviously there is reason to worry that this is *not* the case for the LyαF BAO, so our fiducial analysis uses the anisotropic measurements directly, as recommended in the original analyses.

This issue aside, it is clear from Fig. 5.1 that the preference for a low power law exponent is not some artifact of the anisotropic measurements. Here we show fits to the isotropic-only BAO data for both ΛCDM and power law cosmology. Power law cosmology is a slightly worse fit than in the fiducial analysis, with $\chi^2_{\text{min}} = 7.03$ (a probability of 0.071 for three degrees of freedom). ΛCDM is a good fit now that the tension from the anisotropic LyαF measurements has effectively canceled, with $\chi^2_{\text{min}} = 1.65$ (a probability of 0.65 for three degrees of freedom). We also plot a power law model with the exponent fixed to the value $n = 1.5$, roughly the value required by the SN Ia data, adjusting only the sound horizon r_d to give the best fit. Since we have assumed the same detection signifi-

cances (6σ for CMASS and 4σ for LyαF) as in the fiducial analysis, it is no surprise that a smaller value for the sound horizon, which raises the model relative to the data, is preferred. Such a model fits the low-redshift BAO data nicely but misses the LyαF measurement completely. Increasing the detection significance of the LyαF measurement would make this discrepancy with the SN Ia data even more significant, and we believe that our choice here of 4σ (effectively less when using the χ^2 table for the anisotropic measurements) for the combined auto-correlation and cross-correlation measurement is conservative.

Focusing separately on the $R_\mathrm{h} = ct$ universe, we find that it is conclusively disfavored relative to ΛCDM for all data combinations that include SN Ia data, with at most a relative probability of $0.00081 \simeq 1/1200$, which occurs for BIC when the Union2.1 SN compilation is used without BAO data and with systematic errors included. If systematic errors in the SN data are ignored, the $R_\mathrm{h} = ct$ universe is a poor fit to the data (for JLA, the fit probability of 0.0014 corresponds to a $> 3\sigma$ discrepancy). The $R_\mathrm{h} = ct$ universe is also a poor fit to the BAO data alone and, despite the fact that $R_\mathrm{h} = ct$ benefits from having one less free parameter, ΛCDM is slightly preferred by the model comparison statistics. Note that here, with N very small, we do not expect the BIC result to be valid, and indeed we find that the AICc statistic, with its correction term for finite sample size, is closer to the Bayes factor result.

Figure 5.2 illustrates the ΛCDM and $R_\mathrm{h} = ct$ fits to the JLA SN data, which we have binned in redshift by averaging the distance moduli with inverse-covariance weights. There are two sets of data points because the SN data were standardized separately for each model, with $\mathcal{M}$, ΔM, α, and β optimized to produce the best fit. While ΛCDM is clearly a good fit with or without systematic errors included, it is apparent by eye that $R_\mathrm{h} = ct$ is a poor fit with statistical errors only. While the overall fit looks reasonable when systematic errors are included, there is a clear trend in the residuals, with nearby SNe too bright and distant SNe too dim.

5.6 Discussion

In this analysis, we have used goodness-of-fit and model comparison statistics to test power law and $R_\mathrm{h} = ct$ cosmology against ΛCDM. Before we summarize our conclusions, we discuss some arguments made by proponents of the $R_\mathrm{h} = ct$ universe [138–140], particularly those about hidden model dependence in the SN Ia data.

As mentioned in Sec. 5.1, the authors of [138] criticize the analysis of [137], pointing out that the conclusions are based heavily on visual inspection of plots of reconstructed dynamical quantities (e.g. derivatives of the Hubble parameter). While there is nothing

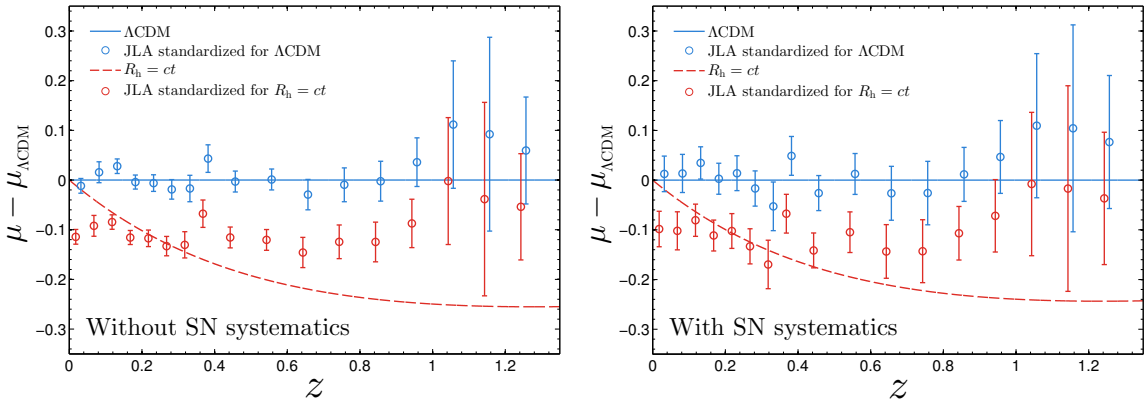

Figure 5.2: Hubble diagram for the JLA SN compilation, where the measured distance moduli have been standardized separately for ΛCDM (blue points) and the $R_h = ct$ cosmology (red points). The best-fit ($\Omega_m = 0.29$) ΛCDM model (solid blue) is plotted along with the $R_h = ct$ model (dashed red). We show the SN data without (left panel) and with (right panel) systematic errors included. The distance moduli are binned in redshift with inverse-covariance weights.

wrong with a dynamical approach, one would like a way to quantify the preference of the data. Here we have used direct model comparison to quantify the relative likelihoods of the alternative models, appropriately accounting for differences in model complexity. Note that a similar approach is used in [140].

One of the concerns [139] about the SN Ia data is that the standardization of the SNe is model-dependent, in the sense that the parameters α, β, $\mathcal{M}$, and ΔM have been determined assuming ΛCDM (or a ΛCDM-like model). This is a valid point in general, but only if one analyzes distance moduli that have been pre-corrected for stretch, color, and host-mass correlations. Fixing the SN Ia absolute magnitude and Hubble constant (thus fixing $\mathcal{M}$) would be even worse. In this analysis, we have used the public JLA data to vary all of the nuisance parameters simultaneously with any cosmological parameters ([140] does something similar using an older version of the SNLS data). It is worth noting that, aside from adjusting the overall offset in the Hubble diagram $\mathcal{M}$, allowing the other parameters to vary has a rather small effect. This is hinted at in Table 5.2, where the best-fit values for α, β, and even ΔM are similar for the different models and regardless of whether systematic errors are included. This is because these correlations, which have now been well-established, primarily serve to reduce the intrinsic scatter in the Hubble diagram. Only if there is, for instance, a trend where the *fraction* of SNe with high-stretch light curves changes significantly with redshift would the choice of model affect the value of α significantly. Note that the SN analyses do consider possible evolution of α and β and account for this by adding systematic error.

The authors of [140] go further and argue that, because the intrinsic scatter is determined by adjusting its value until the reduced χ^2 of the fit is equal to one, the intrinsic scatter estimate is model-dependent. This concern is actually addressed in Section 5.5 of the JLA analysis [145], which explains that one can avoid this problem by estimating the intrinsic scatter in redshift bins, essentially relying on the fact that the SNe are so constraining, and the redshift coverage so complete, that no parametric model needs to be used at all. In other words, the scatter around the mean in a redshift bin gives the intrinsic scatter for that bin directly. Although [145] finds an apparent trend where the estimated intrinsic scatter decreases with increasing redshift, the values are consistent with a constant, and ultimately a separate value is chosen for each of the four main subsamples, effectively allowing for survey-dependent misestimates of other statistical errors. We point out that the approach used in [140], where σ_{int} is constrained along with the other parameters, results in nearly identical determinations of the intrinsic scatter whether assuming ΛCDM ($\sigma_{\text{int}} = 0.103 \pm 0.010$) or $R_{\text{h}} = ct$ ($\sigma_{\text{int}} = 0.106 \pm 0.010$), indicating that even if the model matters in general, it does not in their case.

Why does [140] come to a different conclusion (that $R_{\text{h}} = ct$ is modestly favored over ΛCDM) than the present analysis, where similar SN Ia data is used? Presumably the reason is that [140] uses *only* the SNLS SNe, leaving out the low-redshift samples, the mid-redshift SDSS SNe, and the high-redshift SNe from the Hubble Space Telescope, without any real justification. This of course removes much of the discriminating power of the SN data. In Fig. 5.2, notice that only considering the data points in the range $0.4 < z < 1$, which roughly corresponds to the redshift range dominated by the SNLS SNe, would make $R_{\text{h}} = ct$ a great fit after the overall height of the data points ($\mathcal{M}$) is adjusted. Even the trend in these residuals (presumably due to their statistical correlation) aligns with the $R_{\text{h}} = ct$ expansion. While it is true that combining observations of SNe from different instruments into one Hubble diagram is challenging and can lead to concerns about residual systematic effects, the most important systematic errors (e.g. photometric calibration) are quantified in current analyses. For some reason, despite their apparent worry about unaccounted-for systematic effects, the authors of [140] ignore the *known* systematic errors altogether, a common trend in the literature that is usually unjustified and will lead to false conclusions. Here, for instance, systematic errors substantially weaken the model-discriminating power of the SN data; in fact, it is these systematic errors that allow the $R_{\text{h}} = ct$ universe to be an acceptable overall fit, even if it is conclusively disfavored by the model comparison.

These concerns notwithstanding, we are confident in our conclusions, which we summarize as follows. Given the tension in the BAO data resulting from the anisotropic LyαF measurements, we find that power law cosmology is a slightly better model than ΛCDM

for BAO data alone and is only slightly disfavored relative to ΛCDM for SN Ia data alone. When SN and BAO data are combined, the different power law exponents preferred by each create substantial tension such that ΛCDM is strongly preferred by the model comparison statistics (Table 5.3). While the strength of this preference depends on the detection significance of the BOSS LyαF measurement, our choice here (see Sec. 5.3.2) is conservative. Also, while the preference for a low power law exponent ($n \simeq 0.9$) is due to the LyαF BAO, it is not due to any subtlety in the anisotropic measurements (see Fig. 5.1 and the discussion in Sec. 5.5). In order to reconcile the power law exponent from BAO with the higher value ($n \simeq 1.5$) required by SN Ia data, an unaccounted-for systematic affecting the anisotropic LyαF measurements must avoid cancellation in the isotropic measurement, shifting the value by several times its current error. Hopefully, new data (e.g. BOSS DR12) will soon improve these high-redshift BAO measurements, which are clearly important for distinguishing between alternative models for expansion, including those considered here.

We have also found that the $R_{\rm h} = ct$ cosmology is nearly ruled out when systematic errors in the SN Ia data are ignored (for JLA, the fit is unlikely at a level of $> 3\sigma$). With systematic errors included, the overall fit is acceptable, but ΛCDM is conclusively the better model. The BAO data separately favor ΛCDM, though only slightly, and combining SN and BAO data simply strengthens these conclusions.

CHAPTER 6

Peculiar Velocities of SNe Ia

6.1 Introduction

Motions of objects in the universe are not entirely random. Objects which are physically close to one another respond similarly to the pull of large-scale structure, and as a result their peculiar velocities are correlated. Correlations between galaxy peculiar velocities are an old subject [159–165], and these velocities have already been used to constrain cosmological models, in particular the amount of matter in the universe (see [166] for a review). More recently, peculiar velocities have become important in the analysis of type Ia supernova (SN Ia) data. At low redshift ($z \lesssim 0.05$), typical peculiar velocities of $\sim$300 km/s are a significant contribution to the SN redshift (for instance, $cz = 3{,}000$ km/s at $z = 0.01$). These peculiar velocities are a nuisance if one is interested in using the SNe to constrain expansion history and dark energy, and it is common practice to propagate this extra dispersion into the error budget (e.g. add 300 km/s $\times\, 5/(cz \ln 10)$ in quadrature to the statistical uncertainty of each SN magnitude). However, this neglects significant covariance between the velocities of different SNe.

Alternatively, one can consider the SN peculiar velocity field itself to be a signal, one that should contain useful information about the amount and distribution of matter in the universe. Nearby SNe are much fewer in number than nearby galaxies, and given the volume limitation for both, this will likely still be the case in the future. On the other hand, SNe are more useful on a per-object basis because their individual distances can be inferred directly and with relative precision — roughly 7% for each SN, depending on the quality of the observations. Therefore, there has been a resurgence of interest in how SN peculiar velocities are modeled and used [167, 168].

In this paper, we perform a careful study of the SN velocity correlations in current data, in particular the way in which they are used to draw conclusions about the so-called "bulk velocity" — the motion, relative to the cosmic microwave background (CMB) rest frame,

of the patch of the universe centered on us and containing the nearby sample. Though we focus on SNe, our methodology is not restricted to SNe and equally applies to analysis of galaxy peculiar velocities.

The paper is organized as follows. In section 6.2, we review the physics of how peculiar velocities affect SN magnitudes. In section 6.3, we describe the SN samples and how we use them. In section 6.4, we define a general likelihood that is the basis for our analyses, which include a test for the presence of velocity correlations (section 6.5), a test for the presence of excess bulk velocity beyond that encoded in the correlations predicted in ΛCDM (section 6.6), and a comparison to previous work that studied bulk flows without the velocity covariance (section 6.7). We summarize our conclusions in section 6.8.

6.2 Theoretical framework

6.2.1 Magnification and SN magnitude residuals at low redshifts

The magnitude residuals of standard candles like SNe Ia are directly related to the magnification μ, which is defined as the fractional perturbation in the angular diameter and luminosity distances (see [167, 169]),

$$-\frac{1}{2}\,\mu = \frac{\Delta d_L}{\bar{d}_L(z)} = \frac{\Delta d_A}{\bar{d}_A(z)}\,, \tag{6.1}$$

where $\bar{d}_A(z)$ and $\bar{d}_L(z)$ denote the background distances evaluated at the observed redshift z. The second equality, relating luminosity and angular diameter distances, follows from the conservation of the photon phase space density. That is, μ describes both the change in the apparent angular size of a spatial ruler as well as the change in observed flux of a standard candle.

Covariant expressions for the magnification at linear order in cosmological perturbations have been given in [169–172]. In the conformal-Newtonian (cN) gauge, where the metric is written as

$$ds^2 = a^2(\tau)\left[-(1+2\Psi)\,d\tau^2 + (1+2\Phi)\,\delta_{ij}\,dx^i dx^j\right]\,, \tag{6.2}$$

the magnification is given, in the notation of [172], by[1]

$$\mu = \left[-2 + \frac{2}{aH\tilde{\chi}}\right] \Delta \ln a - 2\Phi + 2\kappa - 2v_{\parallel o} - \frac{2}{\tilde{\chi}} \int_0^{\tilde{\chi}} d\chi \, (\Psi - \Phi) \,, \tag{6.3}$$

where $\tilde{\chi} \equiv \chi(z)$ is the coordinate distance inferred using the observed redshift, and

$$\kappa = \frac{1}{2} \int_0^{\tilde{\chi}} d\chi \, \frac{\chi}{\tilde{\chi}} (\tilde{\chi} - \chi) \nabla_\perp^2 \, (\Psi - \Phi) \;, \tag{6.4}$$

$$\Delta \ln a = \Psi_o - \Psi + v_\parallel - v_{\parallel o} + \int_0^{\tilde{\chi}} d\chi \, [\Phi' - \Psi'] \tag{6.5}$$

are the convergence and fractional redshift perturbation, respectively. The latter contains the gravitational redshift, Doppler shift, and integrated Sachs-Wolfe effect. Further, $\nabla_\perp^2$ denotes the Laplacian on a sphere of radius χ, $v_\parallel = v^i \hat{n}_i$ denotes the peculiar velocity projected along the line of sight $\hat{\mathbf{n}}$, integrals over χ denote integrals along the past lightcone, and a subscript o denotes a quantity evaluated at the location of the observer. Note that κ, $\Delta \ln a$, and any other terms appearing in eq. (6.3) are coordinate-dependent quantities, and only the combination given in eq. (6.3) corresponds to an actual (gauge-invariant) observable. This can be verified by considering gauge transformations and various test cases [172, 173].

For low-redshift SNe, where $z \ll 1$ so that $\tilde{\chi} \ll 1/(aH)$, the terms involving the velocity are the most significant. This is because the lensing convergence is suppressed for small source distances and because the scales probed are much smaller than the horizon. Then, the terms involving the potentials Φ and Ψ are also suppressed by roughly $aH\tilde{\chi}$ relative to the velocity. In this case, we obtain

$$\mu \overset{z \ll 1}{=} \frac{2}{aH\tilde{\chi}} \left(v_\parallel - v_{\parallel o}\right) \;. \tag{6.6}$$

This expression for the magnification, proportional to the relative velocity along the line of sight between source and observer, simply arises due to the fact that we evaluate the luminosity distance to a supernova using the background distance-redshift relation, while the actual redshift is perturbed by the Doppler shift. One can easily verify numerically that this approximation is better than 1% for $z \lesssim 0.1$, which is the redshift range we will consider in this paper. Note that [167] includes the term -2 in the $\Delta \ln a$ prefactor in eq. (6.3); however, this is not strictly consistent, since the terms involving Ψ in $\Delta \ln a$, as

[1] Here, we have neglected a term that is present if the luminosity of the standard candle depends on time; in any case, it is subdominant in the limit we will consider. We have also neglected two pure monopole contributions, motivated by the discussion in section 6.2.2.

well as the aberration term $-2v_{\parallel o}$ in eq. (6.3) are of comparable magnitude to this correction (see also [174]). We will thus work with eq. (6.6) as the proper low-z limit of eq. (6.3). Note that this relation remains valid even if μ becomes of order unity, as long as the velocities $v_\parallel$ remain small compared to the speed of light. On very small scales ($z < 0.01$), the velocities are no longer described accurately by linear perturbation theory. However, since the SN samples considered here are restricted to $z \gtrsim 0.01$, we will work with velocities derived from linear perturbation theory. Note that, in principle, nonlinear corrections to the velocity could also be relevant for higher-redshift SNe, if two SNe happen to be physically close. However, we have verified that nonlinear corrections to the velocities have a small effect (see below).

As eq. (6.6) shows, the relevant quantity for the magnification at low z is the relative velocity between the source and the observer projected along the line of sight. This also includes small-scale motions such as the velocity of the Solar System with respect to the Milky Way center, which are uncorrelated with large-scale cosmological velocity fields. For this reason, we correct the observed SN redshifts to the CMB rest frame using the measured CMB dipole moment (see section 6.3). Then, the magnification becomes

$$\mu|_{z_{\rm CMB}} = \frac{2}{aH\tilde{\chi}} \left(v_\parallel - v_{\parallel,\rm CMB}\right) , \tag{6.7}$$

where the relevant quantity is now the velocity of the SN relative to the CMB rest frame. This simplifies the interpretation, since $v_\parallel - v_{\parallel,\rm CMB}$ is well described by linear perturbation theory. In fact, by performing the calculation in the CMB rest frame (as is normally done), we can set $\mathbf{v}_{\rm CMB} = 0$. The following relations will always assume that we work with CMB-frame redshifts and in the CMB rest frame.

It is straightforward to convert a perturbation in the luminosity distance (as in eq. (6.1)) into a perturbation of the SN magnitude from the homogeneous background value:

$$\delta m = -\frac{5}{2\ln 10}\,\mu \overset{z\ll 1}{=} -\frac{5}{\ln 10}\,\frac{\mathbf{v}\cdot\hat{\mathbf{n}}}{aH\tilde{\chi}} . \tag{6.8}$$

Note that this relation assumes that $\mu \ll 1$ and is thus not applicable at very low redshifts. While it is straightforward to derive the proper nonlinear relation for δm, this is not necessary for our purposes, since $z \gtrsim 0.01$ in our SN samples.

Now consider one object at redshift z_i in direction $\hat{\mathbf{n}}_i$ on the sky, and a second at $(z_j, \hat{\mathbf{n}}_j)$.

We can derive the covariance of their residuals,

$$S_{ij} \equiv \langle \delta m_i \, \delta m_j \rangle = \left[\frac{5}{\ln 10} \right]^2 \frac{a_i}{a_i' \chi_i} \frac{a_j}{a_j' \chi_j} \, \xi_{ij}$$
$$= \left[\frac{5}{\ln 10} \right]^2 \frac{(1+z_i)^2}{H(z_i) d_L(z_i)} \frac{(1+z_j)^2}{H(z_j) d_L(z_j)} \, \xi_{ij} \,, \tag{6.9}$$

where ξ_{ij} is the velocity covariance given by

$$\xi_{ij} \equiv \xi_{ij}^{\rm vel} \equiv \langle (\mathbf{v}_i \cdot \hat{\mathbf{n}}_i)(\mathbf{v}_j \cdot \hat{\mathbf{n}}_j) \rangle$$
$$= \frac{dD_i}{d\tau} \frac{dD_j}{d\tau} \int \frac{dk}{2\pi^2} P(k, a=1) \sum_\ell (2\ell+1) j_\ell'(k\chi_i) j_\ell'(k\chi_j) P_\ell(\hat{\mathbf{n}}_i \cdot \hat{\mathbf{n}}_j) \,. \tag{6.10}$$

Here, primes denote derivatives of the Bessel functions with respect to their arguments, τ is the conformal time, $d\tau = dt/(a^2 H)$, D_i is the linear growth function evaluated at redshift z_i, and $\chi_i = \chi(z_i)$. The power spectrum $P(k, a)$ is evaluated in the present ($a = 1$) and, at the large scales we are interested in, only the first $\simeq 10$ terms in the sum over the multipoles contribute. As mentioned above, we use velocities derived from linear theory and thus insert the linear matter power spectrum for our numerical results. We have verified that using a prescription for the nonlinear matter power spectrum in eq. (6.10) does not significantly affect our results. We thus conclude that the linear treatment is sufficient for our purposes. Physically, this is because the dominant contribution to the covariance comes from fairly large-scale modes. Note that in our approach, $\langle (\delta m_i)^2 \rangle$ is assumed to capture the random motion contribution to the variance of SN residuals.[2] While this is not expected to be completely accurate when using the linear matter power spectrum, the difference in the diagonal covariance elements is not very significant.[3]

We have denoted this covariance matrix $\mathbf{S}$ to emphasize that this is a cosmologically guaranteed "signal" to be added to the "noise" covariance matrix that accounts for the combination of statistical and systematic errors that affects SN distance measurements, such as intrinsic variations in the SN luminosity (see section 6.3). We again point out that the two geometric prefactors in eq. (6.9) each differ by an additive factor of 1 relative to those in [167] because we drop the term -2 in eq. (6.3) in order to achieve a consistent low-

[2] An alternative approach by [175] models velocities with perturbation theory based on a density field derived from other surveys, and complements them with a "thermal" component of $\sim$150 km/s added in quadrature to account for nonlinearities. In contrast to our approach, this thus relies on external data sets. A detailed comparison between the covariances obtained using these different approaches would be interesting but is beyond the scope of this paper.

[3] For the low-redshift SNe we consider, nearly all of the redshifts are derived from host galaxy spectra, and so the motion of the SN within its host does not contribute to the residuals.

redshift expansion; we have checked that all neglected terms would contribute negligibly at $z \lesssim 0.1$.

6.2.2 Monopole subtraction

The magnification eq. (6.1) and its low-redshift version eq. (6.6) still have a monopole component, that is, a contribution that is uniform on the sky. However, since the SN magnitude residuals are defined with respect to the best-fit distance-redshift relation, this monopole is mostly absorbed in the fit. While there could technically be a residual monopole signal due to the fact that our fit (to a flat ΛCDM model, see section 6.4) is very restricted, we will assume here that the bulk of the monopole is removed. Thus, eq. (6.9) needs to be corrected.

To this end, we define the mean magnitude residual at redshift i as

$$\overline{\delta m}(z_i) = \int \delta m(z_i, \hat{\mathbf{n}})\, W(\hat{\mathbf{n}})\, d^2\hat{\mathbf{n}}\,, \tag{6.11}$$

where $W(\hat{\mathbf{n}})$ is the survey window function, which is normalized such that $\int W(\hat{\mathbf{n}})\, d^2\hat{\mathbf{n}} = 1$. Then, noting that we actually measure $\widehat{\delta m}_i = \delta m_i - \overline{\delta m}(z_i)$, the proper covariance is

$$S_{ij} \equiv \left\langle \widehat{\delta m}_i\, \widehat{\delta m}_j \right\rangle = \left\langle \left[\delta m(z_i, \hat{\mathbf{n}}_i) - \overline{\delta m}(z_i)\right] \left[\delta m(z_j, \hat{\mathbf{n}}_j) - \overline{\delta m}(z_j)\right] \right\rangle\,, \tag{6.12}$$

which can be worked out to be

$$\begin{aligned} S_{ij} = &\left[\frac{5}{\ln 10}\right]^2 \frac{(1+z_i)^2}{H(z_i) d_L(z_i)} \frac{(1+z_j)^2}{H(z_j) d_L(z_j)} \frac{dD_i}{d\tau} \frac{dD_j}{d\tau} \int \frac{dk}{2\pi^2}\, P(k, a=1) \\ &\times \sum_\ell (2\ell+1) j'_\ell(k\chi_i) j'_\ell(k\chi_j) \left[P_\ell(\hat{\mathbf{n}}_i \cdot \hat{\mathbf{n}}_j) - \frac{4\pi}{2\ell+1} \left[w_\ell(\hat{\mathbf{n}}_i) + w_\ell(\hat{\mathbf{n}}_j)\right] + 4\pi W_\ell \right], \end{aligned} \tag{6.13}$$

where the survey footprint has been expanded in spherical harmonics,

$$W(\hat{\mathbf{n}}) = \sum_{\ell m} w_{\ell m} Y_{\ell m}(\hat{\mathbf{n}})\,, \tag{6.14}$$

and the coefficients $w_\ell(\hat{\mathbf{n}}_i)$ and W_ℓ are defined as

$$w_\ell(\hat{\mathbf{n}}) \equiv \sum_m w_{\ell m} Y_{\ell m}(\hat{\mathbf{n}})\,, \qquad W_\ell \equiv \frac{\sum_m |w_{\ell m}|^2}{2\ell+1}\,. \tag{6.15}$$

The extra terms in the square brackets in eq. (6.13) are corrections due to the survey window. The W_ℓ are therefore just the angular power spectrum (more precisely, the "pseudo-C_ℓ") of the map, while $w_\ell(\hat{\mathbf{n}})$ is the ℓ portion of the survey mask at an arbitrary location. Note that, due to the required normalization of W, its value where the survey observes is not unity, but rather

$$W(\hat{\mathbf{n}}) = \begin{cases} \dfrac{1}{\Omega_{\text{sky}}} & \text{(observed sky)} \\ 0 & \text{(unobserved sky).} \end{cases} \tag{6.16}$$

The term in the square parentheses in the last line of eq. (6.13), which includes the subtraction of the mean, is therefore a new result that has not, to our knowledge, been derived and included in previous analyses (although the existence of such a term has been pointed out in [167, 174]). For a full-sky window, it is easy to show that this term becomes $P_\ell(\hat{\mathbf{n}}_i \cdot \hat{\mathbf{n}}_j) - 1$ for $\ell = 0$ and remains equal to the original expression $P_\ell(\hat{\mathbf{n}}_i \cdot \hat{\mathbf{n}}_j)$ for the other multipoles.

We find that the monopole-subtracted formula leads to small but noticeable changes in the results, such as the constraints on the parameter A in section 6.5, and we recommend that it be used in future analyses.

6.3 SN Ia data and noise covariance

For our primary SN Ia dataset, we use the joint light-curve analysis (JLA) [145] of SNe from the Supernova Legacy Survey (SNLS) and the Sloan Digital Sky Survey (SDSS). JLA includes a recalibration of SNe from the first three years of SNLS [17, 75] along with the complete SN sample from SDSS, making it the largest combined SN analysis to date. The final compilation includes 740 SNe, $\sim$100 low-redshift SNe from several subsamples, $\sim$350 from SDSS at low to intermediate redshifts, $\sim$250 from SNLS at intermediate to high redshifts, and $\sim$10 high-redshift SNe observed with the Hubble Space Telescope.

We combine the individual covariance matrix terms provided[4] to compute the full covariance matrix, which includes statistical errors (correlated uncertainties in the light-curve measurements, intrinsic scatter, lensing dispersion) and a variety of systematic errors (photometric calibration, uncertainty in the bias correction, light-curve model uncertainty, potential non-Ia contamination, uncertainty in the Milky Way dust extinction correction, and uncertainty in the host galaxy correction).

Although we compute the covariance matrix as described in the JLA analysis, we leave out two contributions to the total error. First, we leave out the additional scatter of

[4] http://supernovae.in2p3.fr/sdss_snls_jla/

150 km/s $\times 5/(cz \ln 10)$ added in quadrature to the other statistical errors on the diagonal to account for peculiar velocity. This peculiar velocity scatter does not apply because peculiar velocities are not a source of noise in our analysis; instead, they are modeled by the formalism discussed in section 6.2. We also leave out the systematic error term corresponding to uncertainty in the peculiar velocity *correction* applied to the low-z JLA redshifts. Since our aim is to study the peculiar velocities themselves, we want to avoid this correction and then leave out the systematic error associated with it. To this end, we obtain the CMB-frame redshifts z_{CMB} directly from the measured heliocentric redshifts z_{hel}. Specifically, for each SN we compute

$$1 + z_{\text{CMB}} = (1 + z_{\text{hel}}) \left[1 + \frac{v_{\text{CMB}}}{c} \left(\hat{\mathbf{n}}_{\text{CMB}} \cdot \hat{\mathbf{n}} \right) \right] , \tag{6.17}$$

where $\hat{\mathbf{n}}$ is the sky position of the SN, $\hat{\mathbf{n}}_{\text{CMB}}$ is the CMB dipole direction, and v_{CMB} is the velocity of the Solar System barycenter relative to the CMB rest frame implied by the dipole amplitude. We use the measured values $v_{\text{CMB}} = 369$ km/s and $\hat{\mathbf{n}}_{\text{CMB}} \equiv (l, b) = (263.99^\circ, 48.26^\circ)$, where the quoted uncertainties [176] are negligible for our purposes.

For comparison, we separately consider the Union2 SN Ia analysis [24] from the Supernova Cosmology Project.[5] We use the full covariance matrix provided for the Union2 SN magnitudes, but as with JLA, we remove the peculiar velocity scatter (300 km/s here) that was added to the diagonal. The redshifts given for the Union2 SNe are just the heliocentric redshifts transformed to the CMB rest frame, so we use them directly.

Note that the Union2 compilation of 557 SNe has been superseded by the Union2.1 compilation [25] of 580 SNe, but here the goal is a fair comparison to previous work that analyzes the Union2 data. Since the primary change in Union2.1 is the addition of a set of high-redshift SNe, and since only low-redshift SNe are relevant for our analysis, we would expect the two compilations to produce very similar results. When substituting Union2.1 for Union2, our results do not change qualitatively, but there are some minor differences due to new estimates for some corrected SN magnitudes and their errors. Union2.1 also includes a host-mass correction (see below) that Union2 does not, but this is relatively small and only accounts for part of the magnitude differences.

Finally, we briefly consider the low-z compilation from the older analysis of [177], also for comparison with other work. This compilation does not include an analysis of systematic errors, so the uncertainty in a SN magnitude is just a combination of the light-curve measurement errors and the derived intrinsic scatter of $\sigma_{\text{int}} = 0.08$ mag. Again, we do not include the peculiar velocity scatter of 300 km/s prescribed for a cosmological analysis. Although CMB-frame redshifts are given, we transform the given heliocentric

[5] http://supernova.lbl.gov/Union/

redshifts into CMB-frame redshifts ourselves using eq. (6.17).

Because SNe Ia are not perfect standard candles, it is necessary to correct the observed peak magnitude of each SN for the empirical correlations between the SN Ia absolute magnitude and both the stretch (broadness) and color measure associated with the light-curve fitter. More recently, it has become common to fit for a constant offset in the absolute magnitude for SNe in high-stellar-mass host galaxies. For JLA, the corrected magnitude is therefore given by

$$m^{\text{corr}} = m + \alpha \times (\text{stretch}) - \beta \times (\text{color}) + P\,\Delta M, \tag{6.18}$$

where α, β, and ΔM are nuisance parameters describing, respectively, the stretch, color, and host-mass corrections. The measured $P \equiv P(M_* > 10^{10} M_\odot)$ is the probability that the SN occurred in a high-stellar-mass host galaxy. Note that, as mentioned above, Union2 does not include this host-mass correction; also, the analysis of [177] uses a different light-curve fitter with different (but related) light-curve corrections.

For each of the three datasets, we fix the SN Ia nuisance parameters to their best-fit values from a fit to the Hubble diagram (for JLA, we perform this fit and correct the magnitudes ourselves; for the other datasets, we use precorrected magnitudes). In a proper cosmological analysis, one should vary the SN nuisance parameters simultaneously with any cosmological parameters. In practice, however, the nuisance parameters are well-constrained by the Hubble diagram with little dependence on the cosmological model, so holding them fixed should be a good approximation, especially for our purposes here.

6.4 Likelihood

We write the full covariance $\mathbf{C}$ as the sum of two contributions, $\mathbf{C} = \mathbf{S} + \mathbf{N}$, where $\mathbf{S}$ is the signal covariance, dominated by velocities at low z and discussed in section 6.2, and $\mathbf{N}$ is the noise covariance, described in section 6.3.

Assuming a given cosmological model that allows us to calculate $\mathbf{S}$ (eq. (6.9)), the *optimal* way to determine whether the data favors peculiar velocities is to consider evidence for the detection of the full signal matrix $\mathbf{S}$. This approach uses more information in the data than the search for any particular moment, such as the dipole, of the peculiar velocity field.

Here we would like to detect evidence for coherent departures of supernova magnitudes from the mean — that is, clustering. To do this, we introduce a new dimensionless parameter A and let $\mathbf{S} \to A\,\mathbf{S}$, where $A = 1$ for the fiducial model. $A = 0$ corresponds to the

case that magnitude residuals are purely due to noise and systematics in the SN Ia data. We would like to test whether A is consistent with one and different from zero. Including the new parameter A, the full covariance becomes

$$\mathbf{C} = A\,\mathbf{S} + \mathbf{N}\,, \tag{6.19}$$

where $0 \leq A < \infty$.

On the other hand, allowing for an excess bulk flow component is interesting as well, as it can be used to search for signatures beyond the fiducial ΛCDM model and also allows us to compare our results with the existing literature (see section 6.6). In this case, the magnitude residuals are affected by an additional bulk velocity $\mathbf{v}_{\text{bulk}}$ (e.g. [167]):

$$\Delta m_i^{\text{bulk}} \equiv \Delta m^{\text{bulk}}(\mathbf{v}_{\text{bulk}}; z_i, \hat{\mathbf{n}}_i) = -\left(\frac{5}{\ln 10}\right) \frac{(1+z_i)^2}{H(z_i) d_L(z_i)}\, \hat{\mathbf{n}}_i \cdot \mathbf{v}_{\text{bulk}}\,, \tag{6.20}$$

where z_i and $\hat{\mathbf{n}}_i$ are the redshift and sky position of the SN, while $\mathbf{v}_{\text{bulk}}$ is a fixed three-dimensional vector. In the quasi-Newtonian picture, $\mathbf{v}_{\text{bulk}}$ corresponds to the bulk motion of the SN sample; however, in the context of non-standard cosmological models (such as those breaking homogeneity or isotropy), this should really be seen as a convenient parametrization of the dipole of SN magnitude residuals.

Putting these ingredients together, we construct a multivariate Gaussian likelihood[6]

$$\mathcal{L}(A, \mathbf{v}_{\text{bulk}}) \propto \frac{1}{\sqrt{|\mathbf{C}|}} \exp\left[-\frac{1}{2}\mathbf{\Delta m}^{\intercal}\mathbf{C}^{-1}\mathbf{\Delta m}\right], \tag{6.21}$$

where the elements of the vector $\mathbf{\Delta m}$ are

$$(\mathbf{\Delta m})_i = m_i^{\text{corr}} - m^{\text{th}}(z_i, \mathcal{M}, \Omega_m) - \Delta m_i^{\text{bulk}}(\mathbf{v}_{\text{bulk}})\,, \tag{6.22}$$

where m_i^{corr} are the observed, corrected magnitudes and $m^{\text{th}}(z_i, \mathcal{M}, \Omega_m)$ are the theoretical predictions for the background cosmological model (see below). The $\mathcal{M}$ parameter corresponds to the (unknown) absolute calibration of SNe Ia; we analytically marginalize over it in all analyses (e.g. appendix of [2]).

We emphasize that, since the covariance depends on the parameter A that we are interested in constraining, we need to include a term for the $1/\sqrt{|\mathbf{C}|}$ prefactor in addition to the

[6]Note that SN flux, or a quantity linearly related to it, might be a better choice for the observable than the magnitude, given that we expect the error distribution of the former to be more Gaussian than the latter. Nevertheless, this choice should not impact our results, as the fractional errors in flux are not too large, and we have explicitly checked that the distribution of the observed magnitudes around the mean is approximately Gaussian. Therefore we follow most literature on the subject and work directly with magnitudes.

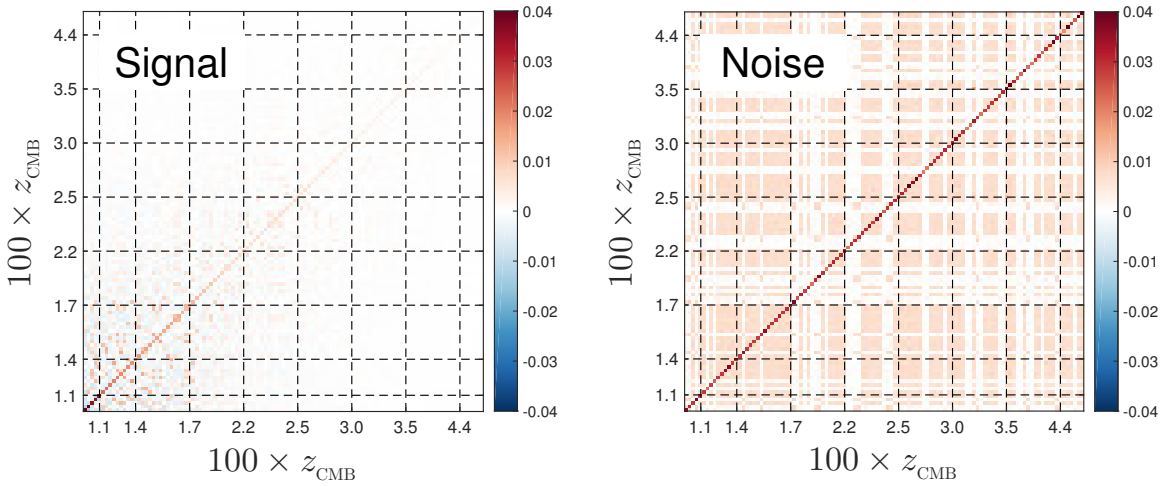

Figure 6.1: Comparison of the signal (left panel) and noise (right panel) contributions to the full covariance matrix for the 111 SNe at $z < 0.05$ from the JLA compilation.

usual χ^2 quantity. Since the covariance is a strictly increasing function of A, neglecting the prefactor would lead to the clearly erroneous result that the likelihood is a maximum for $A \to \infty$.

The likelihood in eq. (6.21) is the principal tool we will use for our analyses. In this most general form, the likelihood depends on two input quantities (four parameters, since the velocity has three components): the normalization A of the signal component of the covariance matrix and the excess bulk velocity $\mathbf{v}_{\rm bulk}$ not captured by the velocity covariance. Note that, in the fiducial model, $A = 1$ and $\mathbf{v}_{\rm bulk} = 0$.

Throughout our analyses, we assume a flat ΛCDM model ($w = -1$, $\Omega_k = 0$) with free parameters fixed to values consistent with data from *Planck* [178] and other probes. That is, we fix $\Omega_m = 0.3$, physical matter density $\Omega_m h^2 = 0.14$, physical baryon density $\Omega_b h^2 = 0.0223$, scalar spectral index $n_s = 0.965$, and amplitude of scalar fluctuations $A_s = 2.22 \times 10^{-9}$. The corresponding derived value of the Hubble constant is $h = 0.683$, and that of the amplitude of mass fluctuations is $\sigma_8 = 0.79$. Within the ΛCDM model, these parameters are determined very precisely using *Planck* data alone, and we have explicitly checked that modest changes in the cosmological model, larger than those allowed by *Planck*, have a negligible effect on our results. We can therefore conclude that adding *Planck* priors and marginalizing over these parameters would not significantly affect our constraints. This is not surprising. The background cosmology only affects the monopole of the Supernova magnitudes, and even this dependence is weak at very low redshifts (since we marginalize over $\mathcal{M}$). Only a much larger change in the parameters would affect the expected pairwise covariance, which we do not expect to be able to measure precisely in the first place.

In figure 6.1, we compare the noise covariance $\mathbf{N}$ to the signal covariance $\mathbf{S}$ for our fiducial cosmology. While the noise contribution is typically larger than the signal, the signal is not negligible, and it actually dominates for the lowest-redshift SNe. The noise, unlike the signal, becomes effectively smaller as more SNe are used in the analysis, making the signal important for the whole redshift range considered (see also the discussion in [179]).

6.5 Constraints on the amplitude of signal covariance

We first consider whether the data itself shows a preference for the presence of the velocity (signal) covariance. Therefore, we explore the constraints on A using the likelihood in eq. (6.21) and fixing $\mathbf{v}_{\text{bulk}} = 0$.

The constraints on the parameter A, which determines the fraction of the velocity covariance added to the full covariance $\mathbf{C}$, are shown in figure 6.2, with the numerical results given in table 6.1. We have adopted a uniform prior on A such that our Bayesian posterior is proportional to the likelihood in eq. (6.21). All data choices consistently use the available SNe out to $z = 0.05$. This leaves 111 objects in the JLA analysis and 132 in the Union2 analysis. We have explicitly checked that the results are insensitive to the precise redshift cutoff; they are driven by the lowest-redshift SNe, and $z < 0.05$ comfortably captures all of them.

The solid black curve shows JLA, the most current and rigorously calibrated dataset. JLA does not rule out the $A = 0$ hypothesis; in fact, the likelihood peaks near this value. Nevertheless, JLA is fully consistent with the standard value $A = 1$, with a probability of 0.07 for $A > 1$.

The solid red curve shows the result from the Union2 dataset. While it is noticeably different than the JLA result, the two likelihoods are mutually consistent; in particular, $A = 1$ is a satisfactory fit to both. Nevertheless, Union2 is different in that it strongly disfavors $A = 0$.

In order to gain additional insight into the difference between the two datasets, we have identified SNe at $z < 0.05$ that overlap between the two datasets, a total of 96 objects. Performing the analysis on this overlap (dashed lines in figure 6.2), we see that the results are in better agreement but still somewhat disagree, despite both analyses using the same SN set. Part of the reason is that JLA and Union2 determine the magnitudes differently; however, even some redshifts do not match. We find a root-mean-square (rms) redshift difference of 1.4% for the object-to-object comparison of the 96 overlapping SNe, and the largest difference is 5%. A further exploration of precisely why the SN redshifts and

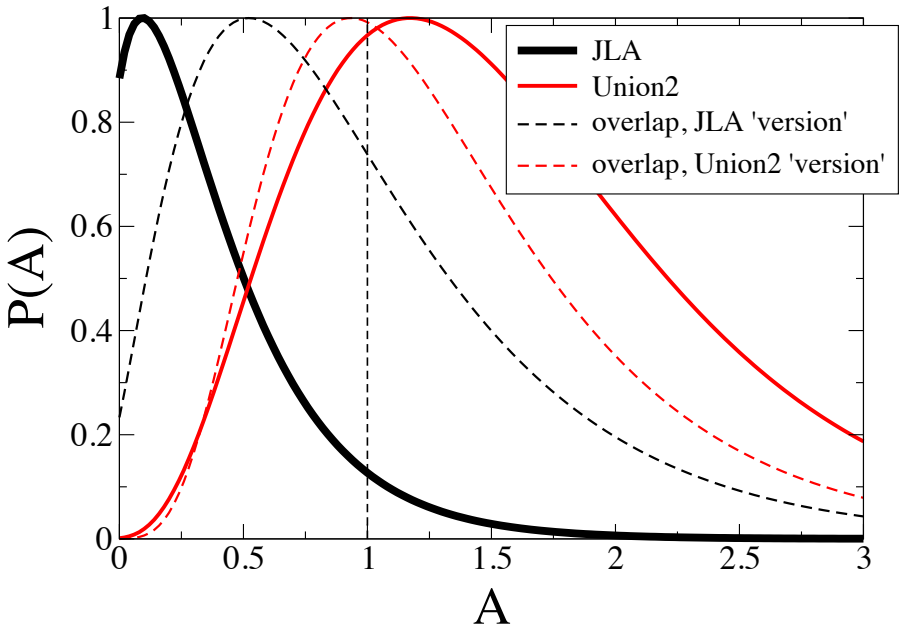

Figure 6.2: Constraints on the parameter A that quantifies the amount of velocity correlations ($A = 1$ is the standard ΛCDM value). The JLA data are consistent with $A = 1$ but do not rule out the noise-only hypothesis $A = 0$. JLA and Union2 give somewhat different constraints, though they are not statistically inconsistent. Note that differences remain even after restricting to the rather large subset of SNe that they have in common (dashed lines).

magnitudes differ is beyond the scope of this study, but we have explicitly checked that the difference between JLA and Union2 for the overlap set is largely due to differences in the estimated apparent magnitudes, not the redshifts.[7]

We also make connection to previous work in [180], where the first cosmological constraints from the correlations of SN Ia peculiar velocities have been obtained. Instead of parametrizing the covariance with a multiplicative amplitude, they jointly constrained the cosmological parameters Ω_m and σ_8. Using the earlier SN dataset from [177], they found constraints broadly consistent with ΛCDM values. Using the same dataset, we roughly agree with [180], our likelihood favoring $A \simeq 1.4$ with a large uncertainty but effectively ruling out $A = 0$. However, we note that the dataset of [177] includes some SNe with extremely low redshifts (as low as $z = 0.002$), which are not in the Hubble flow and for which the assumption of small residuals in eq. (6.8) breaks down (see also discussion after eq. (6.10)). Objects at such extremely low redshifts are mutually separated by distances of a few tens of Mpc; their relative velocities are therefore expected to have important nonlin-

[7] We have checked that the sky positions of JLA and Union2 overlapping SNe do precisely agree. We have also found that the subset of these SNe that are also found in the sample of [177] — 40 in total — have redshifts that mostly agree very well with JLA, but show larger discrepancies with Union2.

ear corrections, in addition to the linear relation eq. (6.8) breaking down, and the analysis would have to be carefully generalized to take this into account. When we exclude all SNe with $z < 0.01$ from the dataset of [177], the likelihood for A actually looks very similar to the JLA constraints in figure 6.2, favoring $A = 0$ but still statistically consistent with $A = 1$.

To summarize, we find that JLA, the most current and rigorous dataset, does not favor the presence of SN velocity covariance guaranteed in the ΛCDM model, but is nonetheless consistent with it. We also find that there is considerable variation in the SN data in terms of their constraints on the velocity covariance, and in particular that the optimistic-looking results found in [180] were due to some very-low-redshift SNe that may be too nearby for accurate modeling with linear theory.

The covariance of SN flux residuals has the potential to provide additional information about cosmological parameters and other interesting physics [181–185]. Our results suggest that current data do not yield interesting constraints. This will likely change with larger, homogeneous samples with greater sky coverage, such as those expected from the Large Synoptic Survey Telescope (LSST), currently under construction.

6.6 Constraints on excess bulk velocity

The optimal way to search for the effect of SN velocity correlations in the context of a fiducial cosmological model is to test for the presence of the full signal covariance, as we did in section 6.5. However, we can also use the SN magnitude residuals to search for a dipolar distortion (for example, due to bulk motion) beyond what is expected in ΛCDM. This provides constraints on physics beyond the concordance cosmology, such as a breaking of statistical isotropy or homogeneity, or the presence of a single large long-wavelength perturbation. The search for bulk flows is the subject of a significant body of literature. Here we use a different approach, and we make the connection to previous literature in the next section.

Bulk velocity is usually defined as the motion of the volume spanned by SNe Ia and the rest frame defined by the CMB. Moving the SN redshifts to the CMB frame, we are looking for an overall motion between the SN volume and the rest frame. Since we aim to search for an excess bulk flow *beyond* ΛCDM, we include the velocity correlations $\mathbf{S}$ in the likelihood, fixing $A = 1$. Since $\mathbf{S}$ includes all velocity correlations within ΛCDM, including the dipole, we expect the posterior for the bulk flow to be consistent with zero if ΛCDM provides a good description of the SN data. Of course, this assumes that our linear modeling of the velocity correlations is accurate for the SN sample and also that there are

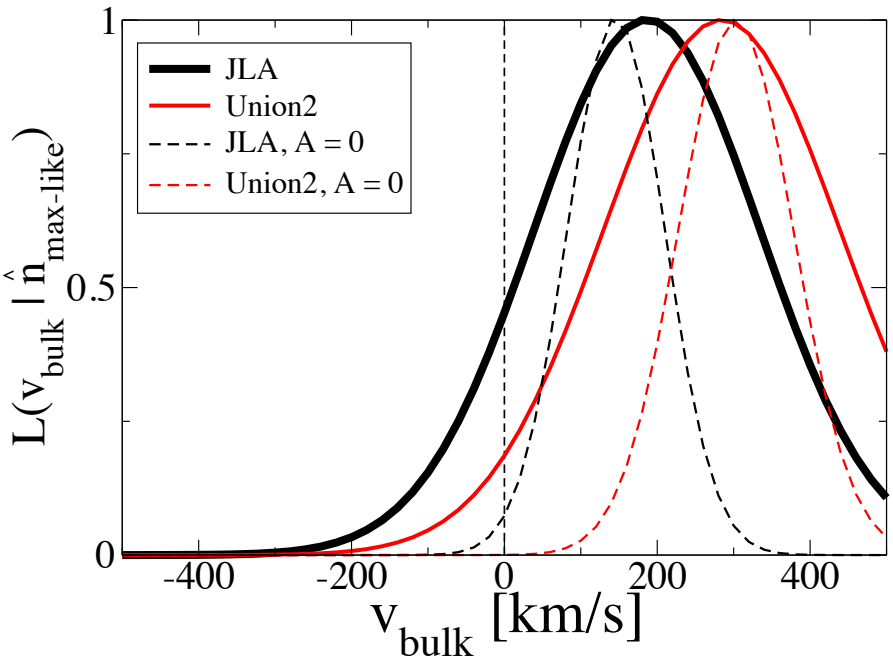

Figure 6.3: A slice through the 3D likelihood for excess bulk velocity. The direction is fixed to be $\hat{\mathbf{n}}_{\text{max-like}}$ (different for each dataset), while the amplitude of the dipole is varied and allowed to be positive or negative. Conclusions about the bulk flow would differ significantly if the velocity signal covariance were set to zero (dashed lines), as in most previous work on the subject.

no unaccounted-for systematic errors in the SN data that could masquerade as an excess bulk flow.

For this analysis, we therefore adopt the likelihood from eq. (6.21), setting $A = 1$ but allowing the bulk velocity $\mathbf{v}_{\text{bulk}} = (v_{\text{bulk}}, \theta, \phi)$ to vary in magnitude and direction. In order to get a sense of the three-dimensional likelihood $\mathcal{L}(v_{\text{bulk}}, \theta, \phi)$, we first consider the likelihood of the excess bulk flow amplitude in a cut through the best-fit direction, that is, as a function of v_{bulk} with θ and ϕ set to their maximum-likelihood values. This is shown in figure 6.3, and note that we continue the scan past zero velocity in the direction opposite that of the best fit by letting the amplitude of the bulk flow take negative values. Because the likelihood is Gaussian, and because $\mathbf{v}_{\text{bulk}}$ enters the observable magnitude linearly (see eq. (6.20)), the likelihood of the bulk velocity is also guaranteed to be Gaussian. Therefore, the likelihood ratio between the best-fit $(v_{\text{bulk}}, \theta, \phi)$ and $v_{\text{bulk}} = 0$ immediately translates into the confidence at which zero excess bulk velocity is ruled out, assuming uniform priors on each component of the vector $\mathbf{v}_{\text{bulk}}$.

Figure 6.3 shows that, once the velocity covariance is properly taken into account, SN data do not favor any bulk velocity beyond the amount expected in ΛCDM. For example,

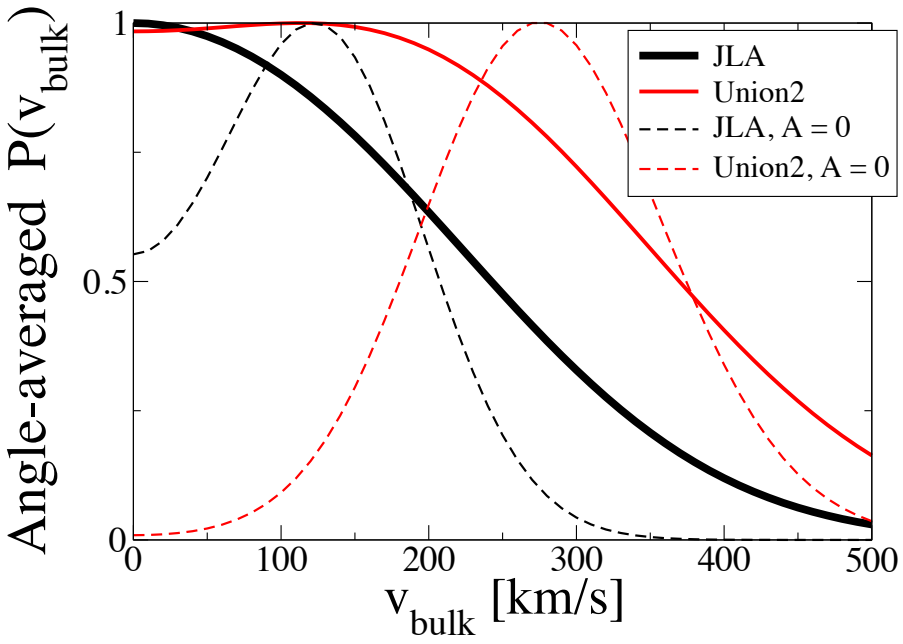

Figure 6.4: Angle-averaged posterior on the amplitude of bulk velocity in excess of the correlations captured by the full ΛCDM velocity covariance. Both JLA and Union2 data are consistent with zero velocity, with relatively large error. The conclusion would again be very different if the velocity covariance were artificially set to zero (dashed lines).

the JLA likelihood peaks at $(v_{\rm bulk}, l, b) = (187\ \text{km/s}, 323°, 25°)$, but this likelihood is larger than that for $v_{\rm bulk} = 0$ only by $-2\Delta \ln \mathcal{L} = -1.6$, far too low even for 68.3% (1σ) evidence, which in three dimensions would be $-2\Delta \ln \mathcal{L} \simeq -3.5$.

We would now like to explicitly calculate the posterior distribution of the amplitude of an excess bulk velocity. Assuming uniform priors on each component of $\mathbf{v}_{\rm bulk}$ would produce an additional $v_{\rm bulk}^2$ factor in the posterior, driving it to zero for the $v_{\rm bulk} = 0$ case so that $\mathbf{v}_{\rm bulk} = 0$ is automatically ruled out. An alternative that allows us to test the $\mathbf{v}_{\rm bulk} = 0$ assumption, implicitly (or explicitly [186]) adopted by most previous work, is to choose the prior $\Pr(v_{\rm bulk}) \propto 1/v_{\rm bulk}^2$ or, alternatively, to consider the angle-averaged likelihood

$$P^{\text{angle-averaged}}(\mathbf{v}_{\rm bulk}) \propto \int \mathcal{L}(\mathbf{v}_{\rm bulk})\, d\cos\theta\, d\phi\,. \tag{6.23}$$

We plot this likelihood in figure 6.4. It is immediately apparent that both JLA and Union2 data show no preference for excess bulk velocity, though there is a large uncertainty. Performing the same analysis but setting the velocity correlations to zero (so that $\mathbf{C} = \mathbf{N}$ with $\mathbf{S} = 0$), the results are drastically different, favoring bulk flows of several hundred km/s and, in the case of Union2, firmly ruling out the $v_{\rm bulk} = 0$ case. This is in agreement

with the conclusion found in previous work [187–192]. In the dashed curves shown in figure 6.4, we have not included the 150 km/s (300 km/s) scatter that is added in quadrature to the diagonal of the noise covariance $\mathbf{N}$ for JLA (Union2) data in some analyses. This clearly does not capture the significant full covariance of SN residuals due to large-scale structure. However, when adding back this contribution, we find nearly perfect agreement with the results of [189].

Given the importance of this issue, we stress again that the dashed lines in figures 6.3 and 6.4 *do not show the proper likelihood of any peculiar velocity*, ΛCDM or otherwise, since a guaranteed component of the covariance of the data has been neglected (nevertheless, one can still use these incorrect likelihoods to construct an estimator for bulk flow, which we will turn to in the next section). Since the velocity covariance $\mathbf{S}$ gives a guaranteed source of correlations in ΛCDM, we argue that it should always be included in likelihood analyses of SN magnitude residuals. Neglecting this covariance will lead to suboptimal estimators and, in general, biased results.

6.7 Relation to previous bulk flow measurements

A significant body of earlier work on SN velocities neglected the velocity covariance (and the lensing covariance, which is important at higher redshifts). These analyses often found evidence for non-zero bulk flow, and we confirm these findings with our dashed curves in figures 6.3 and 6.4. This bulk velocity with $A = 0$ is difficult to interpret, since it was obtained in an analysis with a guaranteed contribution to the covariance of the observables artificially set to zero.

Nevertheless, one can derive a theoretical expectation for what one should expect for the bulk velocity derived in this way; we call it $\mathbf{v}_{\text{bulk}}^{\text{noise-only}}$, and in some previous work it corresponds to what the authors simply call "bulk velocity." Note that this is not the *excess* bulk velocity over the ΛCDM expectation considered in the previous sections.

We will adopt the likelihood from eq. (6.21) once more, but we define a new vector $\mathbf{x}$ via $\mathbf{\Delta m}^{\text{bulk}}(\mathbf{v}_{\text{bulk}}) \equiv v_{\text{bulk}}\,\mathbf{x}$, where

$$x_i \equiv -\left(\frac{5}{\ln 10}\right)\,\frac{(1+z_i)^2}{H(z_i)d_L(z_i)}\,\hat{\mathbf{n}}_i \cdot \hat{\mathbf{n}}_{\text{bulk}}\,. \tag{6.24}$$

To estimate $v_{\text{bulk}}^{\text{noise-only}}$, we set the signal covariance to zero, assume a fixed direction $\hat{\mathbf{n}}_{\text{bulk}}$, and find the maximum of the likelihood; that is

$$\widehat{v}_{\text{bulk}}^{\text{noise-only}} \longleftrightarrow \max_{v_{\text{bulk}}}\,\left[\mathcal{L}(A=0,\mathbf{v}_{\text{bulk}})\right]\,. \tag{6.25}$$

Maximizing with respect to $v_{\rm bulk}$, one finds

$$\widehat{v}_{\rm bulk}^{\rm noise\text{-}only} = \frac{\mathbf{y}^\intercal\,\delta\mathbf{m}}{\mathbf{y}^\intercal\,\mathbf{x}}\,, \tag{6.26}$$

where we have defined for convenience a new vector $\mathbf{y}$ as $\mathbf{y} \equiv \mathbf{N}^{-1}\mathbf{x}$, and where $\delta\mathbf{m}$ is the vector of SN magnitude residuals (eq. (6.20) without the $\Delta m^{\rm bulk}$ term). Assuming ΛCDM, and still keeping the direction $\hat{\mathbf{n}}_{\rm bulk}$ fixed, the expected (mean) velocity is of course zero since $\langle \delta m_i \rangle = 0$.

We are more interested in the variance of this quantity, which can be computed directly and is equal to

$$\left\langle \left(\widehat{v}_{\rm bulk}^{\rm noise\text{-}only}\right)^2 \right\rangle = \frac{\mathbf{y}^\intercal(\mathbf{S}+\mathbf{N})\,\mathbf{y}}{(\mathbf{y}^\intercal\,\mathbf{x})^2}\,, \tag{6.27}$$

since the true SN magnitude covariance for ΛCDM is the sum of both signal and noise: $\langle (\delta m_i)(\delta m_j) \rangle = S_{ij} + N_{ij}$. The square root of this quantity is the desired theoretical expectation for the rms bulk velocity in ΛCDM when one ignores the signal covariance matrix.

Using the JLA SNe up to redshift $z = 0.05$, the ΛCDM expectation for the rms velocity varies from about 150–170 km/s as a function of $\hat{\mathbf{n}}_{\rm bulk}$, with a sky-averaged value of 162 km/s. Assuming only noise in the data, $\langle (\delta m_i)(\delta m_j) \rangle = N_{ij}$, the result is 71 km/s. The Union2 data give similar results.

We have therefore found that the predicted rms value of $v_{\rm bulk}^{\rm noise\text{-}only}$, assuming ΛCDM and SN data up to $z = 0.05$, is ∼160 km/s, and that nearly half of this value would be generated by statistical scatter in SN magnitudes in the absence of any peculiar velocities in the universe (such a contribution is sometimes referred to as the "noise bias"). The peak of the JLA likelihood (black dashed line in figure 6.4) is in agreement with the ΛCDM expectation; Union2 gives a somewhat larger result. Again, however, we caution that the analysis in this section is suboptimal, given that we do condense the data into a weighted dipole estimator $\widehat{v}_{\rm bulk}^{\rm noise\text{-}only}$ rather than using the full covariance. Moreover, this estimator is significantly affected by noise bias which needs to be subtracted. Given the uncertainties in the noise covariance, the subtraction of noise bias will lead to additional systematic uncertainties in the actual peculiar velocity measurement.

We have not attempted to repeat the analyses of some past work that studied the velocity field of low-redshift SNe [190–197] or the anisotropy of the universe from the distribution of nearby SN distances [198–203], since these studies adopted a wide variety of approaches and, in some cases, complicated statistical procedures whose results are calibrated on simulations. We emphasize, however, that the velocity covariance due to large-scale structure

	$P(A)$ (fig 6.2)				$v_{\rm bulk}^{\text{max-like}}$ (fig 6.3)		$v_{\rm bulk}^{\text{angle-avg}}$ (fig 6.4)
Survey	ML	95% C.L.	$\Delta\chi^2\big\vert_{A=0}$	$\Delta\chi^2\big\vert_{A=1}$	ML	95% C.L.	95% C.L.
JLA	0.19	$(0, 1.15)$	0.24	4.13	187	$(-108, 485)$	$(0, 376)$
Union2	1.19	$(0.19, 3.27)$	13.2	0.07	265	$(-37, 568)$	$(0, 456)$

Table 6.1: Summary of numerical results. For both JLA and Union2, we show the best-fit, maximum-likelihood (ML) values and 95% confidence intervals for A. We also show the quantity $\Delta\chi^2$ (that is, $-2\Delta \ln L$) between the best-fit value and special values $A = 0$ (no velocity signal) and $A = 1$ (ΛCDM velocity signal). We also show ML and 95% intervals for bulk velocity in the best-fit direction and 95% intervals for angle-averaged bulk velocity (here we do not report ML values, which are near zero). All velocities are in units of km/s.

should be included in any such analyses in order to obtain unbiased results and draw reliable statistical conclusions about the velocity field of the nearby universe.

6.8 Conclusions

In this paper we have revisited the constraints on bulk velocity — the relative motion of the volume populated by nearby SNe Ia and the rest frame defined by the CMB. Our emphasis was on a precise and clear procedure for selecting the data, performing the analysis, and modeling the theoretical expectation. We concentrated on SNe Ia as tracers of cosmic structure and studied two separate (but overlapping) datasets. Our methodology applies equally well to galaxies and other tracers of large-scale structure.

We argued, and demonstrated with explicit calculations, that inclusion of the "signal" covariance matrix that captures the peculiar velocity correlations between SNe is crucial. The velocities provide a guaranteed source of covariance between SNe; while the velocity contribution is subdominant compared to the noise except at the lowest redshifts (see figure 6.1), it does not become smaller as more SNe are included in the analysis. Neglecting the velocity covariance, as done by a significant body of earlier work on SN velocities and tests of statistical isotropy, leads to results that are both biased and difficult to interpret.

Our approach was based on a likelihood that includes both the signal and noise covariance and four free parameters: the normalization A, specifying the fraction of the signal added to the covariance, and three components of an excess bulk velocity $\mathbf{v}_{\rm bulk}$ beyond that which is encoded in the signal covariance. For the fiducial ΛCDM model, $A = 1$ and $\mathbf{v}_{\rm bulk} = 0$.

We first investigated whether the standard ΛCDM velocity covariance ($A = 1$) is preferred over the case in which the covariance is ignored ($A = 0$); that is, we constrained

$\mathcal{L}(A, \mathbf{v}_{\rm bulk} = 0)$. We found that the JLA dataset, while consistent with $A = 1$, cannot rule out $A = 0$, and in fact its likelihood peaks near zero (figure 6.2). Therefore, we did not find convincing evidence in the data for the correlations expected from velocities. Although we expect things to change with future data, when precise measurements of a quantity like A will effectively constrain cosmological parameters such as Ω_m and σ_8, our results indicate that current data are not close to providing such useful constraints.

We then pursued a different approach; we assumed a standard ΛCDM velocity covariance (the $A = 1$ case) and tested for excess bulk velocity $\mathbf{v}_{\rm bulk}$ beyond that already captured by the covariance — that is, we adopted the likelihood $\mathcal{L}(A = 1, \mathbf{v}_{\rm bulk})$ in the analysis. We found that current SN data provide no evidence for a departure from the null hypothesis $\mathbf{v}_{\rm bulk} = 0$ (figures 6.3 and 6.4). This result is in sharp contrast to the inference one would have made by ignoring the velocity covariance (that is, setting $A = 0$ in the same analysis), as some previous analyses in the literature have done.

To better understand this latter case, we separately studied inferred constraints on a "non-excess" bulk velocity where the velocity covariance has been ignored — that is, the $\mathcal{L}(A = 0, \mathbf{v}_{\rm bulk}^{\text{noise-only}})$ case. Note that this bulk velocity is more difficult to interpret since it was obtained by ignoring a guaranteed source of correlations in the data. We showed that the rms of the estimated $v_{\rm bulk}^{\text{noise-only}}$, assuming ΛCDM and SN data up to $z = 0.05$, is expected to be $\sim$160 km/s, and that nearly half of this value would be generated by a contribution purely from intrinsic and observational scatter in the SN magnitudes. Therefore, there are really two problems with this approach: not only is the constrained quantity difficult to interpret, but it is also guaranteed to be nonzero even without any peculiar velocities in the universe, which is clearly not optimal for cosmological interpretations.

The mapping of velocities in the universe using nearby tracers of large-scale structure has had a remarkably long and productive history. With upcoming large-field, fast-scanning surveys, it is likely that data will become of sufficiently high quality to enable peculiar velocities to progress to the next level and become competitive cosmological probes. Of course, data analysis and theoretical modeling will have to progress as well. In this paper we have demonstrated that, even for current data, clearly defining the quantities to be constrained and carefully accounting for the guaranteed correlations between objects due to large-scale structure are two factors of key importance.

CHAPTER 7

Closing Remarks

Summary

This dissertation investigated systematic effects and performed new cosmological tests with observational probes of dark energy in anticipation of the precision dark energy constraints expected in the near future. Chapters 2–4 studied systematic effects in dark energy probes, focusing on constraints from distance measurements, like those from Type Ia supernovae (SNe Ia). In Chapter 2, we quantified the effect of current SN Ia systematic errors on dark energy constraints, both for simple parametrizations of the equation of state and for a general description with principal components. Chapter 3 investigated recent evidence for a phantom equation of state using three separate SN Ia compilations, introducing new tests to search for systematic effects in the data. Chapter 4 was concerned with photometric calibration errors in the galaxy power spectrum. We highlighted the danger of multiplicative errors and, using a Fisher matrix formalism, demonstrated a simple way to mitigate these errors. Chapters 5–6 focused on tests of the standard cosmological model. In Chapter 5, we used Bayesian model comparison techniques with model-independent SN Ia and BAO data to directly test power law expansion as an alternative cosmological model. In Chapter 6, we used low-redshift SN Ia data to test for the presence of the peculiar velocity correlations predicted by the standard model. We clarified how these are connected to the bulk velocity of local structure.

As a whole, this body of work demonstrates how the distance probes of dark energy, particularly SNe Ia, can be employed in a variety of ways to test the standard cosmological model. It also highlights the many subtleties involved in using these probes for precise cosmological measurements, introducing new ways to understand and test for the presence of systematic effects in the data.

In the coming decade, as we enter an era of big data and of even more precision in cosmology, it will be important to reassess the limitations of cosmological probes. Effects that were once assumed negligible may become important. With so many different types of

data, not to mention the many associated cross-correlations, that one will want to analyze in combination, the question might soon become, which of these many probes are the most robust and reliable, rather than which have the best constraining power individually. From this standpoint, there is certainly an important role for the classic, well-studied probes of dark energy that were the main focus of this dissertation. Below I briefly discuss the future of these probes, particularly in the context of my own research interests.

CMB

CMB observations are packed with an enormous amount of detailed cosmological information. But with the exquisitely precise measurements of temperature fluctuations from *Planck*, it is not surprising that we are running into clear signs of tension among various data sets. Moderate disagreement with WMAP9 in *Planck*'s 2013 release was investigated in [93], and the tension between *Planck*'s value of H_0 (inferred assuming ΛCDM) and the local distance-ladder measurements of H_0 (e.g. [88], discussed in Sec. 3.3.5) is now well-known in the community. As illustrated nicely in [204], constraints on ΛCDM parameters from high multipoles ($\ell > 1000$) are in significant tension with those inferred from low multipoles ($\ell < 1000$), although the latter are now reasonably consistent with WMAP9 constraints from that same multipole range as well as with the low-redshift data (e.g. BAO, H_0). Further still, *Planck* SZ cluster counts disagree with those predicted from *Planck*'s own cosmology, and σ_8 inferred from *Planck* is lower than that inferred from weak lensing (e.g. [205]).

Obviously, sorting out these discrepancies is crucial; if nothing else, hopefully next-generation CMB experiments, which will seek precision polarization measurements at large and small scales, will help alleviate some of the confusion.

On the other hand, for dark energy research, the CMB distance priors provide most of the useful information (though CMB lensing is an important exception), and these will continue to be crucial for breaking dark energy parameter degeneracies. It is worth studying different ways to extract this distance information, for instance, whether the observables described in Sec. 3.2.3 are optimal or whether any such CMB observables are less likely to be affected by systematics. This latter issue is crucial, since the CMB distance now tends to dominate combined constraints for simple dark energy descriptions. The model dependence of the CMB is also an issue, and it would be helpful to understand, in the context of the newest CMB observations, which properties of the CMB are robust to various ΛCDM extensions.

BAO

Fortuitously, BAO distances are still typically limited by statistical errors (shot noise, cosmic sampling variance), and measurements of the BAO feature have nicely Gaussian errors, at least with the discussion in Sec. 2.4 about treating the tails of the likelihood for low-signal-to-noise detections notwithstanding. This may change when we aim to push BAO distance errors to below 1%. A separate question, however, is whether the BAO measurements, once they are obtained, indeed function as a standard ruler. Simulations will be needed here, and unfortunately the answer is probably model-dependent. It may be worth investigating other strategies for using the BAO feature (e.g. [206]) that are maximally reliable and model-independent.

With the newer anisotropic BAO measurements now available (e.g. [13], used in Chapter 5), another avenue now exists for testing isotropy and the ΛCDM model. The radial (line-of-sight) and transverse distances should agree, and interestingly, there is already tension here in the higher-redshift LyαF BAO (see Sec. 5.5). In the future, when anisotropic measurements exist for many redshift slices, it will be interesting to check whether there is broad agreement between the radial and transverse correlation functions. Agreement would build confidence in the robustness of BAO analyses, while disagreement would point to new physics if confirmed.

SNe Ia

As demonstrated in Chapter 2, SN Ia systematic errors are important even for current data. Of the systematic errors, photometric calibration uncertainty is the most damaging, and it will be the hardest and most important systematic error to control for future surveys. But pushing SN cosmology to its limits is certainly worth it. As a probe, SNe Ia are basically unique in that each individual SN has the ability to furnish a (nearly) statistically-independent, model-independent, 7% distance measurement.

SN cosmology is very empirical in nature; the stretch and color calibration relations, and the standard candle property itself, are not predicted by any model, at least in practice. There are many ways one could imagine revising or optimizing this modeling. Is it sufficient to model SNe with a single and/or fixed intrinsic scatter (see brief discussion in Sec. 5.6)? Is the likelihood for SN observables sufficiently Gaussian? Are fully Bayesian techniques (e.g. [207, 208]) more appropriate? Should such methods be expanded, or could they be simplified? Are there alternative models for SN light-curve corrections that better explain the observed data? Can any of the current assumptions be relaxed without losing cosmological information?

A precise, direct measurement of H_0, independent of the cosmological model and uncorrelated with other observations, is a key ingredient for precision dark energy constraints, as it ties relative distances from SNe to the precise distances from CMB and BAO observables. In recent years, various interrelated efforts have been made to characterize the effect of local structure on the H_0 measurements and to explain the small but consistent discrepancy between direct measurements and the CMB values. As low-redshift SNe ($z < 0.1$) are used as the last rung of the H_0 distance ladder, and SNe in this same range are used separately for cosmology, these measurements may be statistically correlated. On top of this, the peculiar velocity formalism of Chapter 6 is particularly relevant for these low-redshift SNe, where a sufficiently large sample of SNe essentially becomes a large-scale structure survey and should be modeled appropriately.

In light of this, we might ask, to what extent can one use the whole redshift range of SNe, not just the lowest-redshift sample, to determine H_0, and is this consistent with a purely local measurement? This would empirically test theoretical expectations for the effect of local structure. Better still, can measurements of Cepheids and other local distance indicators be combined with SNe Ia in a joint cosmological analysis? This would tie the local, low-redshift universe to the Hubble expansion in a maximally self-consistent way, effectively adding an H_0 measurement but also allowing the peculiar velocities, relevant to both H_0 and SN cosmology, and the other statistical correlations to be modeled simultaneously.

APPENDIX A

Analytic Marginalization Over Multiple SN Ia Absolute Magnitudes

The computational cost of varying additional nuisance parameters in a likelihood analysis can be reduced by marginalizing analytically over some of these parameters. The expression for the marginalized χ^2 will be more complicated, but fewer likelihoods will need to be computed in the analysis (in a brute-force grid search, many times fewer). Here we extend Appendix C of [17] and outline a procedure to marginalize analytically over a model with more than two $\mathcal{M}$.

The analytic marginalization over the single $\mathcal{M}$ in Eq. (3.1) is very straightforward. In this case, the marginalized χ^2 (for a flat prior) is given by

$$\begin{aligned}\chi^2_{\text{marg}} &= -2\log\int_{-\infty}^{\infty} e^{-\chi^2/2}\,\mathrm{d}\mathcal{M} \\ &= X_{00} + \log\left(\frac{X_{11}}{2\pi}\right) - \frac{X_{10}^2}{X_{11}}\,, \end{aligned} \tag{A.1}$$

where the unmarginalized χ^2 is given by Eq. (3.3) and

$$\begin{aligned} X_{00} &= \boldsymbol{\delta}^\intercal\,\mathbf{C}^{-1}\boldsymbol{\delta} \\ X_{10} &= \mathbf{1}^\intercal\,\mathbf{C}^{-1}\boldsymbol{\delta} \\ X_{11} &= \mathbf{1}^\intercal\,\mathbf{C}^{-1}\mathbf{1}\,. \end{aligned}$$

In the above, $\mathbf{1}$ is a vector of ones and $\boldsymbol{\delta}$ is the vector of magnitude residuals without the $\mathcal{M}$ term:

$$\boldsymbol{\delta} = \Delta\mathbf{m} + \mathcal{M}\,\mathbf{1} = \mathbf{m}_{\text{corr}} - 5\log_{10}\left(\frac{H_0}{c}\,\mathbf{D_L}\right)\,.$$

Marginalizing over a two-$\mathcal{M}$ model is a bit more complicated due to covariance between SNe with different $\mathcal{M}$. Ignoring this covariance will make things much simpler, but

the resulting constraints will be biased and the effect can be significant. For the two-$\mathcal{M}$ case, we modify Eq. (3.1) so that the vector of predicted SN magnitudes is given by

$$\mathbf{m}_{\rm th} = 5\log_{10}\left(\frac{H_0}{c}\,\mathbf{D_L}\right) + \mathcal{M}_1\,\mathbf{x}_1 + \mathcal{M}_2\,\mathbf{x}_2\ ,$$

where $\mathbf{x}_1$ ($\mathbf{x}_2$) is a vector with ones for SNe described by $\mathcal{M}_1$ ($\mathcal{M}_2$), and zeros otherwise. The marginalized χ^2 is given by

$$\begin{aligned}\chi^2_{\rm marg} &= X_{00} + \log\left(\frac{X}{4\pi^2}\right) \\ &\quad - \frac{1}{X}\left(X_{10}^2 X_{22} + X_{20}^2 X_{11} - 2X_{10}X_{20}X_{12}\right)\ ,\end{aligned} \tag{A.2}$$

where

$$\begin{aligned}X_{00} &= \boldsymbol{\delta}^\intercal\,\mathbf{C}^{-1}\boldsymbol{\delta} \\ X_{10} &= \mathbf{x}_1^\intercal\,\mathbf{C}^{-1}\boldsymbol{\delta} \\ X_{20} &= \mathbf{x}_2^\intercal\,\mathbf{C}^{-1}\boldsymbol{\delta} \\ X_{11} &= \mathbf{x}_1^\intercal\,\mathbf{C}^{-1}\mathbf{x}_1 \\ X_{22} &= \mathbf{x}_2^\intercal\,\mathbf{C}^{-1}\mathbf{x}_2 \\ X_{12} &= \mathbf{x}_1^\intercal\,\mathbf{C}^{-1}\mathbf{x}_2 \\ X &= X_{11}X_{22} - X_{12}^2\ .\end{aligned}$$

One can extrapolate the two-$\mathcal{M}$ case above to cases with three or more $\mathcal{M}$. This is straightforward, but the result quickly becomes very messy. Using the familiar result for the integral of a Gaussian function, one can compute the expression for several $\mathcal{M}$ using algebraic manipulation software. Explicit Mathematica code for marginalizing over six $\mathcal{M}$ (as in this work) is given below. The result must be simplified at intermediate steps to avoid long computation times, memory problems, or unmanageable final expressions. Still, the computation below takes several minutes, and the resulting expressions are very long (several pages of small type). This example can easily be modified for more or fewer $\mathcal{M}$ and for slightly different parametrizations of the SN magnitude (for instance, treating one $\mathcal{M}$ as a $\Delta\mathcal{M}$ so that some SNe are described by more than one such nuisance parameter).

```
fexp[{a_,b_,c_}] := b^2/(4*a)+c
fpre[{a_,b_,c_}] := a/Pi
g[f_,x_] := {-1*Coefficient[f,x^2],Coefficient[f,x],f/.x->0}
pre := 1
exp := -1/2*(X00-2*M1*X10-2*M2*X20-2*M3*X30-2*M4*X40-2*M5*X50-2*M6*X60
+M1^2*X11+M2^2*X22+M3^2*X33+M4^2*X44+M5^2*X55+M6^2*X66
+2*M1*M2*X12+2*M1*M3*X13+2*M1*M4*X14+2*M1*M5*X15+2*M1*M6*X16
+2*M2*M3*X23+2*M2*M4*X24+2*M2*M5*X25+2*M2*M6*X26+2*M3*M4*X34
+2*M3*M5*X35+2*M3*M6*X36+2*M4*M5*X45+2*M4*M6*X46+2*M5*M6*X56)
Do[{
coeffs = g[exp,Mi];
pre = FullSimplify[Expand[pre*fpre[coeffs]]];
exp = FullSimplify[Expand[fexp[coeffs]]]},{Mi,{M1,M2,M3,M4,M5,M6}}]
chisq_marg := Log[pre]-2*exp
```

APPENDIX B

The Biased Angular Power Spectrum

The observed (biased) angular power spectrum for tomographic redshift bins i and j is given by

$$T_\ell^{ij} = \frac{\sum_m \langle t^i_{\ell m} t^{j*}_{\ell m}\rangle}{2\ell+1} \,, \tag{B.1}$$

$$t^i_{\ell m} = \frac{1}{1+\epsilon^i}\left[a^i_{\ell m} + c^i_{\ell m} + \sum_{\substack{\ell_1 m_1\\ \ell_2 m_2}} R^{\ell_1\,\ell_2\,\ell}_{m_1 m_2 m}\, c^i_{\ell_1 m_1} a^i_{\ell_2 m_2} - \sqrt{4\pi}\,\epsilon^i\,\delta_{\ell 0}\right] \,, \tag{B.2}$$

$$\epsilon^i = \frac{c^i_{00}}{\sqrt{4\pi}} + \frac{1}{4\pi}\sum_{\ell m} c^i_{\ell m} a^{i*}_{\ell m} \,, \tag{B.3}$$

where the R coupling is defined in Eq. (4.12). Since the monopole of the calibration field (or equivalently, the true mean galaxy density $\bar{N}$) is not measurable, we are free to specify a value, so we choose $c^i_{00} = (-1/\sqrt{4\pi})\sum_{\ell m} c^i_{\ell m} a^{i*}_{\ell m}$ so that $\epsilon^i = 0$. Then

$$\begin{aligned} T_\ell^{ij} = \frac{1}{2\ell+1}\sum_m \Bigg\langle \Bigg[& (a^i_{\ell m} + c^i_{\ell m})\,(a^{j*}_{\ell m} + c^{j*}_{\ell m}) \\ & + \sum_{\substack{\ell_1 m_1\\ \ell_2 m_2}}\sum_{\substack{\ell'_1 m'_1\\ \ell'_2 m'_2}} R^{\ell_1\,\ell_2\,\ell}_{m_1 m_2 m} R^{\ell'_1\,\ell'_2\,\ell}_{m'_1 m'_2 m}\, c^i_{\ell_1 m_1} a^i_{\ell_2 m_2}\, c^{j*}_{\ell'_1 m'_1}\, a^{j*}_{\ell'_2 m'_2} \\ & + \sum_{\substack{\ell_1 m_1\\ \ell_2 m_2}} R^{\ell_1\,\ell_2\,\ell}_{m_1 m_2 m}\left[(a^i_{\ell m} + c^i_{\ell m})\, c^{j*}_{\ell_1 m_1} a^{j*}_{\ell_2 m_2} + (a^{j*}_{\ell m} + c^{j*}_{\ell m})\, c^i_{\ell_1 m_1} a^i_{\ell_2 m_2}\right] \Bigg] \Bigg\rangle \end{aligned} \tag{B.4}$$

Calculating the ensemble averages, we assume that the cosmological three-point function vanishes and that the $c_{\ell m}$ are fixed (not random) variables, with the exception of c_{00} which must be considered separately. Using the definition of $C_\ell^{\rm cal}$ in Eq. (4.14), we have (for

$\ell \neq 0$)

$$
\begin{aligned}
T_\ell^{ij} &= C_\ell^{ij} + C_\ell^{\mathrm{cal}(ij)} - \frac{1}{4\pi} C_\ell^{\mathrm{cal}(ij)} \left[C_\ell^{ii} + C_\ell^{jj} \right] \\
&\quad + \frac{1}{4\pi} \sum_{\substack{\ell_1 \neq 0 \\ \ell_2 \neq 0}} (2\ell_1 + 1)\, C_{\ell_1}^{\mathrm{cal}(ij)} \begin{pmatrix} \ell_1 & \ell_2 & \ell \\ 0 & 0 & 0 \end{pmatrix}^2 (2\ell_2 + 1)\, C_{\ell_2}^{ij} \\
&\quad + \frac{1}{(4\pi)^2} \left[C_\ell^{\mathrm{cal}(ij)} \left[C_\ell^{ii} C_\ell^{jj} + (C_\ell^{ij})^2 \right] + C_\ell^{ij} \sum_{\ell' \neq 0} (2\ell' + 1)\, C_{\ell'}^{ij} C_{\ell'}^{\mathrm{cal}(ij)} \right] .
\end{aligned}
\tag{B.5}
$$

Note that a_{00}, C_0, t_{00}, and T_0 are all equal to zero by construction, while C_0^{cal} does not contribute and is left undefined. Restricting to auto-power spectra only, dropping the redundant redshift bin indices, and neglecting the last group of terms (which is suppressed by an extra factor of order C_ℓ relative to the other terms), we have

$$
T_\ell = C_\ell + C_\ell^{\mathrm{cal}} - \frac{1}{2\pi} C_\ell^{\mathrm{cal}} C_\ell + \frac{1}{4\pi} \sum_{\substack{\ell_1 \neq 0 \\ \ell_2 \neq 0}} (2\ell_1 + 1)\, C_{\ell_1}^{\mathrm{cal}} \begin{pmatrix} \ell_1 & \ell_2 & \ell \\ 0 & 0 & 0 \end{pmatrix}^2 (2\ell_2 + 1)\, C_{\ell_2} \,, \tag{B.6}
$$

which matches Eq. (4.13) in the text.

The following relations involving Wigner 3-j symbols were useful for simplifying the expression for T_ℓ and for computing the symbols numerically:

$$
\sum_m (-1)^m \begin{pmatrix} \ell & \ell & L \\ m & -m & 0 \end{pmatrix} = (-1)^\ell \sqrt{2\ell + 1}\, \delta_{L0} \tag{B.7}
$$

$$
\sum_{\ell m} (2\ell + 1) \begin{pmatrix} \ell_1 & \ell_2 & \ell \\ m_1 & m_2 & m \end{pmatrix} \begin{pmatrix} \ell_1 & \ell_2 & \ell \\ m_1' & m_2' & m \end{pmatrix} = \delta_{m_1 m_1'}\, \delta_{m_2 m_2'} \tag{B.8}
$$

$$
\sum_{m_1 m_2} (2\ell + 1) \begin{pmatrix} \ell_1 & \ell_2 & \ell \\ m_1 & m_2 & m \end{pmatrix} \begin{pmatrix} \ell_1 & \ell_2 & \ell' \\ m_1 & m_2 & m' \end{pmatrix} = \delta_{\ell \ell'}\, \delta_{m m'} \tag{B.9}
$$

$$
\begin{pmatrix} \ell & \ell & 0 \\ m & -m & 0 \end{pmatrix} = \frac{(-1)^{\ell - m}}{\sqrt{2\ell + 1}} \tag{B.10}
$$

$$
\begin{aligned}
\begin{pmatrix} \ell_1 & \ell_2 & \ell \\ 0 & 0 & 0 \end{pmatrix} &= (-1)^g \sqrt{\frac{(2g - 2\ell_1)!\, (2g - 2\ell_2)!\, (2g - 2\ell)!}{(2g + 1)!}} \\
&\quad \times \frac{g!}{(g - \ell_1)!\, (g - \ell_2)!\, (g - \ell)!} \,, \text{ for integer } g = \frac{\ell_1 + \ell_2 + \ell}{2}
\end{aligned}
\tag{B.11}
$$

BIBLIOGRAPHY

[1] E. J. Ruiz, D. L. Shafer, D. Huterer, and A. Conley, Phys. Rev. **D86**, 103004 (2012), arXiv:1207.4781 [astro-ph.CO] .

[2] D. L. Shafer and D. Huterer, Phys. Rev. **D89**, 063510 (2014), arXiv:1312.1688 [astro-ph.CO] .

[3] D. L. Shafer and D. Huterer, Mon. Not. Roy. Astron. Soc. **447**, 2961 (2015), arXiv:1410.0035 [astro-ph.CO] .

[4] D. L. Shafer, Phys. Rev. **D91**, 103516 (2015), arXiv:1502.05416 [astro-ph.CO] .

[5] D. Huterer, D. L. Shafer, and F. Schmidt, JCAP **1512**, 033 (2015), arXiv:1509.04708 [astro-ph.CO] .

[6] S. Carroll, *Spacetime and Geometry: An Introduction to General Relativity* (Addison-Wesley, San Francisco, CA, 2003).

[7] P. Ade *et al.* (Planck Collaboration), Astron.Astrophys. **571**, A16 (2014), arXiv:1303.5076 [astro-ph.CO] .

[8] A. G. Riess *et al.* (Supernova Search Team), Astron.J. **116**, 1009 (1998), arXiv:astro-ph/9805201 [astro-ph] .

[9] S. Perlmutter *et al.* (Supernova Cosmology Project), Astrophys.J. **517**, 565 (1999), arXiv:astro-ph/9812133 [astro-ph] .

[10] D. J. Eisenstein *et al.* (SDSS Collaboration), Astrophys.J. **633**, 560 (2005), arXiv:astro-ph/0501171 [astro-ph] .

[11] F. Beutler, C. Blake, M. Colless, D. H. Jones, L. Staveley-Smith, *et al.*, Mon.Not.Roy.Astron.Soc. **416**, 3017 (2011), arXiv:1106.3366 [astro-ph.CO] .

[12] R. Tojeiro, A. J. Ross, A. Burden, L. Samushia, M. Manera, *et al.*, Mon.Not.Roy.Astron.Soc. **440**, 2222 (2014), arXiv:1401.1768 [astro-ph.CO] .

[13] L. Anderson *et al.* (BOSS Collaboration), Mon.Not.Roy.Astron.Soc. **441**, 24 (2014), arXiv:1312.4877 [astro-ph.CO] .

[14] T. Delubac *et al.* (BOSS Collaboration), Astron.Astrophys. **574**, A59 (2015), arXiv:1404.1801 [astro-ph.CO] .

[15] J. Frieman, M. Turner, and D. Huterer, Ann.Rev.Astron.Astrophys. **46**, 385 (2008), arXiv:0803.0982 [astro-ph] .

[16] D. H. Weinberg, M. J. Mortonson, D. J. Eisenstein, C. Hirata, A. G. Riess, *et al.*, Phys.Rept. **530**, 87 (2013), arXiv:1201.2434 [astro-ph.CO] .

[17] A. Conley *et al.* (SNLS), Astrophys. J. Suppl. **192**, 1 (2011), arXiv:1104.1443 [astro-ph.CO] .

[18] W. M. Wood-Vasey *et al.* (ESSENCE Collaboration), Astrophys.J. **666**, 694 (2007), arXiv:astro-ph/0701041 [astro-ph] .

[19] M. Hicken, W. M. Wood-Vasey, S. Blondin, P. Challis, S. Jha, *et al.*, Astrophys.J. **700**, 1097 (2009), arXiv:0901.4804 [astro-ph.CO] .

[20] R. Kessler, A. Becker, D. Cinabro, J. Vanderplas, J. A. Frieman, *et al.*, Astrophys.J.Suppl. **185**, 32 (2009), arXiv:0908.4274 [astro-ph.CO] .

[21] M. Sullivan, J. Guy, A. Conley, N. Regnault, P. Astier, *et al.*, Astrophys.J. **737**, 102 (2011), arXiv:1104.1444 .

[22] T. M. Davis, E. Mortsell, J. Sollerman, A. Becker, S. Blondin, *et al.*, Astrophys.J. **666**, 716 (2007), arXiv:astro-ph/0701510 [astro-ph] .

[23] D. Rubin, E. Linder, M. Kowalski, G. Aldering, R. Amanullah, *et al.*, Astrophys.J. **695**, 391 (2009), arXiv:0807.1108 [astro-ph] .

[24] R. Amanullah *et al.*, Astrophys. J. **716**, 712 (2010), arXiv:1004.1711 [astro-ph.CO] .

[25] N. Suzuki *et al.*, Astrophys. J. **746**, 85 (2012), arXiv:1105.3470 [astro-ph.CO] .

[26] M. J. Mortonson, W. Hu, and D. Huterer, Phys. Rev. **D81**, 063007 (2010), arXiv:0912.3816 .

[27] M. Mortonson, W. Hu, and D. Huterer, Phys. Rev. **D82**, 063004 (2010).

[28] D. Huterer and A. Cooray, Phys.Rev. **D71**, 023506 (2005), arXiv:astro-ph/0404062 [astro-ph] .

[29] Y. Wang and M. Tegmark, Phys. Rev. **D71**, 103513 (2005), astro-ph/0501351 .

[30] C. Zunckel and R. Trotta, Mon. Not. Roy. Astron. Soc. **380**, 865 (2007), astro-ph/0702695 .

[31] G.-B. Zhao, D. Huterer, and X. Zhang, Phys. Rev. **D77**, 121302 (2008), arXiv:0712.2277 .

[32] A. Hojjati, L. Pogosian, and G.-B. Zhao, JCAP **1004**, 007 (2010), arXiv:0912.4843 .

[33] E. E. Ishida and R. S. de Souza, Astron.Astrophys. **527**, A49 (2011), arXiv:1012.5335 .

[34] A. Shafieloo, A. G. Kim, and E. V. Linder, (2012), arXiv:1204.2272 .

[35] M. Seikel, C. Clarkson, and M. Smith, JCAP **1206**, 036 (2012), arXiv:1204.2832 .

[36] G.-B. Zhao, R. G. Crittenden, L. Pogosian, and X. Zhang, (2012), arXiv:1207.3804 .

[37] J. Guy *et al.* (SNLS Collaboration), Astron.Astrophys. **466**, 11 (2007), arXiv:astro-ph/0701828 [ASTRO-PH] .

[38] B. C. Kelly, Astrophys.J. **665**, 1489 (2007), arXiv:0705.2774 [astro-ph] .

[39] W. J. Percival *et al.* (SDSS Collaboration), Mon.Not.Roy.Astron.Soc. **401**, 2148 (2010), arXiv:0907.1660 [astro-ph.CO] .

[40] C. Blake, S. Brough, M. Colless, C. Contreras, W. Couch, *et al.*, (2012), arXiv:1204.3674 .

[41] C. Blake, E. Kazin, F. Beutler, T. Davis, D. Parkinson, *et al.*, Mon.Not.Roy.Astron.Soc. **418**, 1707 (2011), arXiv:1108.2635 [astro-ph.CO] .

[42] A. G. Sanchez, C. Scoccola, A. Ross, W. Percival, M. Manera, *et al.*, (2012), arXiv:1203.6616 .

[43] L. Anderson, E. Aubourg, S. Bailey, D. Bizyaev, M. Blanton, *et al.*, Mon.Not.Roy.Astron.Soc. **427**, 3435 (2013), arXiv:1203.6594 [astro-ph.CO] .

[44] J. A. Frieman, D. Huterer, E. V. Linder, and M. S. Turner, Phys.Rev. **D67**, 083505 (2003), arXiv:astro-ph/0208100 [astro-ph] .

[45] E. Komatsu *et al.* (WMAP), Astrophys. J. Suppl. **192**, 18 (2011), arXiv:1001.4538 .

[46] N. Christensen, R. Meyer, L. Knox, and B. Luey, Class. Quant. Grav. **18**, 2677 (2001), astro-ph/0103134 .

[47] J. Dunkley, M. Bucher, P. G. Ferreira, K. Moodley, and C. Skordis, Mon.Not.Roy.Astron.Soc. **356**, 925 (2005), astro-ph/0405462 .

[48] N. Metropolis, A. Rosenbluth, M. Rosenbluth, A. Teller, and E. Teller, J.Chem.Phys. **21**, 1087 (1953).

[49] W. Hastings, Biometrika **57**, 97 (1970).

[50] A. Gelman and D. Rubin, Statistical Science **7**, 452 (1992).

[51] A. Lewis and S. Bridle, Phys. Rev. **D66**, 103511 (2002), astro-ph/0205436 .

[52] E. V. Linder, Phys.Rev.Lett. **90**, 091301 (2003), arXiv:astro-ph/0208512 [astro-ph] .

[53] D. Huterer and G. Starkman, Phys. Rev. Lett. **90**, 031301 (2003), astro-ph/0207517 .

[54] M. Chevallier and D. Polarski, Int. J. Mod. Phys. **D10**, 213 (2001), gr-qc/0009008 .

[55] A. Albrecht *et al.*, (2006), astro-ph/0609591 .

[56] D. Huterer and M. S. Turner, Phys. Rev. **D64**, 123527 (2001), astro-ph/0012510 .

[57] A. J. Albrecht *et al.*, (2009), arXiv:0901.0721 .

[58] M. J. Mortonson, W. Hu, and D. Huterer, Phys. Rev. **D79**, 023004 (2009), arXiv:0810.1744 .

[59] B. A. Bassett and N. Afshordi, (2010), arXiv:1005.1664 [astro-ph.CO] .

[60] R. Kessler, B. Bassett, P. Belov, V. Bhatnagar, H. Campbell, *et al.*, Publ.Astron.Soc.Pac. **122**, 1415 (2010), arXiv:1008.1024 .

[61] R. Hlozek, M. Kunz, B. Bassett, M. Smith, J. Newling, *et al.*, Astrophys.J. **752**, 79 (2012), arXiv:1111.5328 .

[62] A. G. Riess, L.-G. Strolger, S. Casertano, H. C. Ferguson, B. Mobasher, *et al.*, Astrophys.J. **659**, 98 (2007), arXiv:astro-ph/0611572 [astro-ph] .

[63] R. A. Knop *et al.* (Supernova Cosmology Project), Astrophys.J. **598**, 102 (2003), arXiv:astro-ph/0309368 [astro-ph] .

[64] P. Astier *et al.* (SNLS Collaboration), Astron.Astrophys. **447**, 31 (2006), arXiv:astro-ph/0510447 [astro-ph] .

[65] W. L. Freedman, C. R. Burns, M. Phillips, P. Wyatt, S. Persson, *et al.*, Astrophys.J. **704**, 1036 (2009), arXiv:0907.4524 [astro-ph.CO] .

[66] M. Kowalski *et al.* (Supernova Cosmology Project), Astrophys.J. **686**, 749 (2008), arXiv:0804.4142 [astro-ph] .

[67] U. Alam, V. Sahni, and A. A. Starobinsky, JCAP **0702**, 011 (2007), arXiv:astro-ph/0612381 [astro-ph] .

[68] S. Nesseris and L. Perivolaropoulos, JCAP **0702**, 025 (2007), arXiv:astro-ph/0612653 [astro-ph] .

[69] G.-B. Zhao and X.-m. Zhang, Phys.Rev. **D81**, 043518 (2010), arXiv:0908.1568 [astro-ph.CO] .

[70] A. Rest, D. Scolnic, R. Foley, M. Huber, R. Chornock, *et al.*, (2013), arXiv:1310.3828 [astro-ph.CO] .

[71] D. Scolnic, A. Rest, A. Riess, M. Huber, R. Foley, *et al.*, Astrophys.J. **795**, 45 (2014), arXiv:1310.3824 [astro-ph.CO] .

[72] C. Cheng and Q.-G. Huang, Phys.Rev. **D89**, 043003 (2014), arXiv:1306.4091 [astro-ph.CO] .

[73] J.-Q. Xia, H. Li, and X. Zhang, Phys.Rev. **D88**, 063501 (2013), arXiv:1308.0188 [astro-ph.CO] .

[74] A. J. Conley, M. Sullivan, E. Hsiao, J. Guy, P. Astier, *et al.*, (2008), arXiv:0803.3441 [astro-ph] .

[75] M. Betoule *et al.* (SDSS), Astron. Astrophys. **552**, A124 (2013), arXiv:1212.4864 [astro-ph.CO] .

[76] N. Padmanabhan, X. Xu, D. J. Eisenstein, R. Scalzo, A. J. Cuesta, *et al.*, Mon.Not.Roy.Astron.Soc. **427**, 2132 (2012), arXiv:1202.0090 [astro-ph.CO] .

[77] D. J. Eisenstein and W. Hu, Astrophys.J. **496**, 605 (1998), arXiv:astro-ph/9709112 [astro-ph] .

[78] G. Hinshaw *et al.* (WMAP), Astrophys.J.Suppl. **208**, 19 (2013), arXiv:1212.5226 [astro-ph.CO] .

[79] W. Hu and N. Sugiyama, Astrophys.J. **471**, 542 (1996), arXiv:astro-ph/9510117 [astro-ph] .

[80] Y. Wang and S. Wang, Phys.Rev. **D88**, 043522 (2013), arXiv:1304.4514 [astro-ph.CO] .

[81] M. Sullivan *et al.* (SNLS Collaboration), Mon.Not.Roy.Astron.Soc. **406**, 782 (2010), arXiv:1003.5119 [astro-ph.CO] .

[82] R. R. Gupta, C. B. D'Andrea, M. Sako, C. Conroy, M. Smith, *et al.*, Astrophys.J. **740**, 92 (2011), arXiv:1107.6003 [astro-ph.CO] .

[83] R. Kessler, J. Guy, J. Marriner, M. Betoule, J. Brinkmann, *et al.*, Astrophys.J. **764**, 48 (2013), arXiv:1209.2482 [astro-ph.CO] .

[84] J. Johansson, D. Thomas, J. Pforr, C. Maraston, R. C. Nichol, *et al.*, (2012), arXiv:1211.1386 [astro-ph.CO] .

[85] M. Childress, G. Aldering, P. Antilogus, C. Aragon, S. Bailey, *et al.*, Astrophys.J. **770**, 108 (2013), arXiv:1304.4720 [astro-ph.CO] .

[86] S. Wang and Y. Wang, Phys.Rev. **D88**, 043511 (2013), arXiv:1306.6423 [astro-ph.CO] .

[87] M. Rigault, Y. Copin, G. Aldering, P. Antilogus, C. Aragon, *et al.*, Astron.Astrophys. **560**, A66 (2013), arXiv:1309.1182 [astro-ph.CO] .

[88] A. G. Riess, L. Macri, S. Casertano, H. Lampeitl, H. C. Ferguson, *et al.*, Astrophys.J. **730**, 119 (2011), arXiv:1103.2976 [astro-ph.CO] .

[89] W. Hu, ASP Conf.Ser. **339**, 215 (2005), arXiv:astro-ph/0407158 [astro-ph] .

[90] G. Efstathiou, (2013), arXiv:1311.3461 [astro-ph.CO] .

[91] V. Marra, L. Amendola, I. Sawicki, and W. Valkenburg, Phys.Rev.Lett. **110**, 241305 (2013), arXiv:1303.3121 [astro-ph.CO] .

[92] E. Macaulay, I. K. Wehus, and H. K. Eriksen, (2013), arXiv:1303.6583 [astro-ph.CO] .

[93] D. N. Spergel, R. Flauger, and R. Hlozek, Phys. Rev. **D91**, 023518 (2015), arXiv:1312.3313 [astro-ph.CO] .

[94] V. de Lapparent, M. J. Geller, and J. P. Huchra, Astrophys.J. **302**, L1 (1986).

[95] S. Maddox, G. Efstathiou, W. Sutherland, and J. Loveday, Mon.Not.Roy.Astron.Soc. **243**, 692 (1990).

[96] M. Colless *et al.* (2DFGRS Collaboration), Mon.Not.Roy.Astron.Soc. **328**, 1039 (2001), arXiv:astro-ph/0106498 [astro-ph] .

[97] S. Cole *et al.* (2dFGRS Collaboration), Mon.Not.Roy.Astron.Soc. **362**, 505 (2005), arXiv:astro-ph/0501174 [astro-ph] .

[98] D. Parkinson, S. Riemer-Sorensen, C. Blake, G. B. Poole, T. M. Davis, *et al.*, Phys.Rev. **D86**, 103518 (2012), arXiv:1210.2130 [astro-ph.CO] .

[99] D. G. York *et al.* (SDSS Collaboration), Astron.J. **120**, 1579 (2000), arXiv:astro-ph/0006396 [astro-ph] .

[100] M. Tegmark *et al.* (SDSS Collaboration), Astrophys.J. **606**, 702 (2004), arXiv:astro-ph/0310725 [astro-ph] .

[101] K. N. Abazajian *et al.* (SDSS Collaboration), Astrophys.J.Suppl. **182**, 543 (2009), arXiv:0812.0649 [astro-ph] .

[102] C. P. Ahn *et al.* (SDSS Collaboration), Astrophys.J.Suppl. **203**, 21 (2012), arXiv:1207.7137 [astro-ph.IM] .

[103] K. S. Dawson *et al.* (BOSS Collaboration), Astron.J. **145**, 10 (2013), arXiv:1208.0022 [astro-ph.CO] .

[104] A. J. Ross, L. Samushia, C. Howlett, W. J. Percival, A. Burden, *et al.*, Mon.Not.Roy.Astron.Soc., in press (2015), arXiv:1409.3242 [astro-ph.CO] .

[105] T. Abbott *et al.* (Dark Energy Survey Collaboration), astro-ph/0510346 (2005), arXiv:astro-ph/0510346 [astro-ph] .

[106] Z. Ivezic, J. Tyson, R. Allsman, J. Andrew, and R. Angel (LSST Collaboration), 0805.2366 (2008), arXiv:0805.2366 [astro-ph] .

[107] R. Laureijs *et al.* (EUCLID Collaboration), 1110.3193 (2011), arXiv:1110.3193 [astro-ph.CO] .

[108] T. Goto, I. Szapudi, and B. R. Granett, Mon.Not.Roy.Astron.Soc. **422**, L77 (2012), arXiv:1202.5306 [astro-ph.CO] .

[109] A. R. Pullen and C. M. Hirata, Publications of the Astronomical Society of the Pacific, Volume 125, Issue 928, pp. **705-718** (2013), 10.1086/671189, arXiv:1212.4500 [astro-ph.CO] .

[110] S. Ho, A. Cuesta, H.-J. Seo, R. de Putter, A. J. Ross, *et al.*, Astrophys.J. **761**, 14 (2012), arXiv:1201.2137 [astro-ph.CO] .

[111] S. Ho, N. Agarwal, A. D. Myers, R. Lyons, A. Disbrow, *et al.*, 1311.2597 (2013), arXiv:1311.2597 [astro-ph.CO] .

[112] N. Agarwal, S. Ho, and S. Shandera, JCAP **1402**, 038 (2014), arXiv:1311.2606 [astro-ph.CO] .

[113] T. Giannantonio, A. J. Ross, W. J. Percival, R. Crittenden, D. Bacher, *et al.*, Phys.Rev. **D89**, 023511 (2014), arXiv:1303.1349 [astro-ph.CO] .

[114] N. Agarwal, S. Ho, A. D. Myers, H.-J. Seo, A. J. Ross, *et al.*, JCAP **1404**, 007 (2014), arXiv:1309.2954 [astro-ph.CO] .

[115] A. J. Ross, S. Ho, A. J. Cuesta, R. Tojeiro, W. J. Percival, *et al.*, Mon.Not.Roy.Astron.Soc. **417**, 1350 (2011), arXiv:1105.2320 [astro-ph.CO] .

[116] B. Leistedt, H. V. Peiris, D. J. Mortlock, A. Benoit-Lévy, and A. Pontzen, Mon.Not.Roy.Astron.Soc. **435**, 1857 (2013), arXiv:1306.0005 [astro-ph.CO] .

[117] B. Leistedt and H. V. Peiris, Mon.Not.Roy.Astron.Soc. **444**, 2 (2014), arXiv:1404.6530 [astro-ph.CO] .

[118] D. Huterer, C. E. Cunha, and W. Fang, Mon.Not.Roy.Astron.Soc. **432**, 2945 (2013), arXiv:1211.1015 [astro-ph.CO] .

[119] L. Knox, R. Scoccimarro, and S. Dodelson, Phys.Rev.Lett. **81**, 2004 (1998), arXiv:astro-ph/9805012 [astro-ph] .

[120] D. Huterer, Phys.Rev. **D65**, 063001 (2002), arXiv:astro-ph/0106399 [astro-ph] .

[121] A. Lewis, A. Challinor, and A. Lasenby, Astrophys.J. **538**, 473 (2000), arXiv:astro-ph/9911177 [astro-ph] .

[122] G. Efstathiou, Mon.Not.Roy.Astron.Soc. **348**, 885 (2004), arXiv:astro-ph/0310207 [astro-ph] .

[123] A. Pontzen and H. V. Peiris, Phys.Rev. **D81**, 103008 (2010), arXiv:1004.2706 [astro-ph.CO] .

[124] M. Kaplinghat, G. Steigman, I. Tkachev, and T. Walker, Phys.Rev. **D59**, 043514 (1999), arXiv:astro-ph/9805114 [astro-ph] .

[125] M. Kaplinghat, G. Steigman, and T. Walker, Phys.Rev. **D61**, 103507 (2000), arXiv:astro-ph/9911066 [astro-ph] .

[126] A. Dolgov, Phys.Rev. **D55**, 5881 (1997), arXiv:astro-ph/9608175 [astro-ph] .

[127] D. Jain, A. Dev, and J. Alcaniz, Class.Quant.Grav. **20**, 4485 (2003), arXiv:astro-ph/0302025 [astro-ph] .

[128] G. Sethi, A. Dev, and D. Jain, Phys.Lett. **B624**, 135 (2005), arXiv:astro-ph/0506255 [astro-ph] .

[129] Z.-H. Zhu, M. Hu, J. Alcaniz, and Y.-X. Liu, Astron.Astrophys. **483**, 15 (2008), arXiv:0712.3602 [astro-ph] .

[130] A. Dolgov, V. Halenka, and I. Tkachev, JCAP **1410**, 047 (2014), arXiv:1406.2445 [astro-ph.CO] .

[131] F. Melia and A. Shevchuk, Mon.Not.Roy.Astron.Soc. **419**, 2579 (2012), arXiv:1109.5189 [astro-ph.CO] .

[132] A. Dev, M. Sethi, and D. Lohiya, Phys.Lett. **B504**, 207 (2001), arXiv:astro-ph/0008193 [astro-ph] .

[133] A. Dev, M. Safonova, D. Jain, and D. Lohiya, Phys.Lett. **B548**, 12 (2002), arXiv:astro-ph/0204150 [astro-ph] .

[134] G. F. Lewis, Mon.Not.Roy.Astron.Soc. **432**, 2324 (2013), arXiv:1304.1248 [astro-ph.CO] .

[135] F. Melia, Mon.Not.Roy.Astron.Soc. **446**, 1191 (2015), arXiv:1406.4918 [astro-ph.CO] .

[136] G. F. Lewis, Mon.Not.Roy.Astron.Soc.Lett. **431**, L25 (2013), arXiv:1301.0305 [astro-ph.CO] .

[137] M. Bilicki and M. Seikel, Mon.Not.Roy.Astron.Soc. **425**, 1664 (2012), arXiv:1206.5130 [astro-ph.CO] .

[138] F. Melia and R. S. Maier, Mon.Not.Roy.Astron.Soc. **432**, 2669 (2013), arXiv:1304.1802 [astro-ph.CO] .

[139] F. Melia, Astron.J. **144**, 110 (2012), arXiv:1206.6289 [astro-ph.CO] .

[140] J.-J. Wei, X.-F. Wu, F. Melia, and R. S. Maier, Astron.J. **149**, 102 (2015), arXiv:1501.02838 [astro-ph.CO] .

[141] M. Moresco, L. Verde, L. Pozzetti, R. Jimenez, and A. Cimatti, JCAP **1207**, 053 (2012), arXiv:1201.6658 [astro-ph.CO] .

[142] M. Moresco, A. Cimatti, R. Jimenez, L. Pozzetti, G. Zamorani, *et al.*, JCAP **1208**, 006 (2012), arXiv:1201.3609 [astro-ph.CO] .

[143] J. Mosher, J. Guy, R. Kessler, P. Astier, J. Marriner, *et al.*, Astrophys.J. **793**, 16 (2014), arXiv:1401.4065 [astro-ph.CO] .

[144] M. Rigault, G. Aldering, M. Kowalski, Y. Copin, P. Antilogus, *et al.*, Astrophys.J., in press (2015), arXiv:1412.6501 [astro-ph.CO] .

[145] M. Betoule *et al.* (SDSS), Astron. Astrophys. **568**, A22 (2014), arXiv:1401.4064 [astro-ph.CO] .

[146] M. Sako *et al.* (SDSS Collaboration), (2014), arXiv:1401.3317 [astro-ph.CO] .

[147] É. Aubourg, S. Bailey, J. E. Bautista, F. Beutler, V. Bhardwaj, *et al.*, (2014), arXiv:1411.1074 [astro-ph.CO] .

[148] A. Font-Ribera, D. Kirkby, N. Busca, J. Miralda-Escude, N. P. Ross, *et al.*, JCAP **1405**, 027 (2014), arXiv:1311.1767 .

[149] W. H. Press, S. A. Teukolsky, W. T. Vetterling, and B. P. Flannery, *Numerical Recipes: The Art of Scientific Computing*, 3rd ed. (Cambridge University Press, New York, 2007).

[150] A. R. Liddle, Mon.Not.Roy.Astron.Soc. **351**, L49 (2004), arXiv:astro-ph/0401198 [astro-ph] .

[151] R. Trotta, Mon.Not.Roy.Astron.Soc. **378**, 72 (2007), arXiv:astro-ph/0504022 [astro-ph] .

[152] P. Mukherjee, D. Parkinson, P. S. Corasaniti, A. R. Liddle, and M. Kunz, Mon.Not.Roy.Astron.Soc. **369**, 1725 (2006), arXiv:astro-ph/0512484 [astro-ph] .

[153] R. Trotta, Contemp.Phys. **49**, 71 (2008), arXiv:0803.4089 [astro-ph] .

[154] L. Verde, S. M. Feeney, D. J. Mortlock, and H. V. Peiris, JCAP **1309**, 013 (2013), arXiv:1307.2904 [astro-ph.CO] .

[155] L. Verde, P. Protopapas, and R. Jimenez, Phys.Dark Univ. **2**, 166 (2013), arXiv:1306.6766 [astro-ph.CO] .

[156] B. Leistedt, H. V. Peiris, and L. Verde, Phys.Rev.Lett. **113**, 041301 (2014), arXiv:1404.5950 [astro-ph.CO] .

[157] H. Akaike, IEEE Transactions on Automatic Control **19**, 716 (1974).

[158] G. Schwarz, Annals of Statistics **6**, 461 (1978).

[159] N. Kaiser, Mon. Not. Roy. Astron. Soc. **231**, 149 (1989).

[160] K. M. Gorski, M. Davis, M. A. Strauss, S. D. M. White, and A. Yahil, Astrophys. J. **344**, 1 (1989).

[161] A. Sandage, G. A. Tammann, and A. Yahil, Astrophys. J. **232**, 352 (1979).

[162] A. Nusser and M. Davis, Astrophys. J. **736**, 93 (2011), arXiv:1101.1650 [astro-ph.CO] .

[163] E. Macaulay, H. A. Feldman, P. G. Ferreira, A. H. Jaffe, S. Agarwal, M. J. Hudson, and R. Watkins, Mon. Not. Roy. Astron. Soc. **425**, 1709 (2012), arXiv:1111.3338 [astro-ph.CO] .

[164] E. Branchini, M. Davis, and A. Nusser, Mon. Not. Roy. Astron. Soc. **424**, 472 (2012), arXiv:1202.5206 [astro-ph.CO] .

[165] M. Feix, A. Nusser, and E. Branchini, JCAP **1409**, 019 (2014), arXiv:1405.6710 [astro-ph.CO] .

[166] M. A. Strauss and J. A. Willick, Phys. Rept. **261**, 271 (1995), arXiv:astro-ph/9502079 [astro-ph] .

[167] L. Hui and P. B. Greene, Phys. Rev. **D73**, 123526 (2006), arXiv:astro-ph/0512159 [astro-ph] .

[168] T. M. Davis *et al.*, Astrophys. J. **741**, 67 (2011), arXiv:1012.2912 [astro-ph.CO] .

[169] C. Bonvin, R. Durrer, and M. A. Gasparini, Phys. Rev. **D73**, 023523 (2006), [Erratum: Phys. Rev. D85, 029901 (2012)], arXiv:astro-ph/0511183 [astro-ph] .

[170] A. Challinor and A. Lewis, Phys. Rev. **D84**, 043516 (2011), arXiv:1105.5292 [astro-ph.CO] .

[171] C. Bonvin and R. Durrer, Phys. Rev. **D84**, 063505 (2011), arXiv:1105.5280 [astro-ph.CO] .

[172] F. Schmidt and D. Jeong, Phys. Rev. **D86**, 083527 (2012), arXiv:1204.3625 [astro-ph.CO] .

[173] D. Jeong, F. Schmidt, and C. M. Hirata, Phys. Rev. **D85**, 023504 (2012), arXiv:1107.5427 [astro-ph.CO] .

[174] N. Kaiser and M. J. Hudson, Mon. Not. Roy. Astron. Soc. **450**, 883 (2015), arXiv:1411.6339 [astro-ph.CO] .

[175] J. D. Neill, M. J. Hudson, and A. J. Conley (SNLS), Astrophys. J. **661**, L123 (2007), arXiv:0704.1654 [astro-ph] .

[176] G. Hinshaw *et al.* (WMAP), Astrophys. J. Suppl. **180**, 225 (2009), arXiv:0803.0732 [astro-ph] .

[177] S. Jha, A. G. Riess, and R. P. Kirshner, Astrophys. J. **659**, 122 (2007), arXiv:astro-ph/0612666 [astro-ph] .

[178] P. A. R. Ade *et al.* (Planck), (2015), arXiv:1502.01589 [astro-ph.CO] .

[179] I. Ben-Dayan, R. Durrer, G. Marozzi, and D. J. Schwarz, Phys. Rev. Lett. **112**, 221301 (2014), arXiv:1401.7973 [astro-ph.CO] .

[180] C. Gordon, K. Land, and A. Slosar, Phys. Rev. Lett. **99**, 081301 (2007), arXiv:0705.1718 [astro-ph] .

[181] A. Cooray, D. Holz, and D. Huterer, Astrophys. J. **637**, L77 (2006), arXiv:astro-ph/0509579 [astro-ph] .

[182] S. Hannestad, T. Haugboelle, and B. Thomsen, JCAP **0802**, 022 (2008), arXiv:0705.0979 [astro-ph] .

[183] A. Abate and O. Lahav, Mon. Not. Roy. Astron. Soc. **389**, 47 (2008), arXiv:0805.3160 [astro-ph] .

[184] S. Bhattacharya, A. Kosowsky, J. A. Newman, and A. R. Zentner, Phys. Rev. **D83**, 043004 (2011), arXiv:1008.2560 [astro-ph.CO] .

[185] T. Castro and M. Quartin, Mon. Not. Roy. Astron. Soc. **443**, L6 (2014), arXiv:1403.0293 .

[186] Y.-Z. Ma, C. Gordon, and H. A. Feldman, Phys. Rev. **D83**, 103002 (2011), arXiv:1010.4276 [astro-ph.CO] .

[187] R. Watkins, H. A. Feldman, and M. J. Hudson, Mon. Not. Roy. Astron. Soc. **392**, 743 (2009), arXiv:0809.4041 [astro-ph] .

[188] J. Colin, R. Mohayaee, S. Sarkar, and A. Shafieloo, Mon. Not. Roy. Astron. Soc. **414**, 264 (2011), arXiv:1011.6292 [astro-ph.CO] .

[189] D.-C. Dai, W. H. Kinney, and D. Stojkovic, JCAP **1104**, 015 (2011), arXiv:1102.0800 [astro-ph.CO] .

[190] S. J. Turnbull, M. J. Hudson, H. A. Feldman, M. Hicken, R. P. Kirshner, and R. Watkins, Mon. Not. Roy. Astron. Soc. **420**, 447 (2012), arXiv:1111.0631 [astro-ph.CO] .

[191] U. Feindt *et al.*, Astron. Astrophys. **560**, A90 (2013), arXiv:1310.4184 [astro-ph.CO] .

[192] G. J. Mathews, B. Rose, P. Garnavich, D. Yamazaki, and T. Kajino, (2014), arXiv:1412.1529 [astro-ph.CO] .

[193] T. Haugboelle, S. Hannestad, B. Thomsen, J. Fynbo, J. Sollerman, and S. Jha, Astrophys. J. **661**, 650 (2007), arXiv:astro-ph/0612137 [astro-ph] .

[194] A. Weyant, M. Wood-Vasey, L. Wasserman, and P. Freeman, Astrophys. J. **732**, 65 (2011), arXiv:1103.1603 [astro-ph.CO] .

[195] Y.-Z. Ma and D. Scott, Mon. Not. Roy. Astron. Soc. **428**, 2017 (2013), arXiv:1208.2028 [astro-ph.CO] .

[196] A. Johnson *et al.*, Mon. Not. Roy. Astron. Soc. **444**, 3926 (2014), arXiv:1404.3799 [astro-ph.CO] .

[197] Y.-Z. Ma and J. Pan, Mon. Not. Roy. Astron. Soc. **437**, 1996 (2014), arXiv:1311.6888 [astro-ph.CO] .

[198] D. J. Schwarz and B. Weinhorst, Astron. Astrophys. **474**, 717 (2007), arXiv:0706.0165 [astro-ph] .

[199] B. Kalus, D. J. Schwarz, M. Seikel, and A. Wiegand, Astron. Astrophys. **553**, A56 (2013), arXiv:1212.3691 [astro-ph.CO] .

[200] X. Yang, F. Y. Wang, and Z. Chu, Mon. Not. Roy. Astron. Soc. **437**, 1840 (2014), arXiv:1310.5211 [astro-ph.CO] .

[201] S. Appleby, A. Shafieloo, and A. Johnson, Astrophys. J. **801**, 76 (2015), arXiv:1410.5562 [astro-ph.CO] .

[202] H.-N. Lin, S. Wang, Z. Chang, and X. Li, (2015), arXiv:1504.03428 [astro-ph.CO] .

[203] B. Javanmardi, C. Porciani, P. Kroupa, and J. Pflamm-Altenburg, Astrophys. J. **810**, 47 (2015), arXiv:1507.07560 [astro-ph.CO] .

[204] G. E. Addison, Y. Huang, D. J. Watts, C. L. Bennett, M. Halpern, G. Hinshaw, and J. L. Weiland, Astrophys. J. **818**, 132 (2016), arXiv:1511.00055 [astro-ph.CO] .

[205] T. D. Kitching, L. Verde, A. F. Heavens, and R. Jimenez, (2016), arXiv:1602.02960 [astro-ph.CO] .

[206] S. Anselmi, G. D. Starkman, and R. K. Sheth, Mon. Not. Roy. Astron. Soc. **455**, 2474 (2016), arXiv:1508.01170 [astro-ph.CO] .

[207] M. C. March, R. Trotta, P. Berkes, G. D. Starkman, and P. M. Vaudrevange, Mon. Not. Roy. Astron. Soc. **418**, 2308 (2011), [Mon. Not. Roy. Astron. Soc.418,4(2011)], arXiv:1102.3237 [astro-ph.CO] .

[208] D. Rubin *et al.* (Supernova Cosmology Project), Astrophys. J. **813**, 137 (2015), arXiv:1507.01602 [astro-ph.CO] .